

**GRAIN REFINEMENT AND TEXTURE DEVELOPMENT OF
CAST $\text{Bi}_{90}\text{Sb}_{10}$ ALLOY VIA SEVERE PLASTIC DEFORMATION**

A Dissertation

by

JAE-TAEK IM

Submitted to the Office of Graduate Studies of
Texas A&M University
in partial fulfillment of the requirements for the degree of

DOCTOR OF PHILOSOPHY

May 2007

Major Subject: Mechanical Engineering

**GRAIN REFINEMENT AND TEXTURE DEVELOPMENT OF
CAST BI₉₀SB₁₀ ALLOY VIA SEVERE PLASTIC DEFORMATION**

A Dissertation

by

JAE-TAEK IM

Submitted to the Office of Graduate Studies of
Texas A&M University
in partial fulfillment of the requirements for the degree of

DOCTOR OF PHILOSOPHY

Approved by:

Chair of Committee,	K. Ted Hartwig
Committee Members,	Richard Griffin
	Ibrahim Karaman
	Donald G. Naugle
Head of Department,	Dennis L. O'Neal

May 2007

Major Subject: Mechanical Engineering

ABSTRACT

Grain Refinement and Texture Development of Cast Bi₉₀Sb₁₀ Alloy

via Severe Plastic Deformation. (May 2007)

Jae-taek Im, B.S., Yeung-nam University, Republic of Korea;

M.S., Texas A&M University

Chair of Advisory Committee: Dr. K. Ted Hartwig

The purpose of this work was to study learn about grain refinement mechanisms and texture development in cast n-type Bi₉₀Sb₁₀ alloy caused by severe plastic deformation. The practical objective is to produce a fine grained and textured microstructure in Bi₉₀Sb₁₀ alloy with enhanced thermoelectric performance and mechanical strength.

In the study, twelve millimeter diameter cast bars of Bi₉₀Sb₁₀ alloy were encapsulated in square cross section aluminum 6061 alloy containers. The composite bars were equal channel angular (ECAE) extruded through a 90 degree angle die at high homologous temperature. Various extrusion conditions were studied including punch speed (0.1, 0.3 and 0.6 in/min), extrusion temperature (220, 235 and 250°C), number of extrusion passes (1, 2 and 4), route (A, B_C and C), and exit channel area reduction ratio (half and quarter area of inlet channel). The affect of an intermediate long term heat treatment (for 100 hours at 250°C under 10⁻³ torr vacuum) was explored. Processed materials were characterized by optical microscopy, x-ray diffraction, energy dispersive spectroscopy, wavelength dispersive spectroscopy and scanning electron microscopy.

Texture was analyzed using the {006} reflection plane to identify the orientation of the basal poles in processed materials.

The cast grains were irregularly shaped, had a grain size of hundreds-of-microns to millimeters, and showed inhomogeneous chemical composition. Severe plastic deformation refines the cast grains through dynamic recrystallization and causes the development of a bimodal microstructure consisting of fine grains (5-30 micron) and coarse grains (50-300 micron). ECAE processing of homogenized Bi-Sb alloy causes grain refinement and produces a more uniform microstructure. Texture results show that ECAE route C processing gives a similar or slightly stronger texture than ECAE route A processing. In both cases, the basal-plane poles become aligned with the shear direction. Reduction area exit channel extrusion is more effective for both grain refinement and texture enhancement than simple ECAE processing.

DEDICATION

To my father and my family

ACKNOWLEDGMENTS

I would like to express my deepest gratitude and respect to my advisor, Dr. K. Ted Hartwig, for his consistent care, enthusiasm, and untiring patience throughout the course of my Ph.D study. This dissertation would not have been possible without him. My appreciation goes to Dr. Richard B. Griffin, Dr. Ibrahim Karaman and Dr. Donald G. Naugle for their guidance, discussion and support while serving on my advisory committee.

Special thanks goes to Robert Barber who designed the tools, processed samples and discussed this work with me. Robert has given a tremendous amount of help throughout this research. I would like to acknowledge Marlow Industries, who supplied materials and funding for this study. Special thanks to Dr. Jeff Sharp who gave encouragement and shared his ideas throughout this work. Thanks are extended to my office mates, Dr. Suveen Mathaudhu and David Foley, who shared their time and ideas with me.

I also thank Dr. Parag Ravindran who willingly reviewed my dissertation, and Dr. Seungik Baek, Dr. Chaewhan Lim, Dr. Teawon Han, and other Korean colleagues in the Mechanical Engineering Department who shared their time and ideas with me.

Finally, the most notable thanks go to my family, especially to my father and mother, for their unfailing love and encouragement during this Ph.D journey.

TABLE OF CONTENTS

	Page
ABSTRACT	iii
DEDICATION	v
ACKNOWLEDGMENTS	vi
TABLE OF CONTENTS	vii
LIST OF FIGURES	ix
LIST OF TABLES	xiv
CHAPTER	
I INTRODUCTION	1
II LITERATURE REVIEW.....	5
2.1. Thermoelectricity and thermoelectric properties of materials	5
2.1.1. Introduction to the thermoelectric phenomenon	5
2.1.2. Thermoelectric materials.....	9
2.1.3. Applications of thermoelectric materials to thermoelectric modules	10
2.2. Bismuth antimony alloys for cooling applications at low temperature.....	12
2.2.1. Bismuth antimony alloys as thermoelectric materials	12
2.2.2. Crystal structure and phase diagram of Bi-Sb alloys	13
2.2.3. Anisotropic properties of Bi-Sb alloy	16
2.2.4. Mechanical properties of Bi-Sb alloy	18
2.2.5. Manufacturing of polycrystalline thermoelectric materials	18
2.3. Plastic deformation of hexagonal closed packed (hcp) metals	20
2.3.1. Deformation mechanisms of hcp metals and alloys	20
2.3.2. Dymnamic recrystallization in materials undergoing large deformation	22
2.4. ECAE processing to achieve severe plastic deformation	25
2.4.1. Introduction to ECAE processing	25
2.4.2. ECAE processing of hcp materials	29
2.4.3. Materials processing of Bi ₂ Te ₃ alloys	30
2.4.4. ECAE processing of thermoelectric materials	33
III EXPERIMENT PROCEDURES	37
3.1. ECAE processing procedures	37

TABLE OF CONTENTS (CONTINUED)

CHAPTER	Page
3.2. Extrusion conditions and test matrix	38
3.3. Sample preparation for analyses and equipments	40
IV EXPERIMENTAL RESULTS.....	43
4.1. As received materials.....	43
4.2. Preliminary ECAE processing	50
4.3. Microstructure development of preprocessed Bi-Sb alloys.....	52
4.3.1. Microstructure of preprocessed Bi-Sb alloys	52
4.3.2. Texture of preprocessed Bi-Sb alloys	58
4.4. Microstructure from further deformation of preprocessed Bi-Sb alloys	58
4.4.1. Grain refinement with further deformation	58
4.4.2. Microprobe analysis for chemical homogeneity	69
4.4.3. Texture development with further deformation	74
4.5. Microstructure development with further deformation of a preprocessed and heat treated Bi-Sb alloy	78
4.5.1. Grain refinement with a heat treated Bi-Sb alloy	78
4.5.2. Microprobe analysis for chemical homogeneity	79
V DISCUSSION	84
5.1. Grain refinement of cast Bi-Sb alloys	85
5.1.1. Chemical homogeneity effects on grain refinement	85
5.1.2. Dynamic recrystallization mechanisms for grain refinement	90
5.2. Texture development of Bi-Sb alloys	92
VI FINDINGS AND CONCLUSIONS	100
VII SUGGESTIONS FOR FURTHER STUDY	105
REFERENCES	106
VITA	113

LIST OF FIGURES

FIGURE	Page
1. Thermoelectric circuit between two different materials (A and B). When there is a temperature gradient between a hot (T_H) and cold junction (T_L) [21], an electromotive force is generated between point 1 and 2.	5
2. Temperature dependence of the dimensionless figure of merit (zT) for different semiconducting alloys ([14], [21], [25], [26], [27], and [28]).....	9
3. Schematic of refrigerating thermocouple module which illustrates that the electric current induces heat transfer flow through the thermoelements [29].	11
4. Crystal structure of rhombohedral bismuth and antimony [34]. The circles representing atoms can be either Bi or Sb structures of complete solubility between these two elements.....	14
5. Binary phase diagram of the bismuth antimony alloy system [41].....	15
6. The anisotropic figure of merit for single crystal material measured along the a and c directions (i) the temperature range 20 to 300 °K for $Bi_{88}Sb_{12}$ [31] and (ii) for the entire Bi-Sb alloy composition [14]	17
7. Schematic pole figures of [002] and [100] rolling texture in hcp metals depending on the c/a ratios of (i) $c/a > 1.633$, (ii) $c/a \approx 1.633$, and (iii) $c/a < 1.633$ [59].....	23
8. Schematic view of the equal channel angular extrusion (ECAE) process.....	25
9. Schematic illustration of extrusion routes: (i) first pass (ii) second pass, (1) route A is without rotation, (2) route B is with 90° rotation with respect to the extrusion axis prior to the second pass, and (3) route C is with 180° rotation with respect to the extrusion axis between passes.....	27
10. Schematic views of shear planes and shear directions for routes: (i) route A, (ii) route B _C , and (iii) route C. (The longitudinal (L) plane, transverse (T), and flow (F) planes are defined in illustration (iii).....	28
11. Schematic of shear deformation via the ECAE process (i) the element experiences idealized simple shear at the shear zone and (ii) the element experiences rigid body rotation (90°) and simple shear [96]	31
12. Pressure direction and alignment of grains in Bi_2Te_3 in the c direction.	32

LIST OF FIGURES (CONTINUED)

FIGURE	Page
13. Schematic views of crystal orientation rearrangement during area reduction angular extrusion: (i) shear extrusion process and (ii) crystal rearrangement before (a_1) and after (a_2) extrusion [13]	35
14. Schematic views of billets extruded through an exit channel with different areas: (i) same, (ii) half, and (iii) quarter the area of the inlet channel.....	40
15. Microstructures of cast Bi-Sb alloy (i) longitudinal section and (ii) transverse section	44
16. Microprobe analysis with EDS for cast Bi-Sb alloy: (i) EBS image and (ii) qualitative results of bright area (1) and dark area (2).....	45
17. Microprobe analysis with EDS for cast Bi-Sb alloy: (i) EBS image and (ii) qualitative results of bright area (10), gray area (11), and dark area (12)	46
18. The $\{006\}$ pole figures of cast Bi-Sb alloy for (i) transverse, and (ii) longitudinal sections	48
19. Thermal property of cast $\text{Bi}_{90}\text{Sb}_{10}$ alloy with differential scanning calorimeter (DSC).....	49
20. Fracture surface of cast Bi-Sb alloy with scanning electron microscope (SEM).....	50
21. Microstructure development of Bi-Sb alloy after one pass via ECAE at 250°C and 0.1 in/min. Region A is coarse grain and B is fine grain area.....	51
22. Microstructure development of Bi-Sb alloy after (i) two extrusion passes and (ii) four extrusion passes via route A at an extrusion temperature of 250°C and an extrusion rate of 0.1 in/min	53
23. Microstructure development of Bi-Sb alloy after four extrusion passes via route B_C with different punch speeds: (i) 0.1, (ii) 0.3, and (iii) 0.6 in/min at extrusion temperature 250°C	55
24. Microstructure of $\text{Bi}_{90}\text{Sb}_{10}$ alloy after four extrusion passes with a punch speed of 0.3 in/min via route B_C of different extrusion temperatures: (i) 220°C and (ii) 235°C	56
25. Microstructure development of Bi-Sb alloy encapsulated in a Cu can after four extrusion passes via route B_C at an extrusion temperature of 235°C and at a punch speed of 0.3 in/min	57

LIST OF FIGURES (CONTINUED)

FIGURE	Page
26. The {0 0 6} pole figures of preprocessed material under extrusion rates: (i) 0.1, (ii) 0.3 (iii) 0.6 in/min via route B _C at 250°C (ED: Extrusion direction, LD: Longitudinal plane normal direction, FD: Flow plane normal direction)	59
27. The {0 0 6} pole figures of preprocessed material under extrusion temperatures: (i) 235°C (ii) 220°C via route B _C at 0.3in/min. (ED: Extrusion direction, LD: Longitudinal plane normal direction, FD: Flow plane normal direction)	60
28. Microstructure development of preprocessed Bi ₉₀ Sb ₁₀ alloy after one extrusion pass at an extrusion temperature of 235°C and a punch speed of 0.3 in/min. (Preprocessed conditions: extrusion temperature 235°C; punch speed 0.3 in/min; ECAE route B _C).....	61
29. Microstructure development of preprocessed Bi ₉₀ Sb ₁₀ alloy after two extrusion passes via route A at an extrusion temperature of 235°C and a punch speed of 0.3 in/min.	62
30. Microstructure development of preprocessed Bi ₉₀ Sb ₁₀ alloy after four extrusion passes via route A at an extrusion temperature of 235°C and a punch speed of 0.3 in/min.	63
31. Microstructure development of preprocessed Bi ₉₀ Sb ₁₀ alloy after two extrusion passes via route C at an extrusion temperature of 235°C and a punch speed of 0.3 in/min.	64
32. Microstructure development of preprocessed Bi ₉₀ Sb ₁₀ alloy after four extrusion passes via route C at an extrusion temperature of 235°C and a punch speed of 0.3 in/min.	65
33. Microstructure development of preprocessed Bi ₉₀ Sb ₁₀ alloy after using half exit area extrusion at an extrusion temperature of 235°C and a punch speed of 0.15 in/min.....	66
34. Microstructure development of preprocessed Bi ₉₀ Sb ₁₀ alloy after using quarter exit area extrusion at an extrusion temperature of 235°C and a punch speed of 0.15 in/min	67
35. Microprobe analysis with EDS for one extrusion pass of preprocessed Bi ₉₀ Sb ₁₀ alloy via ECAE: (i) coarse grain area, (ii) fine grain area, and (iii) qualitative analysis	70

LIST OF FIGURES (CONTINUED)

FIGURE	Page
36. Microprobe analysis with WDS for one extrusion pass of preprocessed Bi ₉₀ Sb ₁₀ alloy via ECAE: (i) examined locations in coarse grain area, (ii) in fine grain area, and (iii) quantitative analysis results	71
37. Microprobe analysis with EDS for one extrusion pass of preprocessed Bi ₉₀ Sb ₁₀ alloy via half exit area extrusion: (i) coarse grain area, (ii) fine grain area, and (iii) qualitative analysis	72
38. Microprobe analysis with WDS for one extrusion pass of preprocessed Bi ₉₀ Sb ₁₀ alloy via half exit area extrusion: (i) examined locations in EBS image and (ii) quantitative analysis results	73
39. The {0 0 6} pole figures of processed material after: (i) one pass, (ii) two passes and (iii) four passes via route A (ED: Extrusion direction, LD: Longitudinal plane normal direction, FD: Flow plane normal direction).....	75
40. The {0 0 6} pole figures of processed material after: (i) two passes and (ii) four passes via route C (ED: Extrusion direction, (LD: Longitudinal plane normal direction, FD: Flow plane normal direction)	76
41. The {0 0 6} pole figures of processed material following: (i) half and (ii) quarter area exit channel extrusion (ED: Extrusion direction, LD: Longitudinal plane normal direction, FD: Flow plane normal direction).....	77
42. Microstructure of preprocessed and heat treated Bi-Sb alloy. Heat treatment conditions: annealing temperature of 250°C for 100 hours under low vacuum (10 ⁻³ torr)	78
43. Microstructure after four extrusion passes via route B _C using preprocessed and heat treated Bi ₉₀ Sb ₁₀ alloy	80
44. Microprobe analysis with EDS of coarse grains after four extrusion passes of preprocessed and heat treated Bi ₉₀ Sb ₁₀ alloy: (i) bright coarse grains and (ii) dark coarse grains	81
45. Microprobe analysis with EDS of fine grains after four extrusion passes of preprocessed and heat treated Bi ₉₀ Sb ₁₀ alloy: bright fine grain (7) and dark fine grain (8).....	82
46. Illustrations of lattice strains induced by substituted atoms in Bi-Sb alloy: (i) tensile lattice strains imposed on the host atoms (Bi) due to a smaller substitutional atom (Sb), and (ii) dislocation lattice strains induced by a group of smaller substitutional atoms	89

LIST OF FIGURES (CONTINUED)

FIGURE	Page
47. Illustrations of dynamic recrystallization mechanisms in Bi-Sb alloy during hot deformation: (i) sub-grains are formed by applied strain and produce new high angle grain boundaries by rotations and (ii) dislocations induced by strain are accumulated in the vicinity of old grain boundaries. Tyny grains form in the accumulated dislocation area and develop new high angle grain boundaries	91
48. Illustrations for element transformation and angles between transformed element and extrusion axis depending on the number of extrusion pass (N) for route A	95
49. Schematic illustration for different orientations of a material element (representing the basal plane hexagon) after the first (i) and second pass (ii) route A and (iii) route C	97
50. Illustrations for element transformation and angles between transformed element and extrusion axis depending on the exit channel area: (i) equal to inlet area (ii) half inlet area, and (iii) quarter inlet area	99

LIST OF TABLES

TABLE	Page
1. Thermoelectric properties for various materials at room temperature [21, 24].....	7
2. Crystal structure parameters of Bi and Sb at 4.2 °K [34, 39].....	15
3. Test matrix for determining the best preprocessing condition for Bi ₉₀ Sb ₁₀ cast ingots. The chosen processing route is 4B _C	39
4. Test matrix for studying texture development with preprocessed Bi ₉₀ Sb ₁₀ alloy billets (Preprocessed conditions: 4B _C at 235°C and 0.3 in/min)	39
5. Chemical compositions of cast Bi-Sb alloy with microprobe analysis using WDS.....	48
6. Chemical composition of four extrusion pass Bi-Sb after preprocessing and heat treatment analyzed by WDS. Examined locations displayed in Figure 44 and 45	83
7. Refined grain size and percent of fine grain area for preprocessed Bi ₉₀ Sb ₁₀ alloys (four extrusion pass of ECAE via route B _C)	87
8. Summarized refined grain size and percent of fine grain area with further deformation of preprocessed Bi ₉₀ Sb ₁₀ alloy billets (preprocessed conditions: 4B _C at 235°C and 0.3 in/min)	87
9. Summary of Sb content in cast, fine, and coarse grains of nominal Bi ₉₀ Sb ₁₀ alloy billets processed following various deformation routes ...	88
10. Summary of maximum intensity values (logarithmic scale) of basal poles and their positions (degrees) for preprocessed Bi-Sb alloys.....	93
11. Test matrix for determining the best preprocessing condition for Bi ₉₀ Sb ₁₀ cast ingots. Summary of maximum values (logarithmic scale) basal poles and their positions (degrees) for preprocessed Bi-Sb alloys.	94

CHAPTER I

INTRODUCTION

A large amount of plastic deformation is an efficient method to produce microstructure alteration and physical properties improvement in materials [1]. For instance, the application of severe plastic deformation to conventional polycrystalline metals provides a powerful tool for refining grain size. Although several methods to impose severe plastic deformation (SPD) in metals are available, the two most commonly used methods are high-pressure torsion (HPT) and equal channel angular extrusion (ECAE) [2]. The ECAE process has several advantages: (1) intensive shear strain put into a bulk work piece; (2) the possibility of producing a variety of microstructures using various ECAE processing alternatives; (3) repeating extrusion without changing the work piece cross-section area and dimensions. These advantages have enabled ECAE process application to many ductile metals and alloys successfully [3-6].

The ECAE process was recently applied to low ductility or difficult to work materials including materials of hexagonal crystal structure [7-9], and intermetallic compounds and alloys [10-13]. These materials often show shear localization and fracture during or after the ECAE process, even at elevated temperatures [10, 11]. But

under carefully controlled conditions of temperature, extrusion rate, and applying back pressure it is possible to perform the ECAE process on these materials. It is known that Bi-Sb alloys, which fall in the category of difficult to work materials and show brittle behavior, experience slip, rotations, twins, recovery and recrystallization of grains during plastic deformation occurs at elevated temperature. The above mentioned deformation mechanisms enhance the ductility of the material and produce an improved microstructure (refined grain structure and sometimes texture). Appropriate processing conditions (especially strain rate and processing temperature) are necessary to achieve large deformation in low ductility or difficult to work materials.

Bismuth antimony alloys are known as low temperature thermoelectric materials. Their thermoelectric performance is good between 70 – 150°K and they are used for refrigeration at low temperature [14, 15]. Although Bi-Sb single crystals show superior thermoelectric performance compared to that of polycrystalline materials, the application of single crystal materials in thermoelectric devices is restricted because of their poor mechanical properties. The brittle behavior of Bi-Sb single crystals is caused by easy failure along a cleavage plane (basal plane) [16]. Powder metallurgy methods have been used to improve the mechanical properties of polycrystalline Bi-Sb alloys [17, 18]. Polycrystalline alloys made using powder metallurgy techniques offer several advantages to manufacturing single crystals: easy alloy synthesis, easy handling, consistency of composition, short preparation time, small grain size, and untextured products.

Polycrystalline Bi-Sb alloys produced by powder metallurgy result in fine grained microstructure which reduces catastrophic brittle failure, but they show poor thermoelectric performance as a result of random orientations of grains. A preferred grain orientation in bulk polycrystalline Bi-Sb materials is favorable to improved thermoelectric performance [19, 20]. A highly textured microstructure can yield strong anisotropic behavior that approaches single crystal like thermoelectric performance.

Currently the most viable method to improve mechanical and thermoelectrical properties of polycrystalline Bi-Sb alloy is powder consolidation by pressing or conventional area reduction extrusion at elevated temperature. The Bi-Sb alloy powders are obtained by various techniques: mechanical alloying, arc-plasma spraying, and grinding of zone-melted ingot. It is known that consolidation of the fine powders through pressing or extrusion at elevated temperature produces a fine grained microstructure and texture. Consolidated Bi-Sb alloys give opportunities to improve mechanical properties and thermoelectric performance.

However, powder preparation requires elaborate time and effort because of contamination issues, oxidation problems and complex processing. From the standpoint of grain refinement, cast ingot extrusions have advantages over billets obtained by powder consolidation. An alternative to regular extrusion is the ECAE process. The ECAE process has several advantages as noted earlier.

The purpose of this work is to determine whether ECAE and area reduction angular extrusion at elevated temperature can be applied to produce a material with fine homogeneous grain sized microstructure and strong texture from cast Bi-Sb alloys. If the

purpose is achieved, the objective is to explain how the microstructure and texture develop in cast Bi-Sb alloy. The practical objective is to produce a fine grained and textured microstructure in $\text{Bi}_{90}\text{Sb}_{10}$ alloy in order to improve mechanical strength and enhanced thermoelectric performance. Severe plastic deformation will be introduced by multipass equal channel angular extrusion and reduced exit channel area angular extrusion at elevated temperature. ECAE processing of cast $\text{Bi}_{2-x}\text{Sb}_x\text{Te}_3$ alloy ingots, which have similar mechanical behavior, was successfully conducted by the author [12].

A well planned/executed project enables (1) a better understanding of how the cast grains refine during hot plastic deformation, (2) the effect of heat treatment following SPD processing steps on the microstructure, and (3) correlation of microstructure and texture with strain levels and processing routes. The primary task is to study the grain refinement mechanisms of cast Bi-Sb alloys and understand how this is related to level of strain, processing path, and microstructural homogeneity. The next task is to investigate how much chemical homogeneity changes with heat treatment between ECAE processing, and how heat treatment effects grain refinement. The final task is to find and understand the mechanism of texture development in Bi-Sb alloys through multipass ECAE and reduced area exit channel extrusion.

CHAPTER II

LITERATURE REVIEW

2.1. Thermoelectricity and thermoelectric properties of materials

2.1.1. Introduction to the thermoelectric phenomenon

Thermoelectric effects are associated with the flow of heat and electricity in materials. A thermoelectric circuit is composed of two electrically conducting materials (A+B) joined as shown in Figure 1. T_L and T_H represent cold and hot junction points respectively. An electromotive force is generated between points 1 and 2 (See Figure 1) in the open circuit. This is called the Seebeck effect [21]. The thermoelectric current arises from a slight inequality between the currents carried by ‘hot’ electrons and ‘cool’ electrons. The imbalanced charge carriers generated by the temperature difference

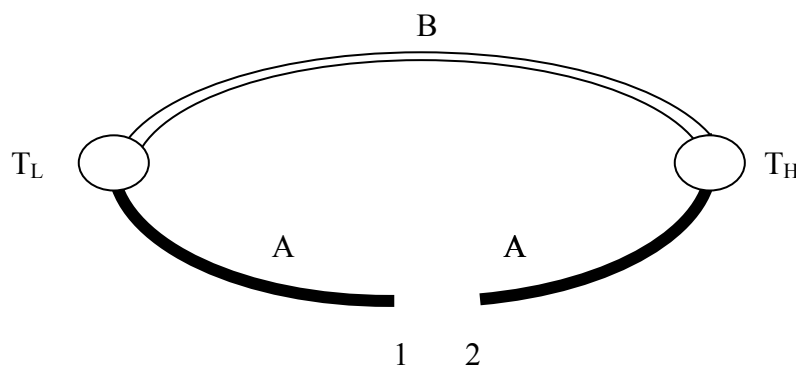


Figure 1. Thermoelectric circuit between two different materials (A and B). When there is a temperature gradient between a hot (T_H) and cold junction (T_L) [21], an electromotive force is generated between point 1 and 2.

induce the thermoelectric effect. The hot electrons flow into the cold junction and cold ones flow into the hot junction [22]. The flow rates of electrons are not equal because the two materials (A+B) have different electrical and thermal properties. Thus, there will be a net electric current and an electric motive force between point 1 and 2 in figure 1. The electromotive force (\mathcal{E}) is proportional to the temperature difference (ΔT) between points T_L and T_H , which is defined by the following equation (1):

$$\mathcal{E} = \alpha \Delta T \quad (1)$$

The Seebeck coefficient (α) is a property of the material.

When a circuit consisting of two dissimilar conductors carries electric current, heat is given off at one junction and is absorbed at the other. The rate at which heat is absorbed is proportional to the current. This phenomenon is called the Peltier cooling effect. The Seebeck and Peltier effects underlie the conversion of heat energy into electrical energy and vice versa.

The electrical resistivity is an important factor for thermoelectricity. The electrical resistivity (ρ) of a material is determined by the charge carrier concentration (n), carrier charge (e), and charge carrier mobility (μ) and is defined by equation (2):

$$\rho = \frac{1}{ne \mu} \quad (2)$$

Last important factor for thermoelectricity is thermal conductivity (k) of materials. Two mechanisms are responsible for conduction of heat in materials: electrons and lattice vibrations. Around room temperature, the conduction of heat in metals is mainly

by free electrons because the electronic contribution to heat transfer is very large compared to the lattice vibration contribution [22, 23]. Thus, near room temperature, electrical conductivity is proportional to thermal conductivity in metals. However, the conduction of heat in dielectric materials is mainly by lattice vibrations or phonons because dielectric materials do not have free electrons.

The figure of merit used for describing the performance of thermoelectric materials is defined by the following equation (3):

$$z = \frac{\alpha^2}{\rho k} \quad (3)$$

The ideal high performance thermoelectric material has a high Seebeck coefficient, a low electrical resistivity and a low thermal conductivity. These properties depend on temperature. Thus, the dimensionless value of zT is widely used for determining the thermoelectric performance of materials. It is desirable to obtain materials which have a high value of z over as wide a temperature range as possible.

Table 1. Thermoelectric properties for various materials at room temperature [21, 24].

Materials\Properties	$Z (^{\circ}\text{K})$	$\alpha (\mu\text{V}/^{\circ}\text{K})$	$\rho (\Omega\text{m})$	$k (\text{W}/\text{mK})$
Metal	$\times 10^{-6}$	1-10	$\sim \times 10^{-8}$	High
Semiconductor	$\times 10^{-3}$	100~500	10^{-4} - 10^6	Medium
Insulator	$\times 10^{-17}$	1000	$< 10^{10}$	Low

Thermoelectric (TE) properties for various materials at room temperature are shown in the Table 1. In metals, electrical resistivity is low and thermal conductivity is high. The electrical conductivity of metals is proportional to thermal conductivity because the primary mechanism that transfers heat in them is by electrons. According to band theory, the Fermi energy level overlaps with the conduction band. Thus, the transfer of heat and electricity in metals is performed mostly by the most energetic or hot free electrons [22]. The thermoelectric effect is caused by these carriers, when hot electrons flow one way and cold ones flow the other way. The Seebeck coefficients of metals are small being on the order of several $\mu\text{V}/\text{K}$ at room temperature [22]. Because these materials have a low figure of merit, they are not suitable for the thermoelectric cooling or power generation applications. Even though the Seebeck coefficient of insulators is high, the electrical resistivity is also high and therefore the overall figure of merit is low, so these materials are also not suitable for TE application.

However, it has been found that the Seebeck coefficients of semiconductors are far higher than those of metals. Although electrical resistivity and thermal resistivity of semiconductors are higher than those of metals, semiconductors are the best candidates for thermoelectric materials because their Seebeck coefficients are at least two orders of magnitude higher [22] and there are two heat carriers in semiconductors: electrons and holes. The Seebeck coefficient of n-type semiconductors is negative, which means that the carriers are electrons, and that of p-type semiconductors is positive meaning, the carriers are holes. When these two types of semiconductors are connected in parallel in a thermoelectric circuit, the thermoelectric performance is maximized.

2.1.2. Thermoelectric materials

The most widely used thermoelectric semiconductors are based on bismuth antimony [14], cesium bismuth telluride [25], bismuth telluride [21], lead telluride [26], and silicon germanium [27, 28] alloys. The applications of thermoelectric materials are determined by their zT values because the figures of merits of materials vary depending on temperature as shown in Figure 2. The reason that material performance depends on temperature is that different semiconductors have different values of their energy band

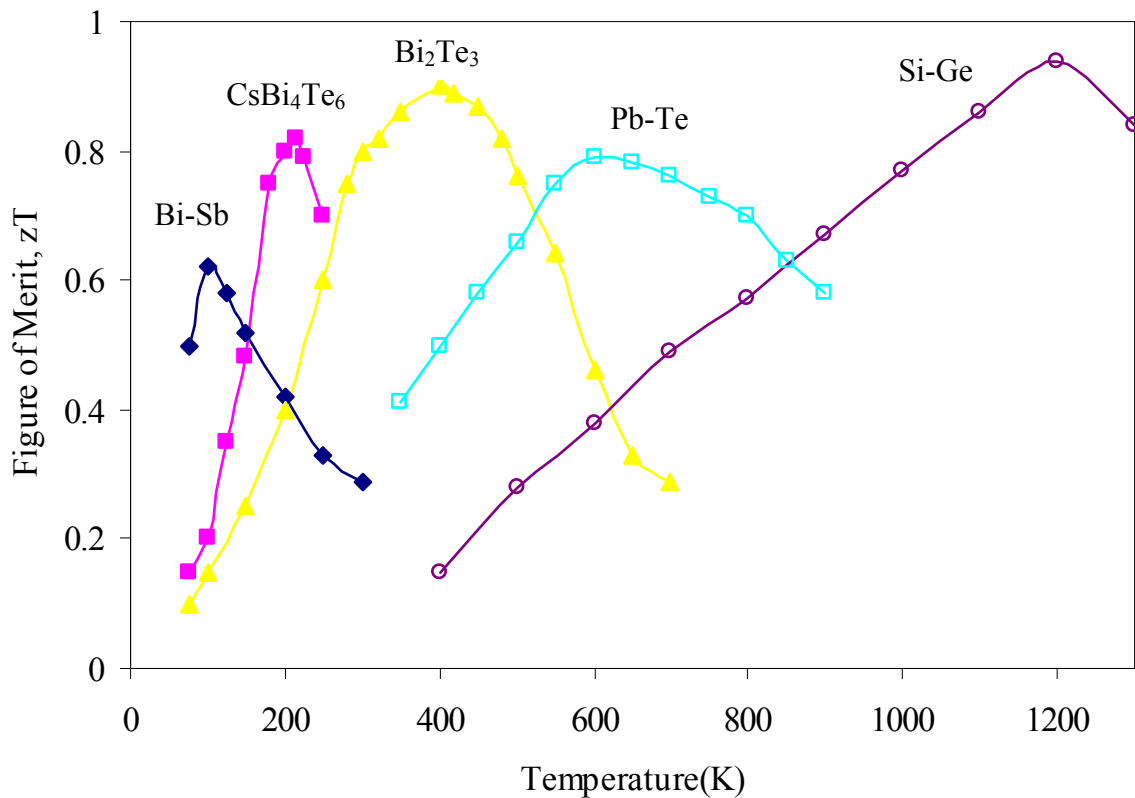


Figure 2. Temperature dependence of the dimensionless figure of merit (zT) for different semiconducting alloys ([14], [21], [25], [26], [27], and [28]).

gaps. Generally speaking, the materials which have their maximum z at higher temperatures have larger energy band gaps and are used in power generation. The materials which have maximum z at lower temperatures have smaller band gaps and are used for refrigeration.

The intermetallics of Bi_2Te_3 with Sb_2Te_3 and Bi_2Se_3 are used for thermoelectric refrigeration at ambient temperature. The band gap of bismuth telluride is about 0.13 eV at room temperature [21]. These alloys, when optimized, have a zT value of about unity at 300K. Bismuth rich antimony alloys are used for low temperature (77~200K) cooling applications. These alloys show the semi-metallic character of bismuth up to about 7 at.% (atomic percent) of antimony. The alloys become n-type semiconductors from 7 to 22 Sb at.% and have a small energy gap up to 30 meV depending on the Sb content in the solid solution [14].

The energy gaps of thermoelectric materials used for power generation are large. The energy gap of lead telluride alloy is for instance 0.32 eV and it is used for power generation at intermediate temperatures (~ 700 K). The energy gaps of silicon and germanium are 1.15eV and 0.65eV respectively. These large energy gap semiconductors are used for higher temperature (1100K~1200K) power generation.

2.1.3. Applications of thermoelectric materials to thermoelectric modules

Semiconductors for cooling were developed in the 1950's. The breakthrough for practical cooling applications was a result of better understanding of the physical properties of solids. Thermoelectric materials are used in cooling devices and stacked to form a thermoelectric module. The coolers operate with direct current (DC) and may be

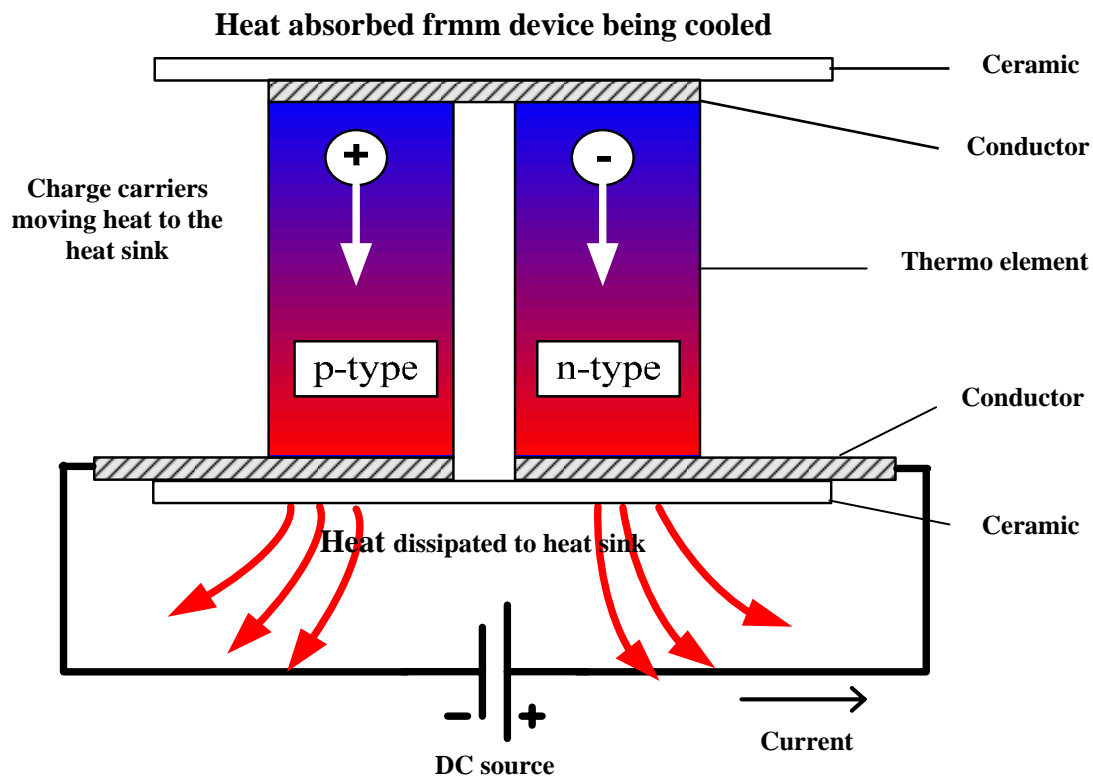


Figure 3. Schematic of refrigerating thermocouple module which illustrates that the electric current induces heat transfer flow through the thermoelements [29].

used for heating or cooling by reversing the direction of current flow. This is achieved by moving heat from one side of the module to the other with current flow. A typical single stage cooler, shown in Figure 3, consists of two ceramic plates with p- and n-type semiconductor materials (bismuth telluride) between the plates. The elements of semiconductor material are connected electrically in series and thermally in parallel [29]. When a positive DC voltage is applied to the n-type thermoelement, electrons pass from the p- to the n-type thermoelement and holes pass from the n- to the p-type the

thermoelement. The charge carriers move the heat generated from a hot device (microchip or laser diode) to the heat sink and the hot side temperature will decrease as heat is absorbed. The heat absorption (cooling) is proportional to the current and the number of thermoelectric couples [21]. This heat is transferred to the hot side of the cooler, where it is dissipated into the heat sink and surrounding environment. For practical applications, a thermoelectric cooling device consists of the assembly of thermoelectric couples between two ceramics as shown in Figure 3. The ceramic plate materials should be good dielectric insulators, have mechanical strength, have compatible thermal expansion with the (copper) conductor and have good thermal conductivity [30]. The assembled multi couple module is connected in parallel to obtain adequate cooling power. However, the thermoelectric couples are connected in series in order to obtain greater temperature difference by operating cooling units in cascade. This arrangement is called a multi stage of modules [21]. The first stage of the cascade provides a low temperature heat sink for the second stage which, in turn, provides a sink at an even lower temperature for third stage, and so on.

2.2. Bismuth antimony alloys for cooling applications at low temperature

2.2.1. Bismuth antimony alloys as thermoelectric materials

The bismuth rich $\text{Bi}_{1-x}\text{Sb}_x$ alloys are n-type thermoelectric materials without doping impurities and work well for low temperature cooling applications. Smith and Wolfe in 1962 [31] reported that the thermoelectric properties of $\text{Bi}_{1-x}\text{Sb}_x$ alloys and their thermoelectric performance are better than Bi_2Te_3 compounds, which have the best TE performance at temperatures lower than 220°K . These researchers found that the figure

of merit (z) increased from $1 \times 10^{-3} / ^\circ\text{K}$ at 300°K to the maximum of $5.2 \times 10^{-3} / ^\circ\text{K}$ at 80°K in 12% antimony single crystal alloy without doping. Yim and his colleague in 1972 reported a higher value of $6.5 \times 10^{-3} / ^\circ\text{K}$ at 80°K with $\text{Bi}_{85}\text{Sb}_{15}$ single crystal alloy and $11 \times 10^{-3} / ^\circ\text{K}$ at 100°K in a transverse magnetic field [14].

However, compatible p-type materials have not been found for low temperature cooling applications. Recently, the discovery of high temperature superconductors has lead to new applications of $\text{Bi}_{1-x}\text{Sb}_x$ alloys at low temperatures [15, 32, 33]. The superconductor leg, which is thermoelectrically passive, acts as the p-type leg in the cooling module and the bismuth antimony alloy acts as an n-type thermoelement. This cooling arrangement can be operated effectively at liquid nitrogen temperatures (77°K).

2.2.2. Crystal structure and phase diagram of Bi-Sb alloys

It is known that bismuth, antimony and their alloys have a rhombohedral crystal structure (spatial group R-3m) [34, 35]. As shown in the Figure 4, the unit cell is a distorted unit cube and contains one atom at the center. Every sixth plane in the structure repeats itself. This structure can also be expressed as a hexagonal type of crystal structure [36]. This type of crystal structure shows a lamellar structure which has the tendency to easily cleave along trigonal planes (basal plane in the hexagonal system) [14, 37, 38]. The lattice parameters of Bi and Sb at 4.2 K are listed in Table 2 [34, 39]. P. Cucka and his colleague showed that the lattice constants of the Bi-Sb alloys varied linearly with composition depending on the atomic percent of Sb and described the variation with following equations [40]:

$$a = 4.546 - 23.84 \times 10^{-4}x, \quad c = 11.863 - 51.66 \times 10^{-4}x, \quad \text{at } 298^\circ\text{K} \quad (x \text{ is atomic percent of Sb}).$$

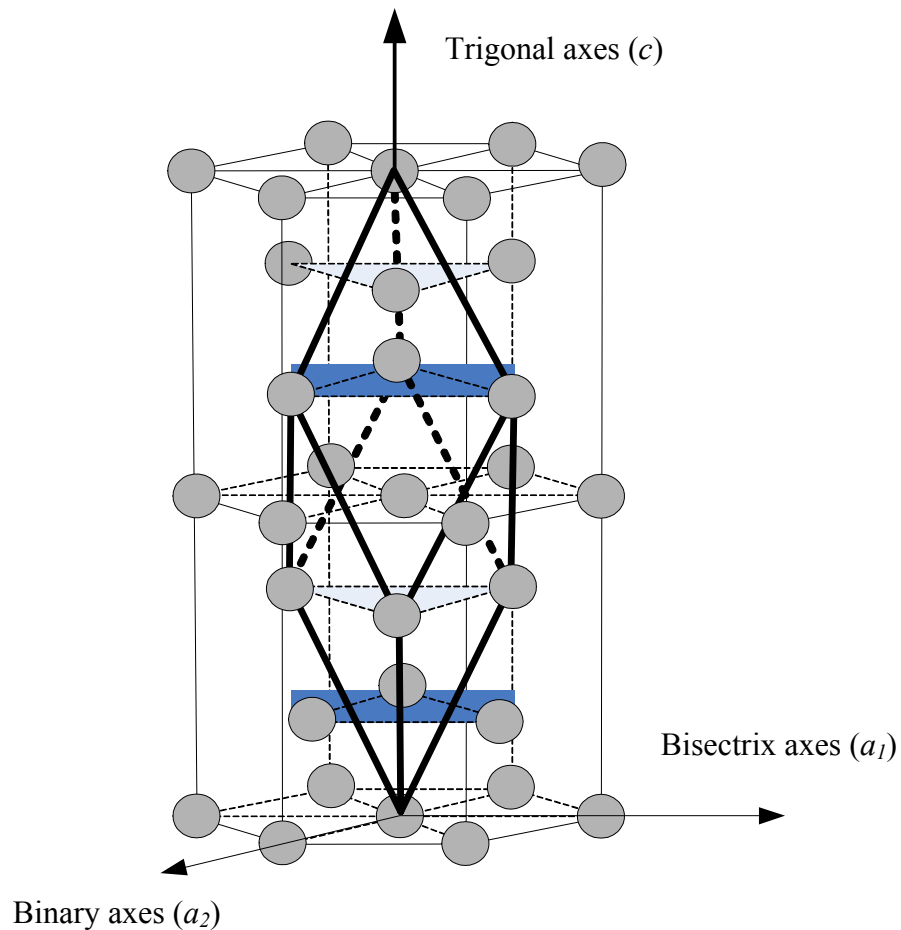


Figure 4. Crystal structure of rhombohedral bismuth and antimony [34]. The circles representing atoms can be either Bi or Sb structures of complete solubility between these two elements.

Bismuth and antimony make complete solid solutions through out the entire composition range as shown in Figure 5 [41]. The binary phase diagram shows a large temperature difference between the liquidus and the solidus line which results in macro- and micro-segregation in samples solidified from the melt. The tendency to segregate

Table 2. Crystal structure parameters of Bi and Sb at 4.2 °K [34, 39].

Materials		Bi	Sb
Lattice constants in hexagonal system	a (Å)	4.5332	4.3007
	c (Å)	11.7967	11.2221
Rhombohedral system	a(Å)	6.3081	5.998
	angle	57.19	57.14

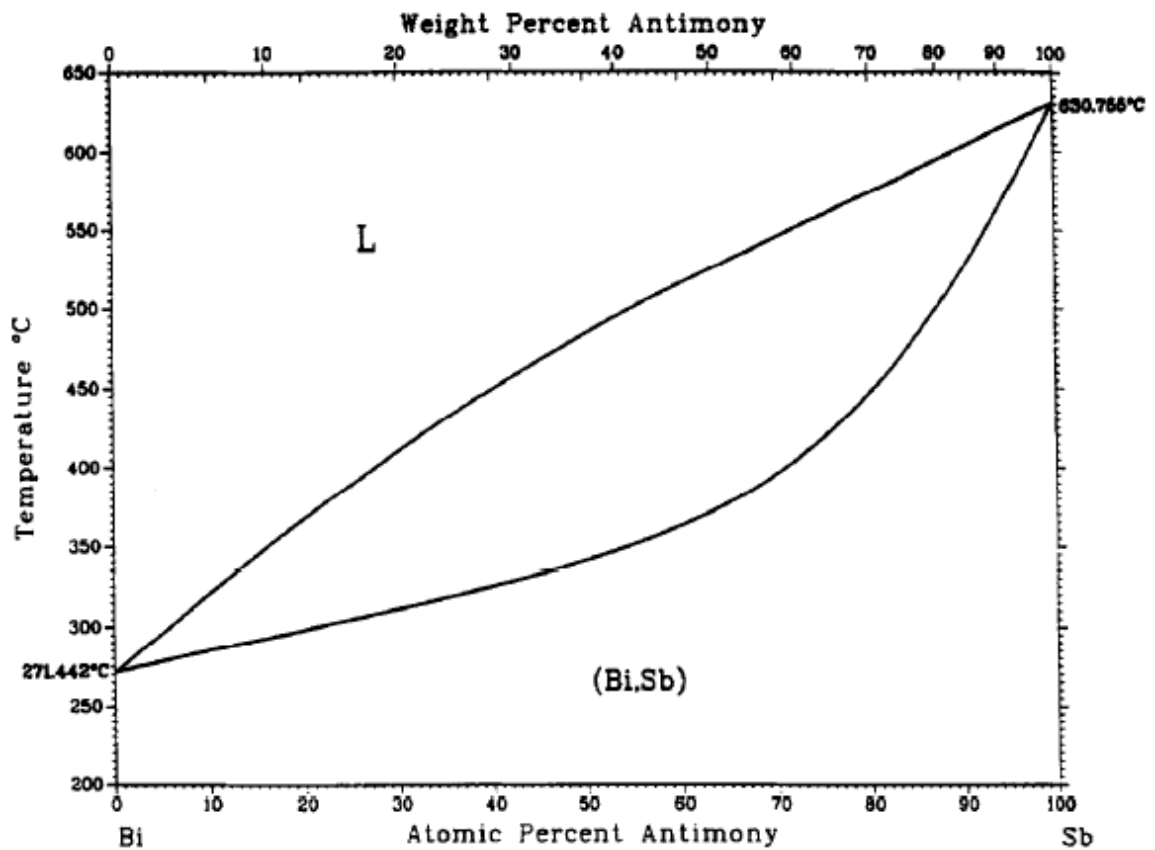


Figure 5. Binary phase diagram of the bismuth antimony alloy system [41].

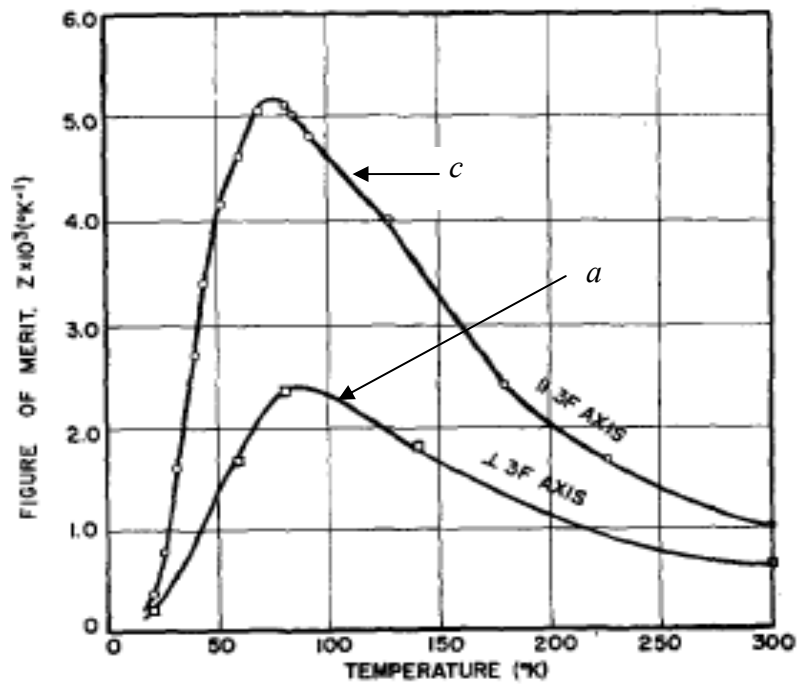
makes it difficult to produce chemically homogeneous single crystals or poly-crystals of $\text{Bi}_{1-x}\text{Sb}_x$ alloy. Chemically inhomogeneous $\text{Bi}_{1-x}\text{Sb}_x$ alloys have poor thermoelectric properties because of a mixture of semiconductor and semimetal properties.

Various techniques for making homogeneous single crystals are used, a zone-leveling technique [14, 31, 38, 42], a traveling heater method [41, 43], and a (modified) Czochralski method [44-46]. All the techniques for producing high quality of $\text{Bi}_{1-x}\text{Sb}_x$ alloy single crystal require elaborate effort and time.

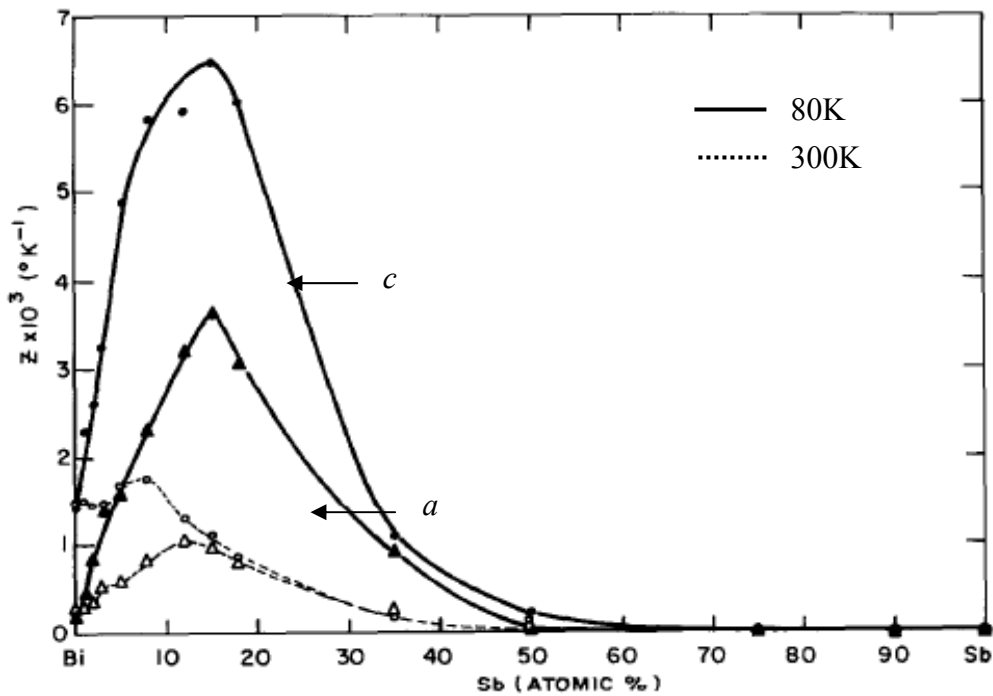
2.2.3. Anisotropic properties of Bi-Sb alloy

The single crystals of $\text{Bi}_{1-x}\text{Sb}_x$ alloy show strong anisotropic thermoelectric properties. The thermoelectric figure of merit parallel to the trigonal axis (c axis) is higher than that along the perpendicular axis to the trigonal axis (a axis). Smith et al. showed that the thermoelectric figures of merit show anisotropy from 20°K to 300°K in a pure and undoped $\text{Bi}_{88}\text{Sb}_{12}$ alloy which was fabricated by a zone leveling technique, as shown in Figure 6 (a) [31]. The figure of merit along the c axis rises from $1.0 \times 10^{-3} / ^\circ\text{K}$ at 300 °K to $5.2 \times 10^{-3} / ^\circ\text{K}$ at 80 °K and then drops sharply at lower temperature. The figure of merit along the a axis shows similar trends but the values are smaller. The researchers believe that the anisotropy in the figure of merit is caused by the anisotropy of Seebeck coefficient.

W.M. Yim et al. extensively studied the anisotropy of thermoelectric properties through the entire alloy compositions over the temperature range of 80 to 300 °K. Figure 6 (b) illustrates the anisotropy of the figure of merit through the entire Bi-Sb composition [14]. The largest thermoelectric figure of merit occurs in Bi-rich alloy along



(i)



(ii)

Figure 6. The anisotropic figure of merit for single crystal material measured along the a and c directions (i) the temperature range 20 to 300 $^{\circ}\text{K}$ for $\text{Bi}_{88}\text{Sb}_{12}$ [31] and (ii) for the entire Bi-Sb alloy composition [14].

the *c*-axis, and at low temperatures. Yim and his colleague believe that the additions of Sb into Bi cause larger Seebeck coefficients and the alloying reduced the lattice thermal conductivity. Their work shows that the highest figure of merit was $6.5 \times 10^{-3} / ^\circ\text{K}$ at 80 °K with $\text{Bi}_{85}\text{Sb}_{15}$ alloy (see figure 6 (b)). Thus, a properly oriented grain microstructure is preferred for thermoelectric applications of polycrystalline $\text{Bi}_{1-x}\text{Sb}_x$ alloys.

2.2.4. Mechanical properties of Bi-Sb alloy

The mechanical properties of Bi-Sb single crystals, including their low bending strength and tensile strength, restrict their applications for thermoelectric cooling devices. The main reason for poor mechanical properties is that the Bi-Sb single crystal is rhombohedral. However, it is represented as a hexagonal closed packed crystal structure and easily cleaves along the basal plane as described in an earlier section. The brittleness of the thermoelectric material makes its fabrication into final products difficult [33].

There have been many attempts to improve the mechanical properties without deterioration in thermoelectric properties. Sidorenko and coauthors reported on extrusion of single crystals in order to improve mechanical properties [16, 33]. In the polycrystalline ceramic materials, it is well known that mechanical properties such as toughness and strength can be improved by the reduction of grain size and development of a uniform microstructure [47]. The use of polycrystalline thermoelectric materials with a finer and more homogeneous grain size will reduce the cleavage problem because fine grains should make crack propagation more difficult.

2.2.5. Manufacturing of polycrystalline thermoelectric materials

Powder metallurgy and hot pressing are currently used techniques for producing Bi-

Sb polycrystalline material because powder is easy to synthesize, fabricate, and handle compared to fabrication of single crystals. There are several ways to obtain Bi-Sb powder alloys: mechanical alloying [17], arc plasma spraying [18], and grinding of zone-melted single crystal ingots [48]. These powder-processing techniques are all similar. Raw granular thermoelectric materials are placed in a jar with milling balls to produce fine powders. The jar is oriented with its axis horizontal and physically rotated to grind and mix the materials in an inert gas environment. The final particle size is determined by mixing time, speed of rotation of the jar and ball-powder ratio. The mixed and ground powder is sieved, then pressed and sintered or deformed at elevated temperature to produce solid thermoelectric material.

Martin-Lopez and colleagues extensively studied the effects of microstructure on thermoelectric properties for mechanically alloyed Bi-Sb powders [17, 19, 49, 50] and ultrafine powders produced by arc plasma spraying [51, 52]. The highest figure of merit of the sintered $\text{Bi}_{85}\text{Sb}_{15}$ alloy was $1.4 \times 10^{-3} / ^\circ\text{K}$ at 170°K and the value of an extruded sample showed $2 \times 10^{-3} / ^\circ\text{K}$ at 150°K . Compared to single crystals, the temperature for the maximum value shifted from 70°K towards a higher temperature range ($140 \sim 170^\circ\text{K}$) [19]. The authors concluded that samples manufactured by conventional area reduction extrusion showed better thermoelectric performance than material processed by sintering because extrusion introduces stronger texture. They believe that the extrusion process causes the trigonal axes to align perpendicular to the extrusion direction. Another study for comparison between sintering and hot extrusion was conducted by Yong-Hoon Lee et al. [20]. The extrusion sample showed better thermoelectric properties because the

extrusion process improved grain orientations compared to sintering.

Martin-Lopez and colleagues also studied the thermoelectric effect of grain size in $\text{Bi}_{86.5}\text{Sb}_{13.5}$ alloys [51, 52]. They produced ultrafine powders using evaporation of Bi-Sb pre-alloyed ingots in an arc plasma under an Ar- H_2 atmosphere and made samples using cold pressing and sintering. They claimed that a mean grain size of $2.5\mu\text{m}$ showed a better thermoelectric figure of merit among mean grain sizes of 0.1, 0.8, and $200\mu\text{m}$ for temperatures higher than 150K. The maximum figure of merit for the sample of a mean grain size of $2.5\mu\text{m}$ was 2×10^{-3} /K. They believe that phonon scattering at the grain boundaries induces a decrease in thermal conductivity in very fine grained material. Electrical conductivity also decreases when the grain size diminishes which results in a decrease in thermoelectric figure of merit.

The polycrystalline Bi-Sb alloys are preferable to single crystal from the viewpoint of mechanical strength, but polycrystalline alloys have reduced values of figure of merit. The polycrystalline Bi-Sb alloys are still being studied with various techniques for improving thermoelectric properties and ease of fabrication. Optimized material compositions and fabrication techniques are necessary for improving the performance of thermoelectric materials, reliability of thermoelectric devices, and reducing production costs.

2.3. Plastic deformation of hexagonal closed packed (hcp) metals

2.3.1. Deformation mechanisms of hcp metals and alloys

The deformation mechanisms of hexagonal close packed (hcp) metals are complicated because of the diversity of possible deformation slip modes [1]. In addition

to the slip modes, lattice rotations tend to occur with increasing deformation. Twinning causes spontaneous large-scale lattice rotations even for low degrees of deformation [53, 54]. Plastic deformation in polycrystalline materials is much more complicated than it is in single crystals. Each crystal undergoes large deformations which allow it to conform to change in a coordinated way with its neighbors. One single slip mode in polycrystalline materials is not enough for extensive deformation.

There are several slip modes for plastic deformation in hcp metals: basal slip (001) $\langle 110 \rangle$, prismatic (100) $\langle 110 \rangle$, pyramidal (101) $\langle 110 \rangle$, and twinning modes [55, 56]. These different slip modes show different deformation character depending on the material. One good example is the brittleness of hcp metals. Zinc, magnesium, cadmium, and beryllium show brittle behavior, whereas titanium and zirconium show ductile behavior. The cleavage plane for the former group of metals is the basal plane but the later materials activate various slip planes such as pyramidal or prismatic slip plane in addition to basal slip [57].

In addition to the various deformation slip modes, another important factor with regard to plastic deformation mechanisms in hcp metals is the c/a ratio [1, 58]. The distance a equals the distance between atoms in the basal plane, while c is the vertical distance between atoms in every other basal plane. If the atoms of hcp metals are ideally spherical in shape, the ratio c/a is 1.633. However, the ratio c/a varies with different materials and can be used to categorize materials as those with c/a ratio greater 1.633 ($c/a > 1.633$), similar to 1.633 ($c/a \approx 1.633$), and smaller than 1.633 ($c/a < 1.633$). The ratio c/a of cadmium and zinc is larger than 1.633, in magnesium and cobalt the ratios

are similar to 1.633, and beryllium, titanium, and zirconium have a smaller than the ideal ratio ($c/a \approx 1.633$).

Typical cold rolled texture of hcp metals are categorized by the c/a ratios as shown in Figure 7 [59]. Metals alloys with c/a ratios above the ideal ratio ($c/a > 1.633$) tend to exhibit textures with basal poles tilted ± 15 to 25 degrees away from the normal direction toward the rolling direction in Figure 7 (i). Metals alloys with c/a ratios similar to the ideal ratio ($c/a \approx 1.633$) tend to form [001] fiber textures in Figure 7 (ii). Metals alloys with c/a ratios below the ideal ratio ($c/a < 1.633$) tend to form textures with basal poles tilted ± 20 to 40 degrees away from the normal direction toward the transverse direction in Figure 7 (iii). However, the categorization by c/a ratio for texture development of hcp materials is only an approximate approach because other factors affect deformation texture. Strain rate, deformation temperature, initial texture, chemical compositions, alloying variation, and impurities can influence the texture.

2.3.2. Dynamic recrystallization in materials undergoing large deformation

Recrystallization is a common microstructure transformation in plastically deformed metals subjected to appropriate heat treatment. Generally speaking, some fraction of energy is stored after cold working and recrystallization produces a new set of strain free grains [60]. The annealing temperature for recrystallization is normally $\sim 0.3T_m$ for pure metals and as high as $0.7 T_m$ for alloys, where T_m is melting temperature.

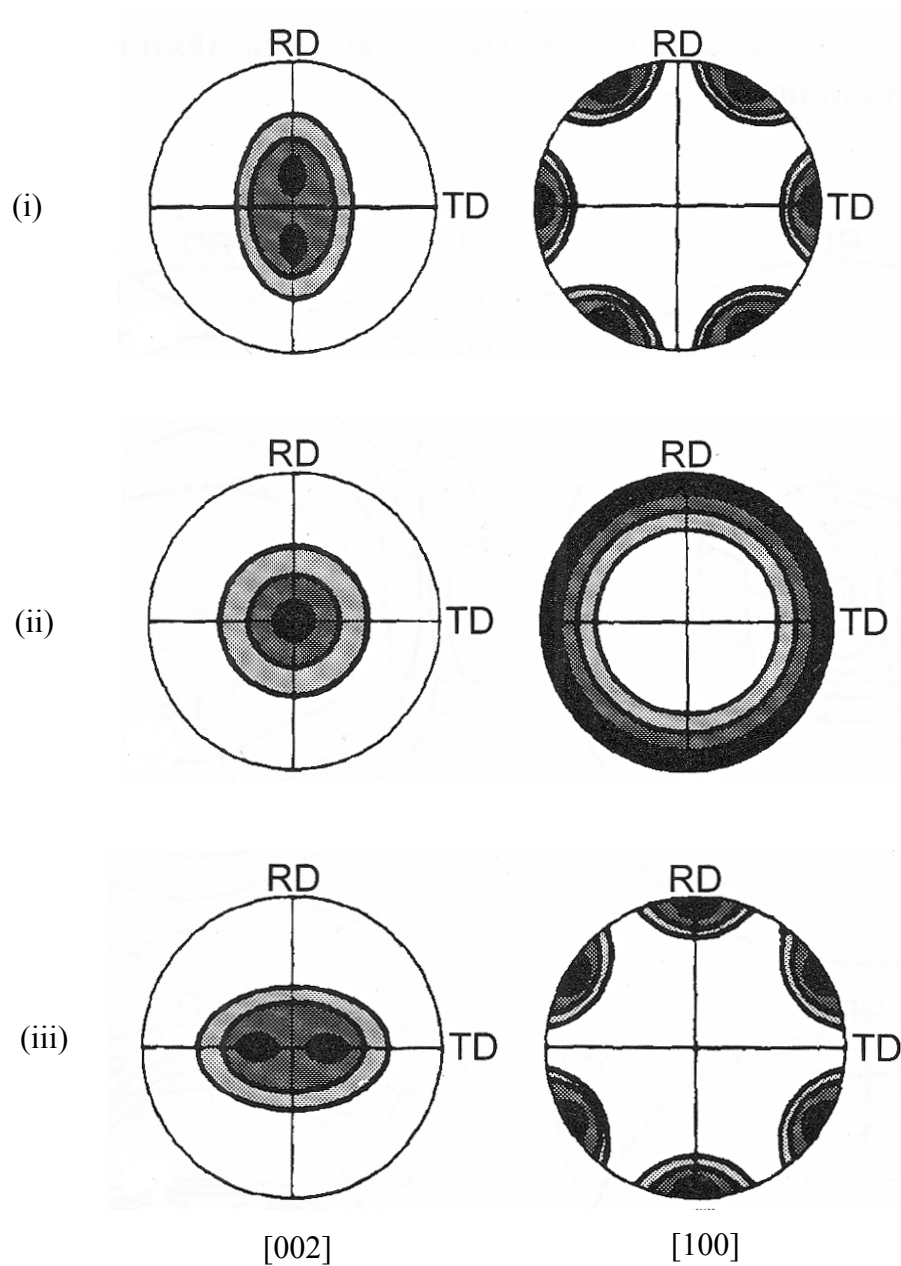


Figure 7. Schematic pole figures of [002] and [100] rolling texture in hcp metals depending on the c/a ratios of (i) $c/a > 1.633$, (ii) $c/a \approx 1.633$, and (iii) $c/a < 1.633$ [59].

The workability of hcp metals and minerals is poor because of lack of slip systems compared to cubic metals. The poor workability can be enhanced by raising the working temperature. Dynamic recovery and recrystallization reduces the flow stress and raises the ductility of materials at elevated deformation temperatures. Simultaneously, the microstructure changes to finer grains [61-66]. Generally speaking, it is known that a small new set of recrystallized grains forms at the vicinity of old grain boundaries during deformation. The mechanisms of dynamic recrystallization are studied well by several researchers with polycrystalline magnesium [67-69]. Drury et al. described the development of new grains by dynamic recrystallization by three basic processes: sub-grain rotation, strain induced grain boundary bulging, and sub-grain growth.

The three basic dynamic recrystallization mechanisms are as follows: First, sub-grain boundaries develop by the progressive increase in misorientation in grains as strain increases. Then, the sub-grains or sub-grain clusters form new high angle grain boundaries by sub-grain rotations. Second, the strain induced grain boundary bulge induces local grain boundary migration. The driving force for grain boundary migration by bulge is considered to be a difference in dislocation density or substructure development across the pre-existing grain boundary. The strain free bulge forms new high angle boundaries and develops into new grains during deformation. Third, new grains can be formed by sub-grain growth in the areas with large gradients of strain and orientation, such as deformation bands, transition bands, twins and near large phase particles. However, in many cases new grains are developed by some combination of two or all three of these processes.

2.4. ECAE processing to achieve severe plastic deformation

2.4.1. Introduction to ECAE processing

Equal channel angular extrusion (ECAE) is a processing method for producing intense plastic strain in bulk metallic materials. The basic principles of ECAE are shown in Figure 8 [3-6, 10]. The extrusion die consists of two channels which are called inlet and exit. Both channels have almost the same cross-sectional area and are connected at an angle of 90° . The work piece is put into the inlet channel and leaves through the exit channel. The work piece experiences simple shear at the intersection of the channels,

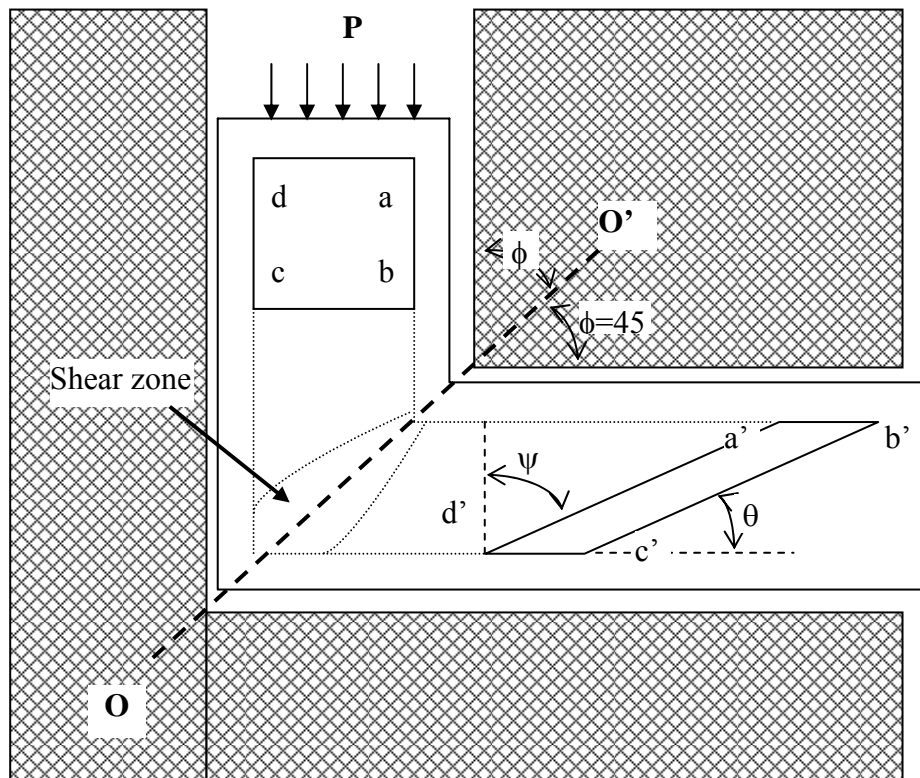


Figure 8. Schematic view of the equal channel angular extrusion (ECAE) process.

which is called the shear zone.

When a work piece passes through the shear zone, the billet is deformed such that an originally square material element, $abcd$, is transformed to the sheared parallelogram $a'b'c'd'$ at the channel crossing plane ($O-O'$) as shown in Figure 8. The cross-sectional area of the work piece is nearly the same before and after extrusion. This circumstance makes possible repeated extrusions by small modifications to the billet dimensions. The accumulated shear, γ , caused by multipass extrusions and occurring at the crossing plane is equal to:

$$\gamma = (2/\sqrt{3}) N \cot \phi \quad (4)$$

The term, N , refers to the number of extrusion passes and ϕ is the half angle between the inlet and exit channels.

Severe plastic deformation via ECAE is known as an effective method for microstructure refinement of metallic materials. Carefully applied multipass extrusions coupled with recrystallization heat treatment can produce fine and homogeneous grain morphology in bulk metallic materials [70-72]. The nomenclature to describe the multipass deformation routes is as follows: route A: no work-piece rotation about the billet axis between the passes; route B (or B_A): clockwise 90° rotation of the work piece, following by anti-clockwise 90° rotation on the next pass or vice-verse; route C' (or B_C): 90° clockwise rotations between passes; and route C: 180° rotations between passes. Schematic illustrations showing the second pass for routes A, B, and C are given in Figure 9 for the second pass. During multipass ECAE processing microstructure

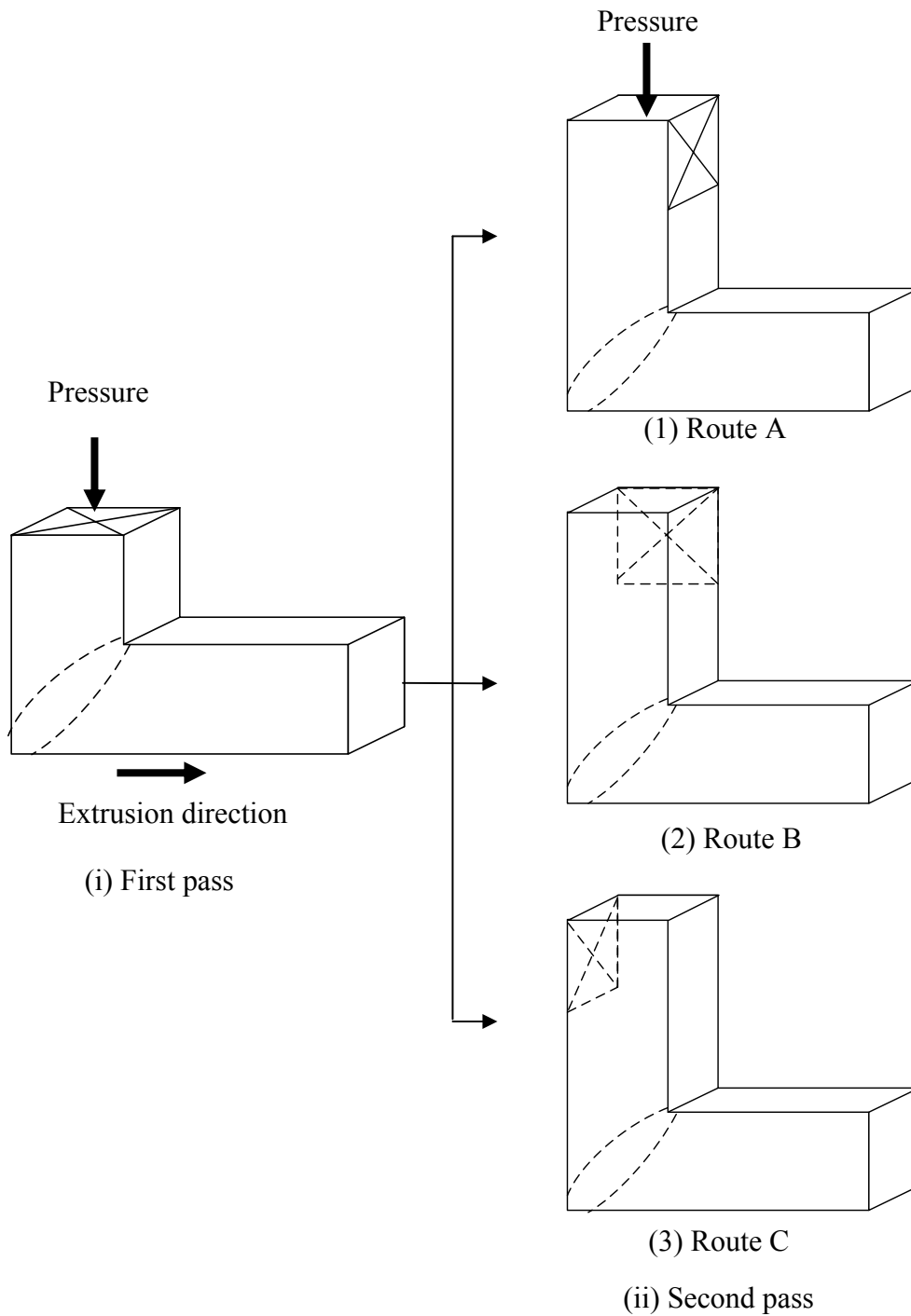


Figure 9. Schematic illustration of extrusion routes: (i) first pass (ii) second pass, (1) route A is without rotation, (2) route B is with 90° rotation with respect to the extrusion axis prior to the second pass, and (3) route C is with 180° rotation with respect to the extrusion axis between passes.

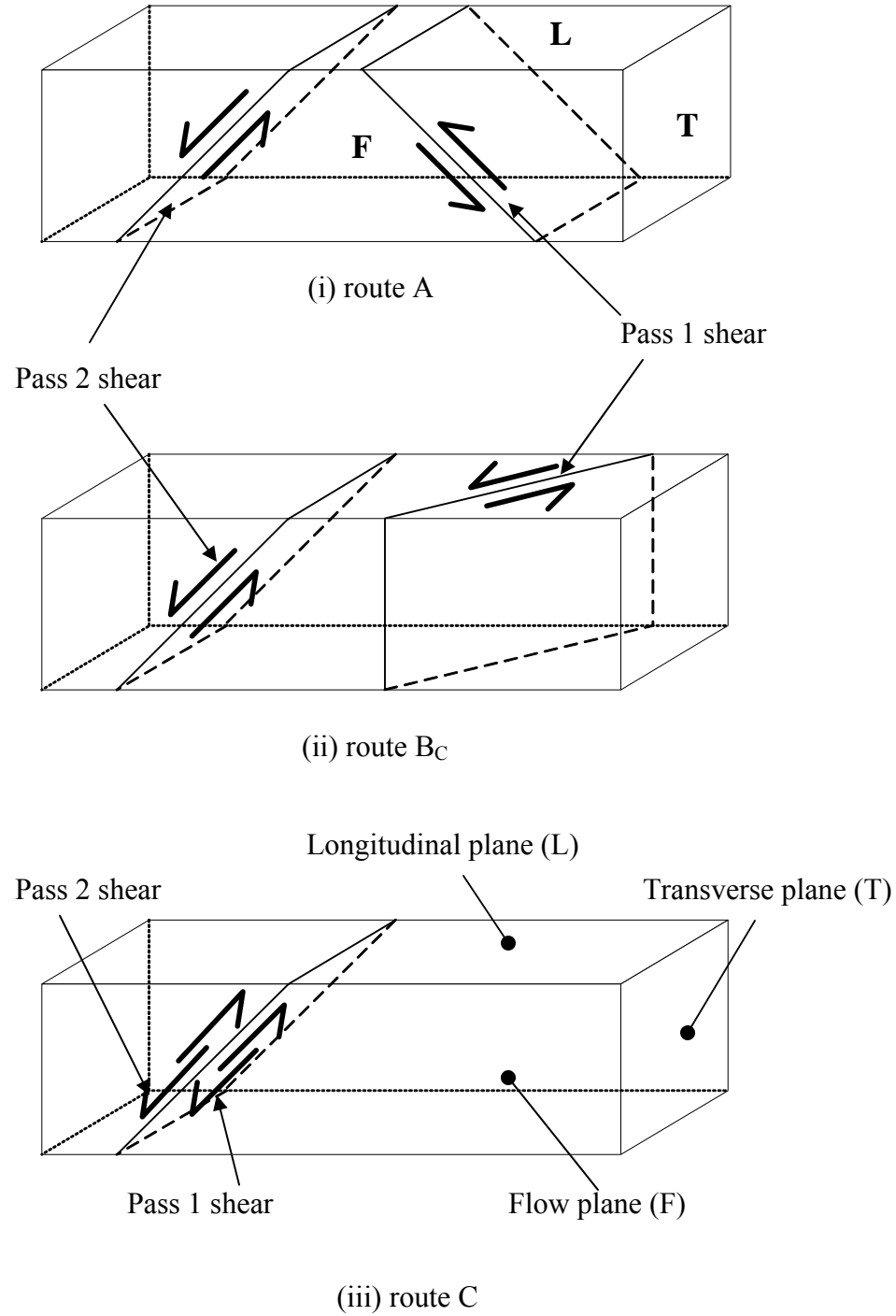


Figure 10. Schematic views of shear planes and shear directions for routes: (i) route A, (ii) route B_C, and (iii) route C. (The longitudinal (L) plane, transverse (T), and flow (F) planes are defined in illustration (iii).

refinement and texture evolution are dependent on the billet orientation between the extrusion passes and the number of extrusions. The schematic views of shear planes and shear directions are shown in Figure 10. The intersection of shear planes is an important factor for improving effective microstructure refinement [2, 70, 73].

2.4.2. ECAE processing of hcp materials

Recently there have been several ECAE studies of microstructure refinement and texture evolution for non-cubic materials, such as beryllium [7], zinc alloy [74, 75], titanium [9, 76-81], titanium alloy [11, 82, 83], zirconium [8, 84-87], magnesium [88], magnesium alloy [89-92]. Extrusions for these hexagonal closed packed (hcp) metals were carried out in a warm or hot ECAE die and sometimes with back pressure to avoid shear fracture during extrusion. Semiatin et al. studied on the workability of materials such as pure titanium, AISI 4340 steel, and Ti-6Al-4V alloy [11]. These difficult-to-work materials showed shear localization and shear failure during non-isothermal ECAE processing. Lee et al. used an ECAE die angle of 120° between inlet channel and exit channel for processing commercial purity zirconium at room temperature [86, 87]. Nagasekhar used an ECAE die with an angle of 150° to process commercially pure titanium [93].

Most of these studies concentrated on grain refinement and improvement of mechanical properties. Stolyarov and his colleagues conducted eight pass ECAE processing (route B_A and B_C) on commercial purity Ti at the temperatures between $400 \sim 450^\circ\text{C}$ [76]. They concluded that route B_C showed the most effective for microstructural refinement.

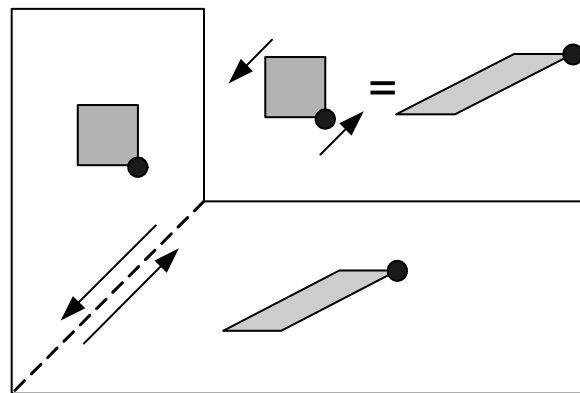
Mukai et al. proposed a texture development mechanism in AZ31 magnesium alloy processed by the ECAE [89-92]. He believed, based on XRD results, that the basal planes orient to the shearing direction ($\sim 45^\circ$). He reported significantly enhanced ductility and fracture toughness at room temperature by grain refinement of the alloys. Kim et al. reported similar textures for magnesium alloy AZ61 processed by a similar method [94].

On the other hand, Agnew and his colleagues have extensively studied ECAE texture development in Mg and its alloys with multipass extrusion [95-97]. Agnew et al. did ECAE tool at temperatures of 200~300°C and applied back pressure (in the range of 58-77 MPa) in order to avoid shear failure. The results of their experiments show that the dominant c-axis fiber texture of AZ80 and AZ31 alloys is inclined approximately at 55° to the extrusion axis. The texture is strengthened by subsequent passes of route A ECAE processing but the orientation direction of the texture does not persist. They suggested that the reasons for texture strengthening through multipass extrusions are due to large rigid body rotations as shown in Figure 11. The basal slip is a dominant deformation mode and there is a small contribution of non-basal slip modes for these materials. They also suggested that various textures evolved depending on the routes, initial texture, end effects and material compositions through multipass ECAE processing.

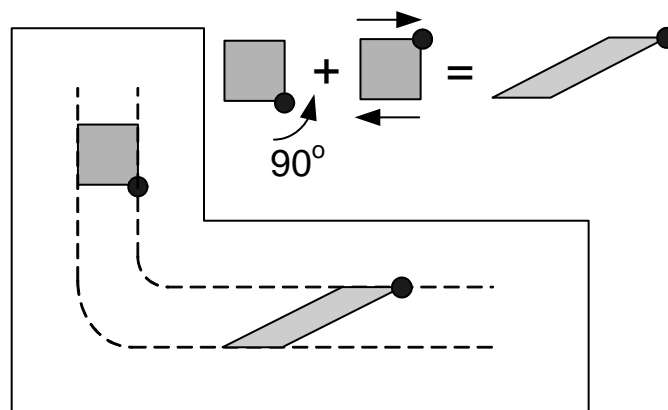
2.4.3. Materials processing of Bi_2Te_3 alloys

The crystal structure of bismuth telluride alloys is similar to bismuth antimony alloys, a rhombohedral layered structure, and it shows strong anisotropic properties. The

processing techniques for bismuth antimony alloys are compatible with bismuth telluride alloys. The processing techniques for polycrystalline bismuth telluride and its alloys are



(i) Idealized simple shear.



(ii) Element rotates and experiences simple shear along flow lines.

Figure 11. Schematic of shear deformation via the ECAE process (i) the element experiences idealized simple shear at the shear zone and (ii) the element experiences rigid body rotation (90°) and simple shear [96].

plastic deformation at elevated temperature, press sintering and mechanical alloying, to improve the thermoelectric and mechanical properties. The hot pressed sintering process and plastic deformation via hot extrusion improve the figure of merit by enhancement of grain orientation distribution in Bi_2Te_3 alloys. The figure of merit of simply sintered thermoelectric material is not good compared to single crystals due to the poor crystal orientation [98].

An effect of plastic deformation via extrusion at elevated temperature is to introduce large carrier concentrations of point defects into the lattice [99, 100]. Point defects are generated by dislocation interactions when non-basal dislocation sliding results from the deformation. The donor concentration increases as a result of non-basal dislocation sliding, depending on solid solution composition, doping impurities and doping degree [100]. However, point defects are annihilated by dislocation climb and array formation during annealing.

Other more important effects of plastic deformation via extrusion at elevated

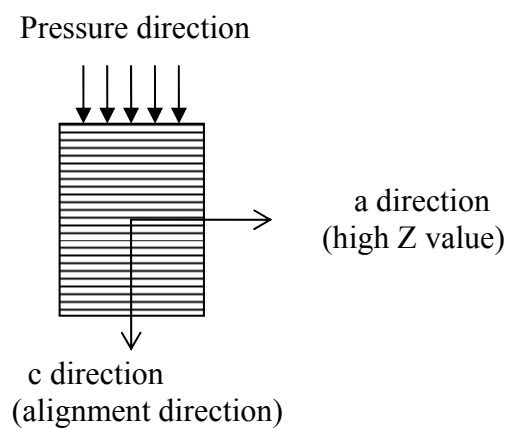


Figure 12. Pressure direction and alignment of grains in Bi_2Te_3 in the c direction.

temperatures are grain refinement and enhanced texture [101-106]. In Bi_2Te_3 and its alloys, bonding between tellurium atoms in the c plane is established by weak van der Waals forces so that pressing will cause a preferred orientation of the c axis in the pressing direction as shown in Figure 12. When powders are pressed, they slip along the cleavage planes. Each powder's c axis tends to align to the pressing direction, but it is imperfect. The powders orient their c axis with an orientation distribution. Of course, each grain is anisotropic by itself. Thus, the figure of merit in sintered materials depends on the level of texture. The orientation distribution can be determined by X-ray diffraction [101, 102].

It is known that slip, rotation, recovery and recrystallization of crystal grains occur during hot plastic deformation. Enhancement of texture yield strong anisotropic thermoelectric properties, which suggest high thermoelectric performance in the direction perpendicular to a pressing direction. The hot extruded microstructure shows highly fine and equiaxed grains that derive from dynamic recrystallization during hot area reduction extrusion [107].

2.4.4. ECAE processing of thermoelectric materials

Recently, brittle intermetallic compounds of cast p-type Bi_2Te_3 alloy were successfully processed by conventional area reduction extrusion [107] and multipass ECAE at elevated temperature [12]. Cast ingot extrusion has many advantages such as simple material preparation, easy purity retention, and energy saving compared to powder consolidation methods. It is possible to obtain grain refinement and strong texture, and therefore favorable mechanical properties and thermoelectric properties.

Large brittle cast grains were refined to equiaxed and micron sized grains through dynamic recrystallization during plastic deformation at elevated temperatures. The final grain size of ECAE processed cast p-type Bi_2Te_3 alloy is strongly dependent on extrusion temperature and the extrusion speed. An average recrystallized grain size of 10-30 μm with uniform morphology was achieved after four passes following route E (2CX2C: Two pass route C extrusion followed by rotating the work piece 90° after two pass route C extrusion) at an extrusion temperature of 500°C and a punch speed of 2.5 mm/sec. The microstructural uniformity is strongly affected by the level of strain and the orientation of strain between passes which means that intersection of shear planes is more effective for grain refinement.

Another new approach for severe plastic deformation in Bi_2Te_3 alloys is reduced area channel angular extrusion. Kim et al. processed mechanically alloyed powders (average agglomerate particle size of 125 μm) by this method through an area reduced exit channel (approximately reduction ratio of 4:1) with argon cover gas at the temperatures between 693-783K [13, 108]. Their XRD results for the processed Bi_2Te_3 alloy with reduced area exit channel show that higher intensities of basal plane peaks are present perpendicular to the extrusion direction. The authors believe that the strong texture is developed by crystal orientation rearrangement as shown in Figure 13 and the grains are refined by dynamic recrystallization during severe shear deformation at elevated temperatures. The refined grain size was about 20 μm and the improvement in mechanical strength (bending strength = 120 MPa) was six times higher than that of

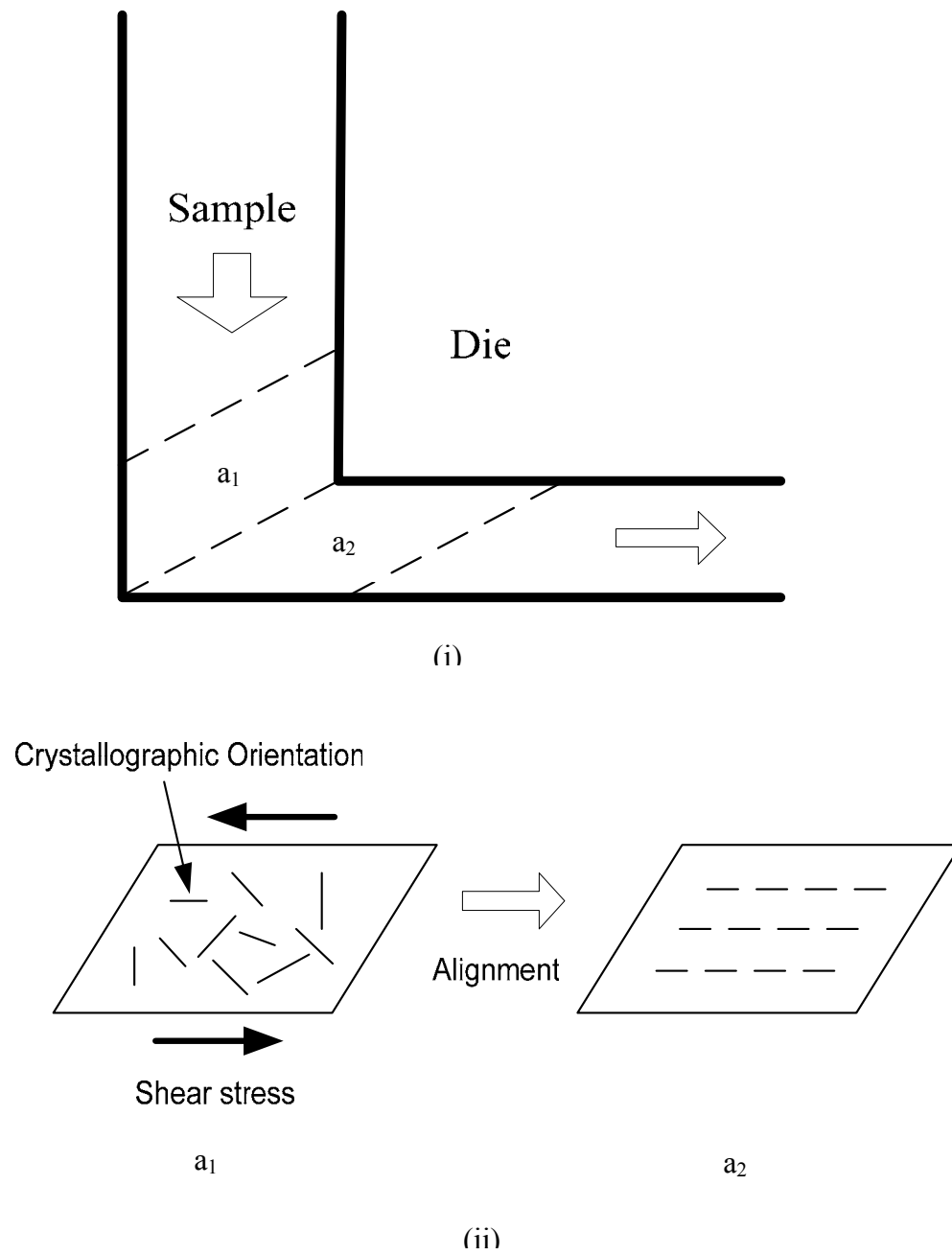


Figure 13 Schematic views of crystal orientation rearrangement during area reduction angular extrusion: (i) shear extrusion process and (ii) crystal rearrangement before (a_1) and after (a_2) extrusion [13].

unidirectional grown samples. According to inverse pole figure analysis from electron backscattered diffraction patterns, the basal planes align from 0° to 30° to the extrusion axes. The highly anisotropic processed material had almost the same electrical resistivity ($1.008 \times 10^{-5} \Omega\text{m}$) as that of single crystal material ($0.995 \times 10^{-5} \Omega\text{m}$) and the thermoelectric figure of merit for p-type material was enhanced to $3.03 \times 10^{-3} \text{K}^{-1}$.

CHAPTER III

EXPERIMENTAL PROCEDURES

According to the literature review from the previous section, multipass ECAE and reduced area exit channel extrusion can be another processing candidate for cast Bi-Sb alloys. It is expected that fine and homogeneous grain morphology can be developed by the multipass ECAE process. The texture evolution by various ECAE routes and reduced exit channel area components will give information related to how Bi-Sb alloy microstructure evolves in the shear zone. Thus, the following series experiments and analyses will be used to determine the mechanisms of grain refinement and texture evolution for cast Bi-Sb alloys via ECAE and reduced exit channel area extrusion.

3.1. ECAE processing procedures

Fifteen millimeter diameter cylindrical cast Bi-Sb ingots for experiments were supplied by Marlow Industries, Inc. The Bi-Sb cast ingot was encapsulated in a fully annealed Al 6061 can to contain the alloy to increase ductility. The Al cans were annealed at a temperature of 400°C for 2 hours and cooled in the furnace. Boron nitride lubricant was sprayed on the surface of the Al can and anti-seize Moly dry film was painted on to the ECAE tool. The composite billet was placed into the inlet channel in a heated extrusion tool and held for 10 minutes at the die temperature before extrusion. The composite bar containing the Bi-Sb ingot was extruded repeatedly through a 90 degree ECAE tool to produce a high level of strain. Small dimensional modifications of the extruded billet were necessary for consecutive extrusions.

3.2. Extrusion conditions and test matrix

The experimental test matrix is shown in Tables 3 and 4. Extrusion conditions were varied by changing the extrusion temperature (220, 235, and 250°C) and the punch speed (2.5, 7.6, and 15.2mm/min) through four passes of route Bc in order to check the level of grain refinement and dynamically recrystallized grain size. Based on the results from the series of experiments described in the Table 3, the most favorable preprocessing conditions, extrusion temperature and punch speed with route Bc, were determined.

The subsequent series of extrusions shown in Table 4 were performed to study the development of grain morphology and texture. The preprocessed materials (four pass of route Bc) were used for the test matrix in Table 4 because they provided a more uniform starting microstructure than cast material. The level of error for subsequent texture analysis was reduced by the refined starting microstructure.

The variables in Table 4 are route (A and C), number of passes (one to four) of extrusion, prior heat treatment and the exit channel reduction ratio (0, 1/4, and 1/2). Other extrusion conditions were fixed: extrusion temperature 235°C and punch speed of 0.3 in/min. One of the preprocessed billets was heat treated at 250°C for 100 hours under vacuum ($\sim 10^{-3}$ torr) and ECAE processed with four pass of route B_C only.

Schematic views of the extruded billets with a reduced area exit channel are shown in Figure 14. The dimensions of the exit channel are 3/4" x 3/4", 3/8" x 3/4", and 3/16" x 3/4" giving exit channel areas of A_{inlet} , $1/2A_{\text{inlet}}$, and $1/4A_{\text{inlet}}$ respectively. The inlet and exit channel were connected at a sharp right angle.

Table 3. Test matrix for determining the best preprocessing condition for Bi₉₀Sb₁₀ cast ingots. The chosen processing route is 4B_C.

Billet ID	Area of exit channel	Punch speed (in/min)	Extrusion Temperature (°C)	Number of extrusion passes (4B _C)
1	A _{inlet}	0.1	250	4
2	A _{inlet}	0.3	250	4
3	A _{inlet}	0.6	250	4
4	A _{inlet}	0.3	235	4
5	A _{inlet}	0.3	220	4

Table 4. Test matrix for studying texture development with preprocessed Bi₉₀Sb₁₀ alloy billets (Preprocessed conditions: 4B_C at 235°C and 0.3 in/min).

Billet ID	Area of exit channel	Punch speed (in/min)	Number of extrusion passes	Route
1	A _{inlet}	0.3	1	A
2	A _{inlet}	0.3	2	A
3	A _{inlet}	0.3	4	A
4	A _{inlet}	0.3	2	C
5	A _{inlet}	0.3	4	C
6*	A _{inlet}	0.3	4	B _C
7	1/2 A _{inlet}	0.15	1	A
8	1/4 A _{inlet}	0.075	1	A

* Heat treated billet (100 hours at 250°C under 10⁻³ torr vacuum).

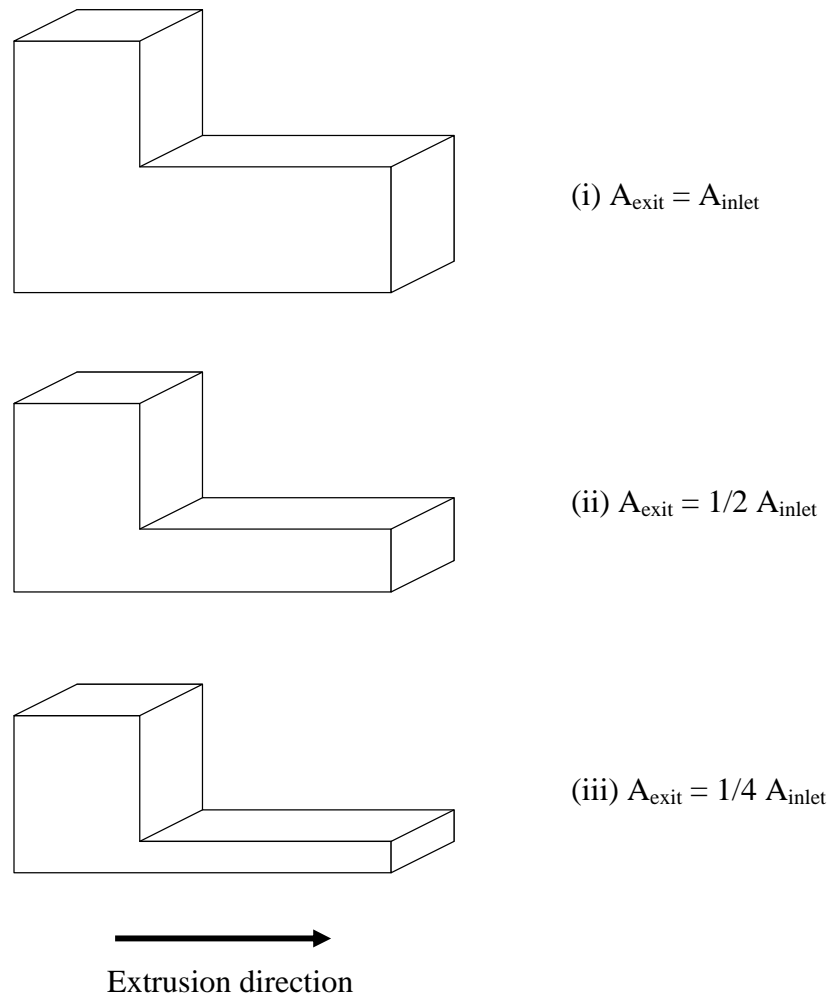


Figure 14. Schematic views of billets extruded through an exit channel with different areas: (i) same, (ii) half, and (iii) quarter the area of the inlet channel.

3.3. Sample preparation for analysis and equipments

Extruded billets were prepared for optical metallography, texture, and microprobe analysis by cutting along the longitude plane with a Buehler Isomet 1000 Saw using a

0.02inch thick diamond cut-off blade (#11-4246). Lubrication during cutting was accomplished using Isocut Plus fluid. The cutting was carried out with necessary care (slowly). Specimens were ground with SiC emery papers (400, 600, 800 and 1000 grit sizes) and finally polished (0.05 micron alumina - water slurry). Since the bismuth antimony alloys are easily scratched on the surface, grinding and polishing were done by hand. The samples were prepared without etching.

A Nikon (Epiphot) digital optical microscope with polarized light was used for observing the grain refinement, grain shape, and grain morphology. Digitized micrographs were obtained from a polished surface. The mean lineal intercept method was used to determine the average grain size with the micrographs taken from the fine-grain area and the standard deviation was less than 20%. Grids (approximately 30 x 5) on the digitized micrographs were used for obtaining the ratio of fine grain area to coarse grain area. The percentage of fine grain area was calculated by counting the number of grids in fine grain area out of the whole sample surface area and the estimation of error was less than $\pm 3\%$. Scanning electron microscopy (SEM) was used for examination of the fracture surface using a Zeiss 1530 high-resolution field emission scanning electron microscope (FE-SEM).

Microprobe analysis was conducted for analyzing the chemical homogeneity of initial cast ingot material and chosen extruded samples using an SX50 Cameca Electron Microprobe. Electron backscattered (EBS) images used for the analysis. Energy dispersive spectroscopy (EDS) and wavelength dispersive spectroscopy (WDS) were used for qualitative and quantitative analysis. The acceleration voltage and beam current

used were 15KV and 3nA respectively for electron backscattering spectroscopy and qualitative analyses with EDS. The current was raised to 10nA for quantitative analyses with WDS. A PET (Pentaerythritol) crystal was used with a take off angle of 40° for WDS. The estimation of errors for WDS analysis was less than 1 at %.

X-ray diffraction patterns and texture measurements were conducted at room temperature using a Bruker D8 DISCOVER X-ray diffraction system with $\text{Cu K}\alpha$ radiation (wave length 1.5406\AA) on the longitudinal plane of the extruded billets. Texture evolution of the Bi-Sb alloy was analyzed using the $\{0\ 0\ 6\}$ reflection plane to identify the orientation of the basal poles.

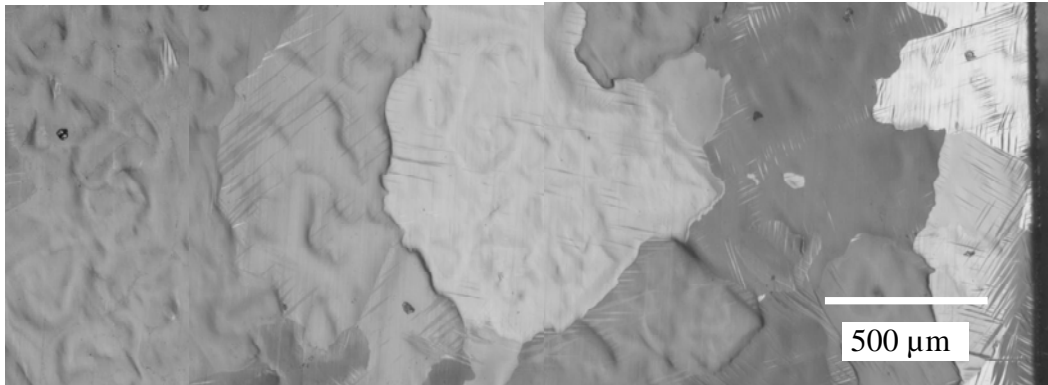
CHAPTER IV

EXPERIMENTAL RESULTS

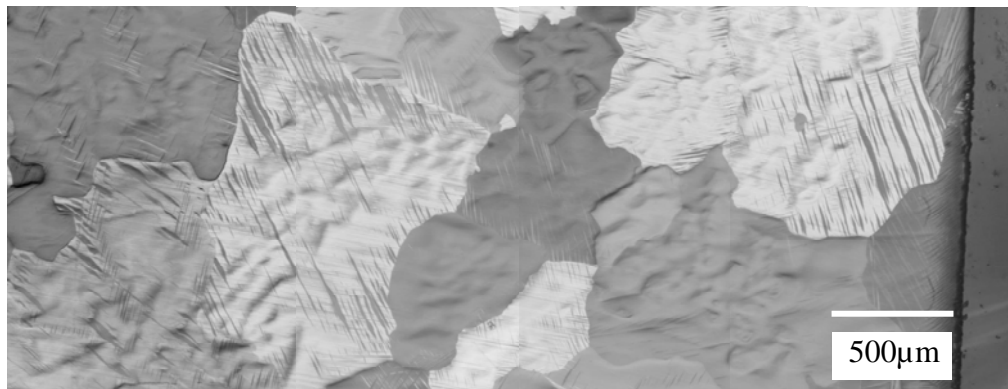
4.1. As received materials

All bismuth telluride alloy billets for extrusion were supplied by Marlow Industries. The billets were cylindrical cast bars of roughly twelve millimeter diameter with a nominal chemical composition of 90 at% bismuth and 10 at% antimony. Before the experiments, the cast Bi-Sb alloys were examined for grain structure, melting temperature, chemical homogeneity, and texture. Optical micrographs of the longitudinal and transverse sections for a cast Bi-Sb alloy are shown in Figures 15. The grain size of cast material is on the order of several millimeters. The grain shape and size in both longitudinal and transverse sections are similar indicating an equiaxed microstructure.

EDS and WDS in the cast material were performed to check chemical homogeneity. The results of qualitative EDS analysis for the sample are shown in Figure 16 and 17. Qualitative analysis of the antimony peaks from the EDS results indicates differences bright area and dark area in the EBS image as shown in Figure 16. The antimony intensity peak near the 3.6 keV in dark area is much higher than that of bright area in Figure 16, which means that there is high antimony content in dark area of the EBS image. It is clearer that the level of grayness represents the antimony contents of cast Bi-Sb alloys on the EBS image in Figure 17. The highest antimony peak shows in the dark area with the medium peak associated with the gray area and the lowest peak with



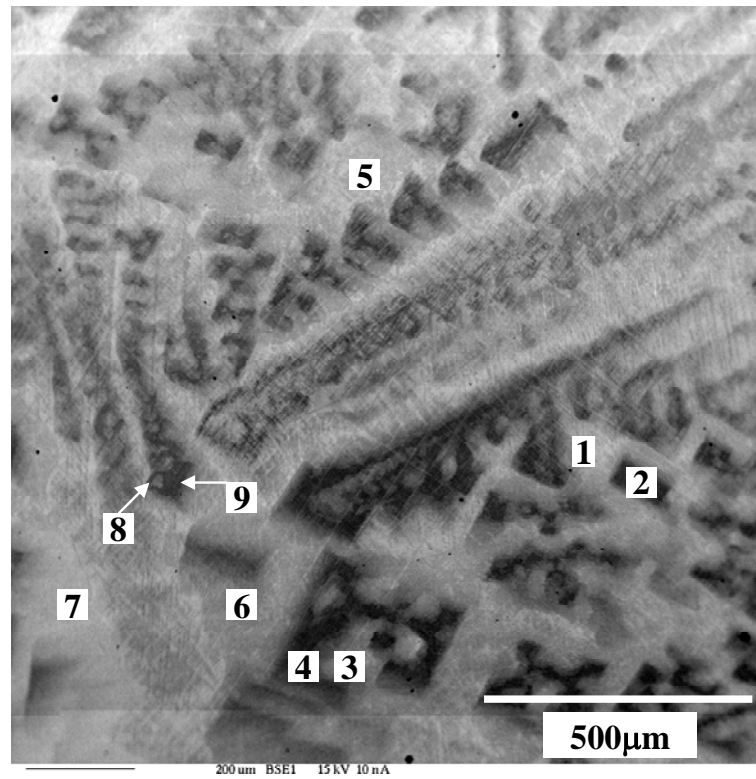
(i)



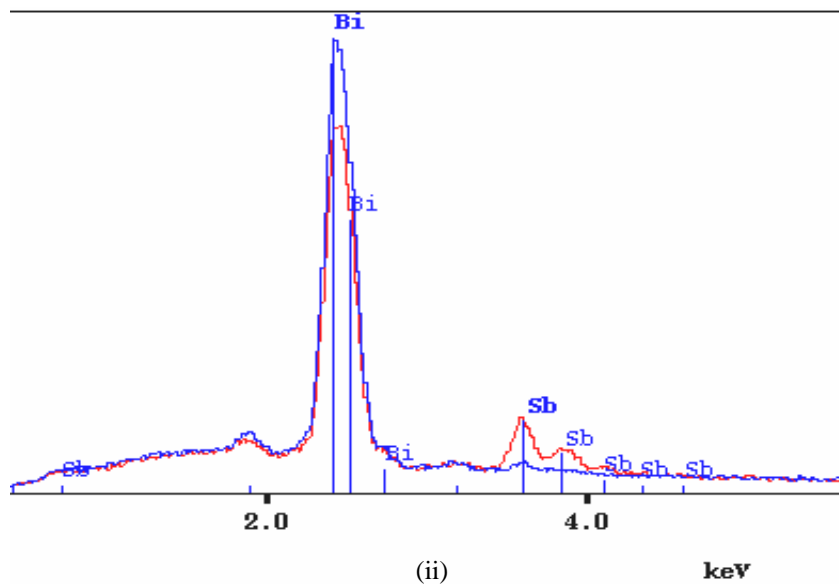
(ii)

Figure 15. Microstructures of cast Bi-Sb alloy (i) longitudinal section and (ii) transverse section.

the bright area. Basde on the EBS images and EDS results, the antimony distributions in bismuth matrix are inhomogeneous and large antimony concentration differences exist in the cast Bi-Sb alloy. Small dark areas are scattered in the bright area and the distance between the dark areas, which are high antimony concentration, varies between 50-500μm.

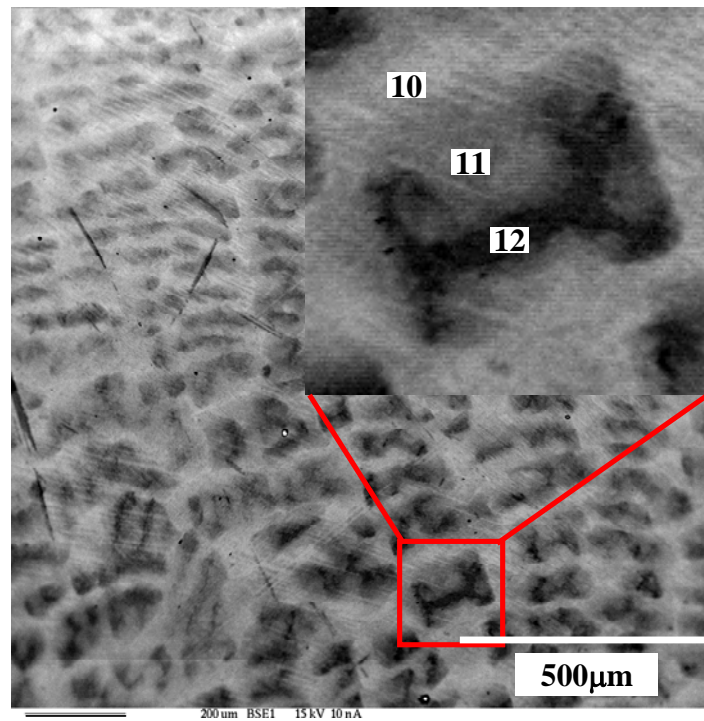


(i)

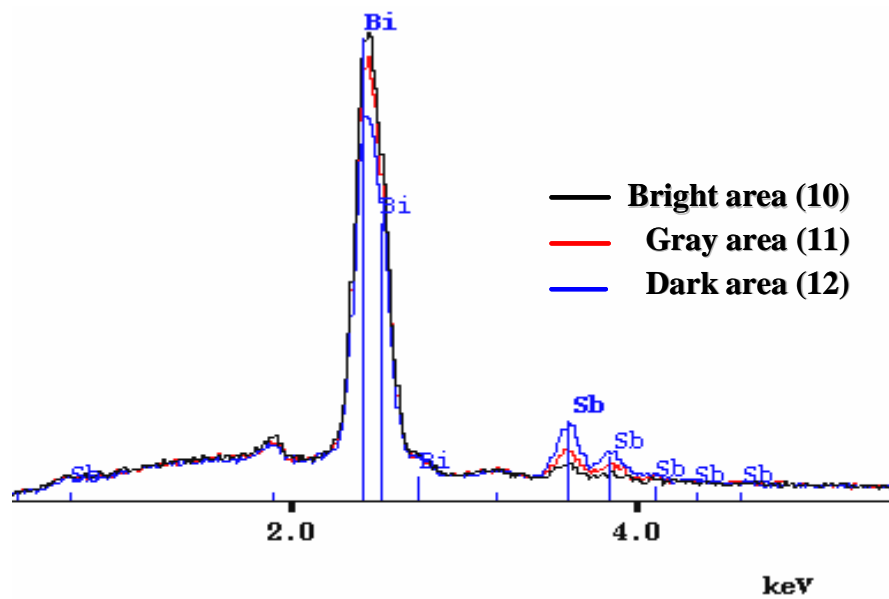


(ii)

Figure 16. Microprobe analysis with EDS for cast Bi-Sb alloy: (i) EBS image and (ii) qualitative results of bright area (1) and dark area (2).



(i)



(ii)

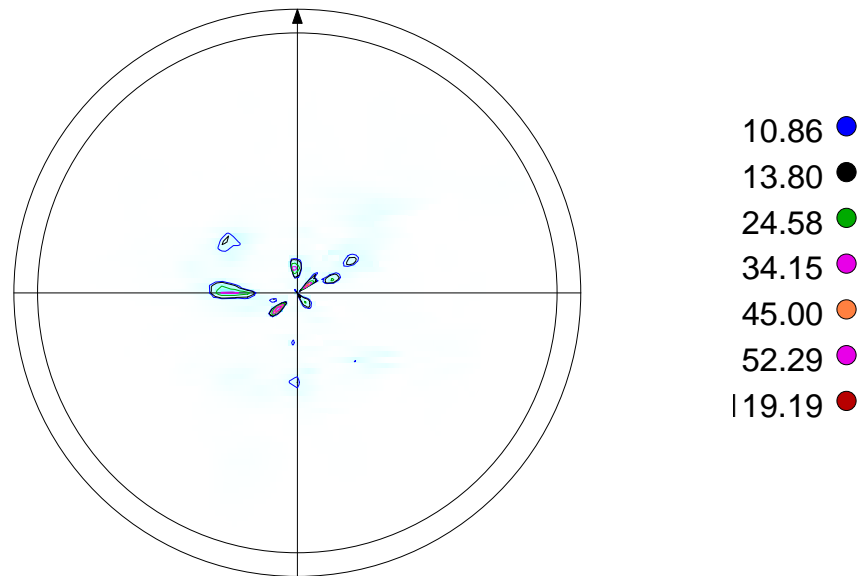
Figure 17. Microprobe analysis with EDS for cast Bi-Sb alloy: (i) EBS image and (ii) qualitative results of bright area (10), gray area (11), and dark area (12).

Further quantitative analysis of chemical composition conducted with WDS is shown in Table 5. The examined areas are numbered on the EBS images of Figure 16 and 17. The antimony content in cast Bi-Sb alloy varies from 0.2 at% to 33 at% depending on the grayness of examined area. From the WDS result, antimony content in the bright area is 0.2-3.8 at%, in the gray area it is 17.3-21.4 at%, and in dark area it is 24-33 at%. The level of grayness in the EBS images for cast Bi-Sb alloy is represented to the level of antimony content. Thus, the initial cast Bi-Sb alloy shows a large antimony gradient in the cast grains with very inhomogeneous chemical compositions.

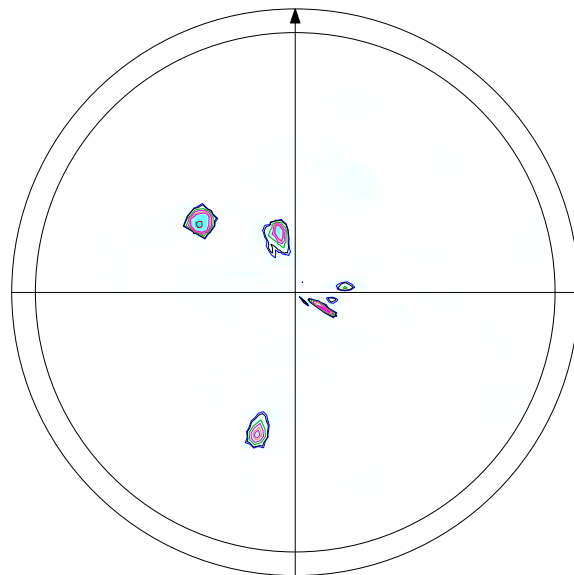
Table 5. Chemical compositions of cast Bi-Sb alloy with microprobe analysis using WDS.

Area ID	Contrast	Bi (at%)	Sb (at%)
1	Bright	98.5	1.5
2	Dark	68.0	32.0
3	Bright	96.2	3.8
4	Dark	76.0	24.0
5	Bright	99.5	0.5
6	Bright	98.8	1.2
7	Bright	99.8	0.2
8	Dark	68.7	31.3
9	Gray	78.6	21.4
10	Bright	98.8	1.2
11	Gray	82.7	17.3
12	Dark	67.0	33.0

* Measurement uncertainty is about 0.5 at%.



(i) Transverse section



(ii) Longitudinal section

Figure 18. The $\{006\}$ pole figures of cast Bi-Sb alloy for (i) transverse, and (ii) longitudinal sections.

Figure 18 shows the pole figures of a diffracting pole $\{0\ 0\ 6\}$ for transverse and longitudinal sections of cast Bi-Sb alloy. The strong basal pole is formed in various directions. It reflects that several large cast grains are dominantly oriented. As shown in Figure 19, the cast Bi-Sb alloy starts to melt near 274°C and completely melts over 330°C . This DSC result indicates that the material has the large temperature difference between the liquidus and the solidus line in phase diagram. The cast Bi-Sb alloy shows

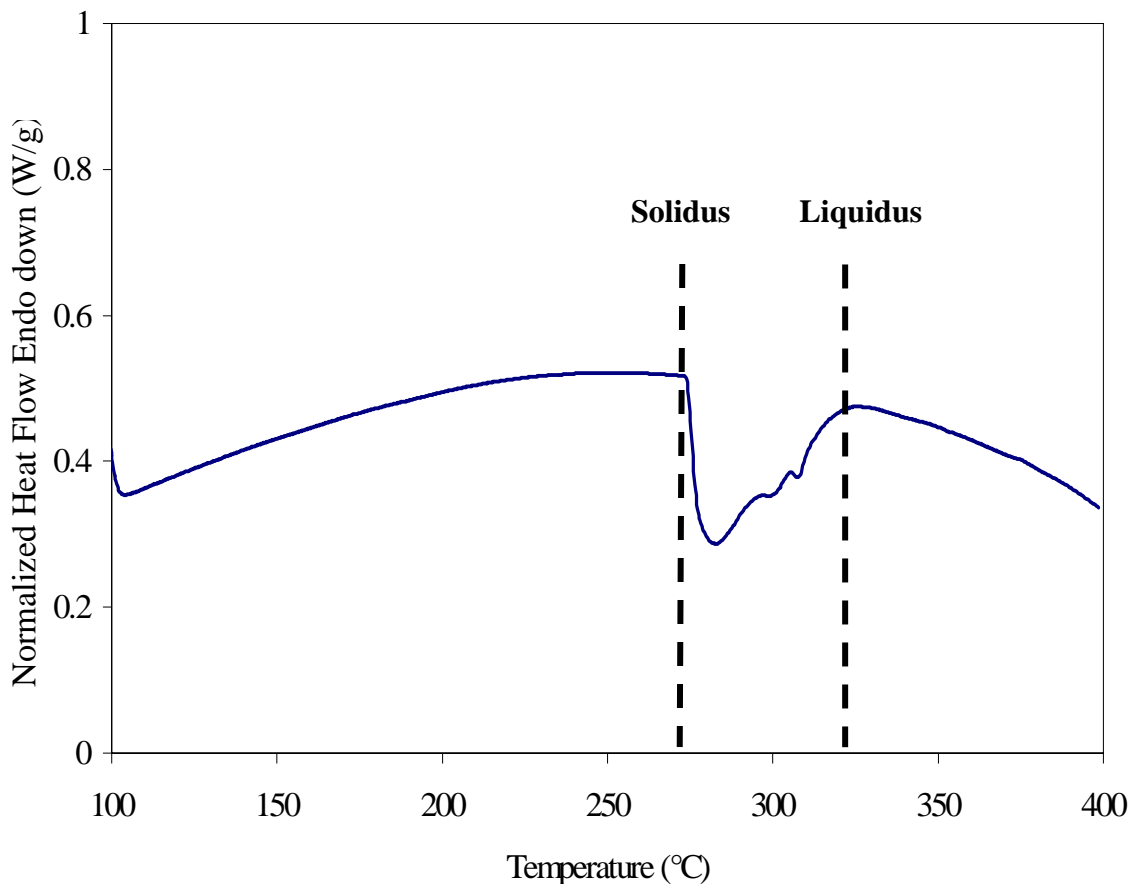


Figure 19. Thermal property of cast $\text{Bi}_{90}\text{Sb}_{10}$ alloy with differential scanning calorimeter (DSC).

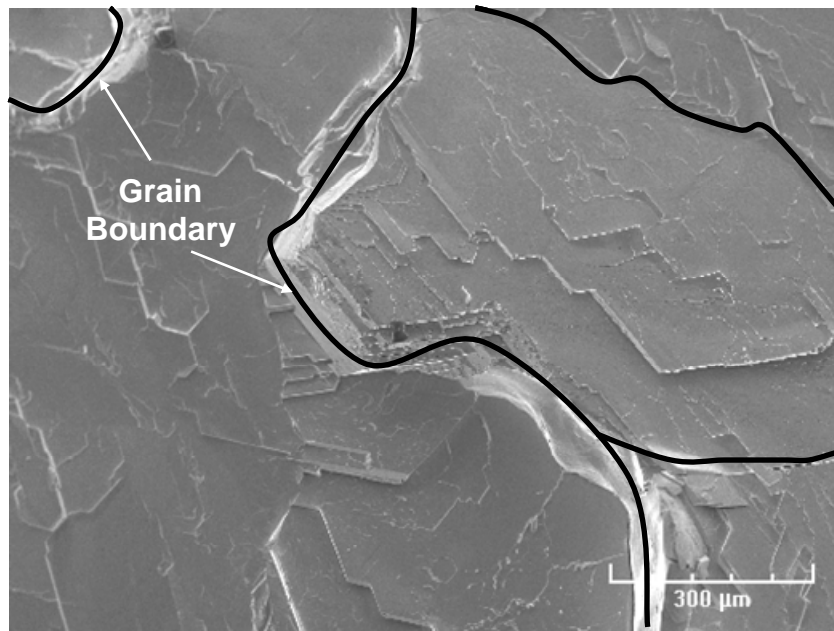


Figure 20. Fracture surface of cast Bi-Sb alloy with scanning electron microscope (SEM).

brittle fracture behavior at room temperature and the fracture occurs along the cleavage plane (basal plane). The large cast grains of layered microstructure on the fracture surface from the SEM image are shown in Figure 20.

4.2. Preliminary ECAE processing

ECAE processing was performed on the Bi-Sb alloys to check the level of grain refinement dependence on the number of extrusion pass (1~4), route (A and C), and area reduction channel angular extrusion (half and quarter area of exit area). The extrusions for preliminary experiments were carried out at the extrusion temperature 250°C and extrusion rate 0.1 in/min. As shown in Figure 21, the initial large cast grains are refined

inhomogeneously and produce bimodal grain sized microstructure after all deformation routes. Several millimeter size of cast grains break down to coarse grains (several hundred of microns) and fine grains (5~30 μm) through dynamic recrystallization. As shown in Figure 21, the fine-grain areas (grain size in area A: 10~30 μm) are formed near the edges of coarse grain (grain size in area B: hundreds of microns) boundaries. The fine grains are equiaxed in shape; the size of coarse grains varies and is of irregular shape.

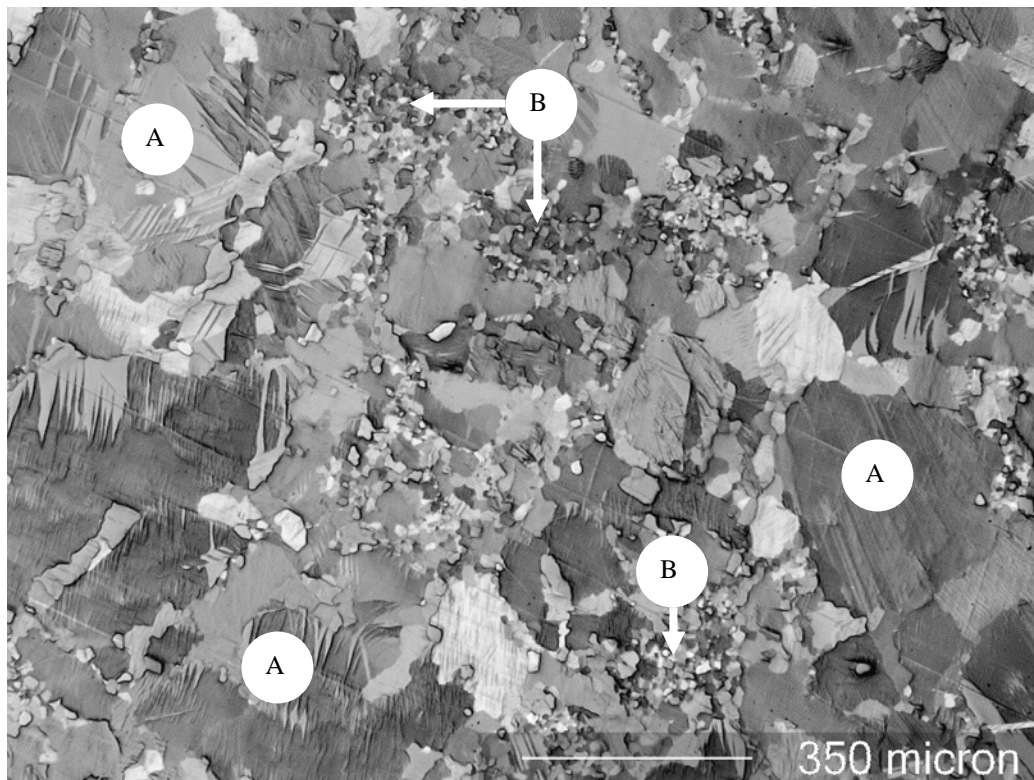


Figure 21. Microstructure development of Bi-Sb alloy after one pass via ECAE at 250°C and 0.1 in/min. Region A is coarse grain and B is fine grain area.

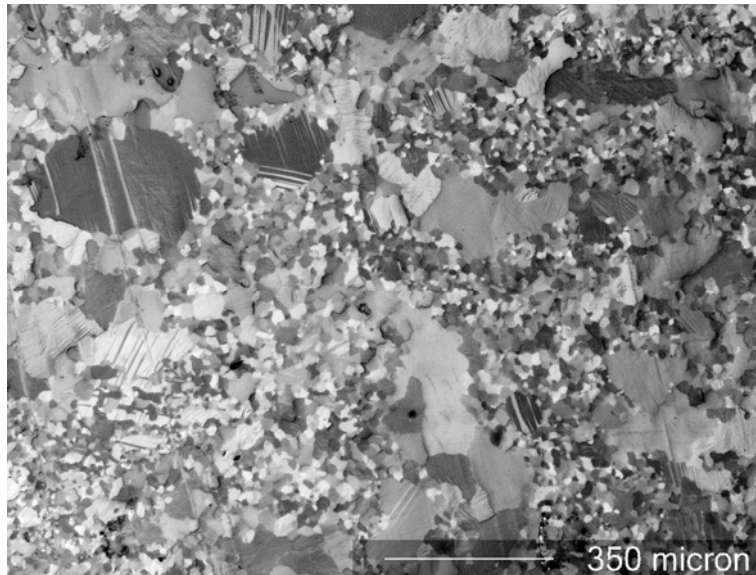
The coarse grains (several hundred of microns) are refined further after successive hot extrusions (two and four pass via route A process) as shown in Figure 22. The fine-grain area becomes larger as the number of extrusion passes increases at the expense of coarse-grain area. Though the coarse grain size reduced to 50-300 μm , the fine grain size (5-30 μm) remained similar as the number of extrusion passes increases. Coarse grains persist and bimodal a grain structure remains even after four extrusion passes via route A as shown in the Figure 22. The microstructures after four extrusion passes via route C and area reduction channel angular extrusion show similar behaviors including the bimodal grain size microstructure.

4.3. Microstructure development of preprocessed Bi-Sb alloys

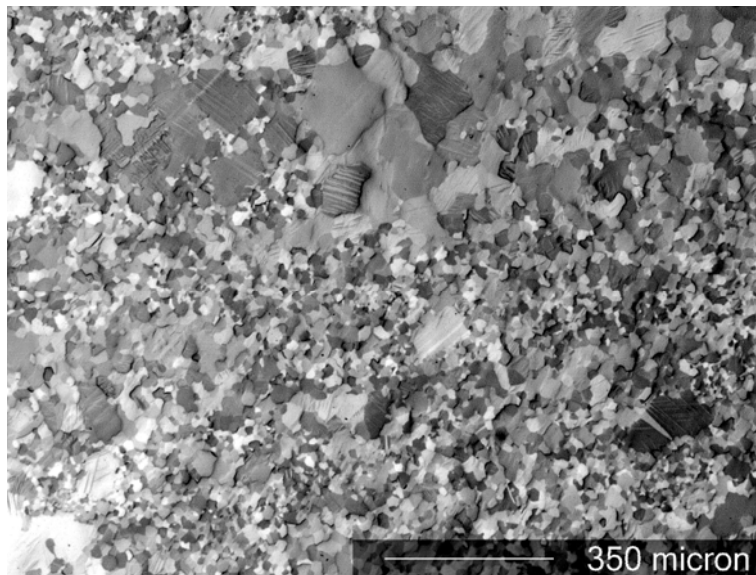
4 3.1. Microstructure of preprocessed Bi-Sb alloys

According to preliminary experiments, the cast grains of Bi-Sb alloy are refined through dynamic recrystallization during hot plastic deformation. The cast Bi-Sb alloy grains are not fully refined and produce a bimodal grain sized microstructure (approximately 10 μm size of fine grains and up to 300 μm size of coarse grains). Even after four extrusion passes of route A or route C, ECAE processing at an elevated temperature does not produce a homogeneous fine grain structure from the cast Bi-Sb alloy.

According to the literature review, route B_C is the best route for grain refinement because of the number of intersecting shear planes. Thus, the experiment conducted with different extrusion rates (0.1, 0.3, and 0.6 in/min) and extrusion temperatures (220, 230, and 250°C) utilized route B_C. The overall extrusion conditions examined for



(i) Two extrusion passes



(ii) Four pass extrusion

Figure 22. Microstructure development of Bi-Sb alloy after (i) two extrusion passes and (ii) four extrusion passes via route A at an extrusion temperature of 250°C and an extrusion rate of 0.1in/min.

maximum grain refinement via the ECAE process are listed in Tables 3 and 4 in the previous section.

The microstructure development after four extrusion passes via route B_C with different extrusion rates is shown in Figure 23. All microstructures show two different areas: one is called a fine-grain area (5-30 μm) and the other area is called a coarse-grain area (50~300 μm). The average fine grain size for an extrusion rate 0.1 in/min is approximately 15 μm . At 0.3 in/min, the average grain size is around 11 μm . At 0.6 in/min, the average grain size is around 9 μm . The average fine-grain size decreases as the extrusion rate increases. The percentage of fine-grain area at an extrusion rate of 0.1 in/min is approximately 55%. At 0.3 in/min, it is 59%. At 0.6 in/min, it is 56%. Similar percentages of fine-grain area occur for the different extrusion rates. The level of grain refinement for cast Bi-Sb alloy is not strongly dependent on extrusion rate.

Figure 24 shows the effect on extrusion temperature (200 and 235 $^{\circ}\text{C}$) on microstructure development. The other extrusion conditions are fixed: extrusion rate 0.3 in/min, four extrusion passes, and route B_C. The average fine-grain size at an extrusion temperature of 220 $^{\circ}\text{C}$ is about 7 μm ; it is 9 μm at 235 $^{\circ}\text{C}$. The results from the experiment also show a bimodal grain sized microstructure. The percentage of fine-grain area at the extrusion temperature of 220 $^{\circ}\text{C}$ is 48% while it is 56% for 235 $^{\circ}\text{C}$. The percentage of fine-grain area increases as the extrusion temperature increases, but a large portion of coarse grain still exist. At three temperatures, the level of grain refinement for cast Bi-Sb alloy is not affected significantly by the extrusion temperature.

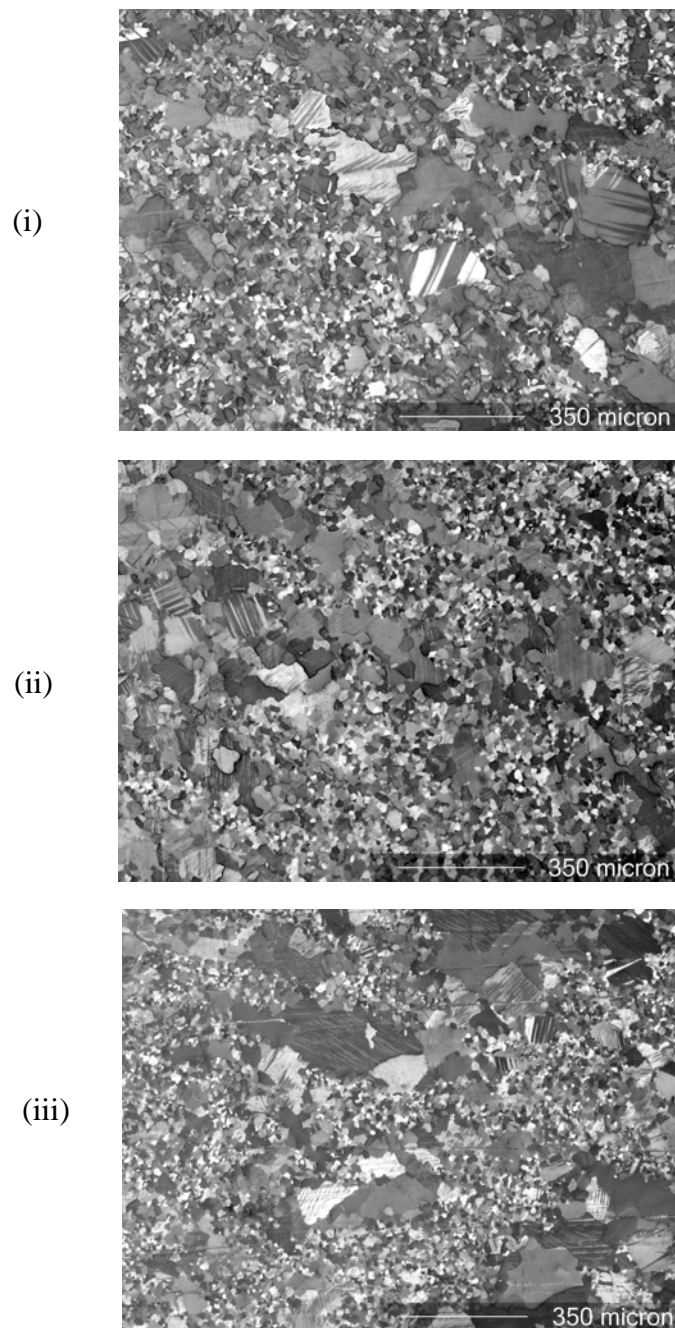


Figure 23. Microstructure development of Bi-Sb alloy after four extrusion passes via route B_C with different punch speeds: (i) 0.1, (ii) 0.3, and (iii) 0.6 in/min at extrusion temperature 250°C.

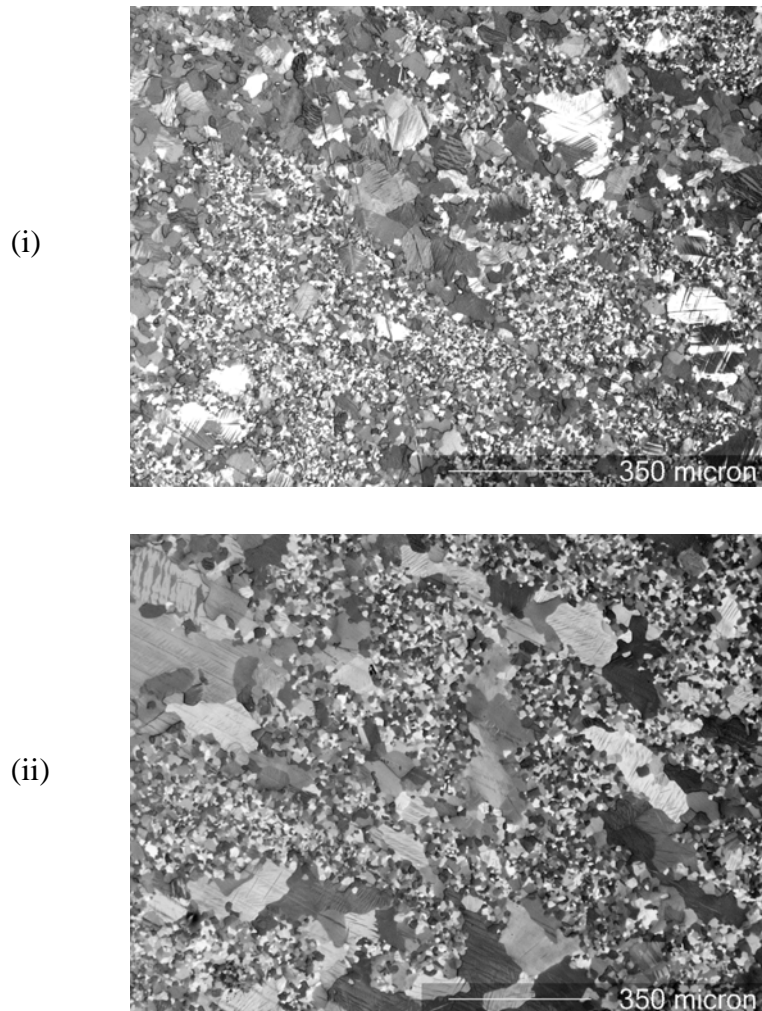


Figure 24. Microstructure of $\text{Bi}_{90}\text{Sb}_{10}$ alloy after four extrusion passes with a punch speed of 0.3 in/min via route Bc of different extrusion temperatures: (i) 220 and (ii) 235°C.

The grain refinement effect on the hydrostatic pressure is studied using encapsulation of a cast Bi-Sb alloy in a copper can. The average maximum punch pressure for extrusion an aluminum composite can was approximately 310 MPa and for a copper composite can was approximately 670 MPa. The extrusion experiment was carried out

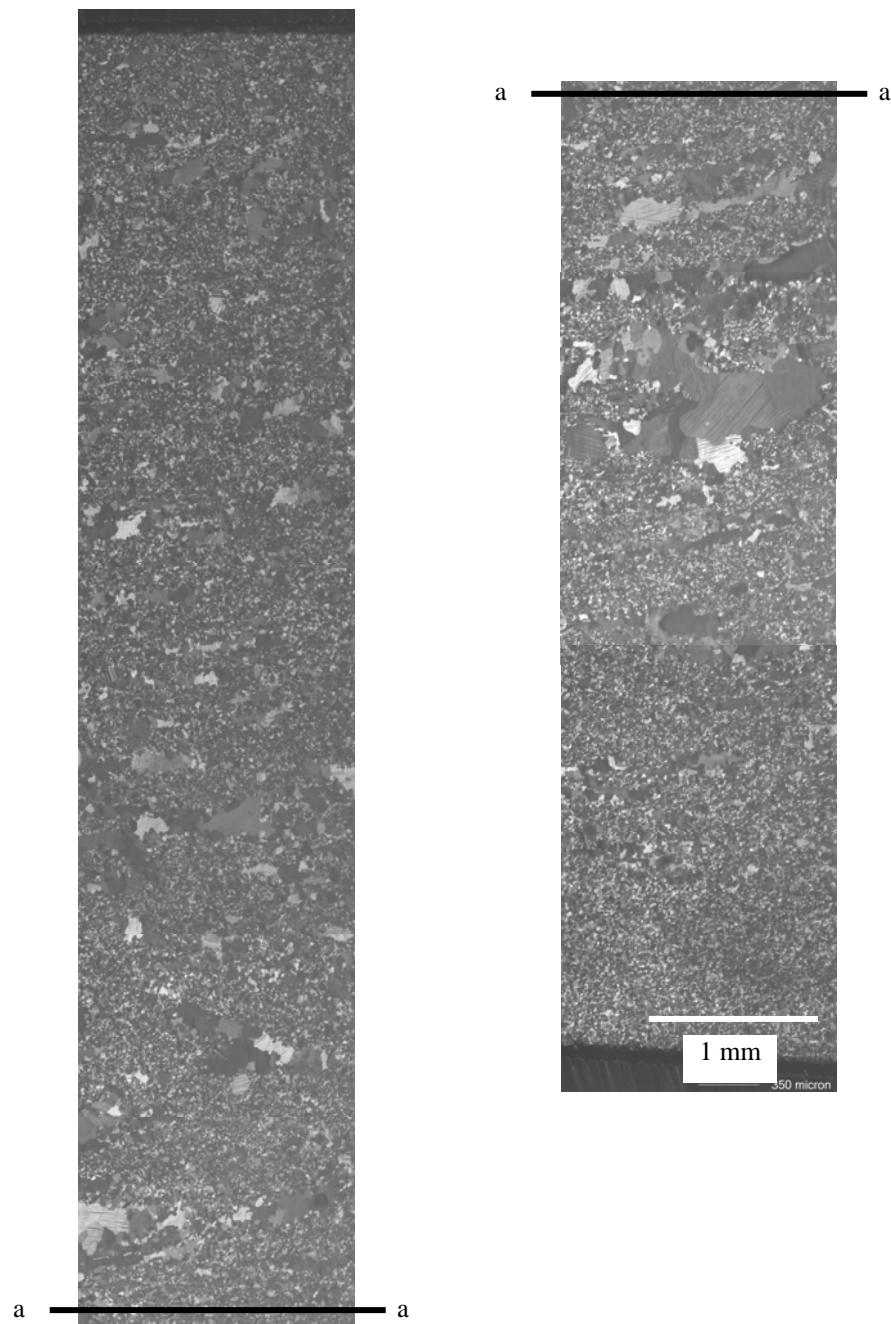


Figure 25. Microstructure development of Bi-Sb alloy encapsulated in a Cu can after four extrusion passes via route Bc at an extrusion temperature of 235°C and at a punch speed of 0.3 in/min.

following four extrusion passes via route B_C at a temperature of 235°C and a punch speed 0.3 in/min. Figure 25 shows the microstructure development with an increased hydrostatic force during hot extrusion. The average grain size in the fine-grain area is approximately 10µm and the percentage of fine grain area is 65%. These results are compared to the results with an aluminum composite can carried out under the same extrusion conditions (four extrusion passes via route B_C at an extrusion temperature 235°C and punch speed 0.3in/min). The average grain size in fine-grain area under these circumstances is similar (10-11µm) but the percentage of fine grain area increases approximately 10%. Even though there is an increased hydrostatic force during plastic deformation, the average grain size is not affected appreciably.

4.3.2. Texture of preprocessed Bi-Sb alloys

Figure 26 shows the {0 0 6} pole figures of preprocessed material at extrusion rates of (i) 0.1, (ii) 0.3 (iii) 0.6 in/min via route B_C at 250°C. The strong texture of cast Bi-Sb alloy disappears and a relatively weak texture develops as a result of preprocessing. The basal poles are observed to orient from 5-40° on the longitudinal plane normal regardless of extrusion rate. The temperature effect shows a similar pattern in Figure 27. The basal poles are observed at 5-25° on the longitudinal plane normal regardless of extrusion temperatures. In this case a weak texture also is formed.

4.4. Microstructure from further deformation of preprocessed Bi-Sb alloys

4. 4. 1. Grain refinement with further deformation

Figure 28 to 34 show microstructure development for cases of further plastic deformation of preprocessed Bi-Sb alloy (preprocessed conditions: four extrusion

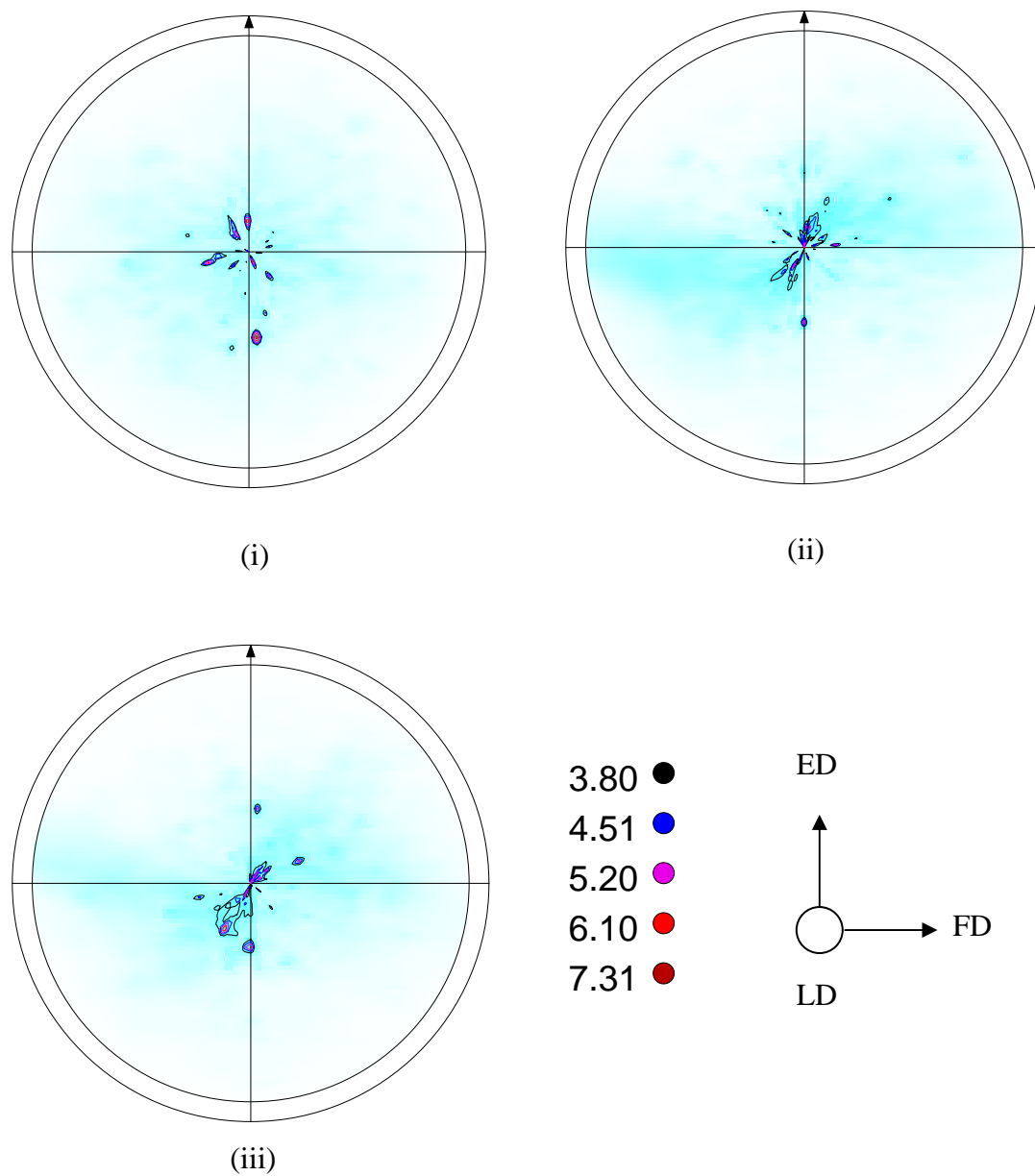


Figure 26. The $\{0\ 0\ 6\}$ pole figures of preprocessed material under extrusion rates: (i) 0.1, (ii) 0.3 (iii) 0.6 in/min via route B_C at 250°C (ED: Extrusion direction, (LD: Longitudinal plane normal direction, FD: Flow plane normal direction).

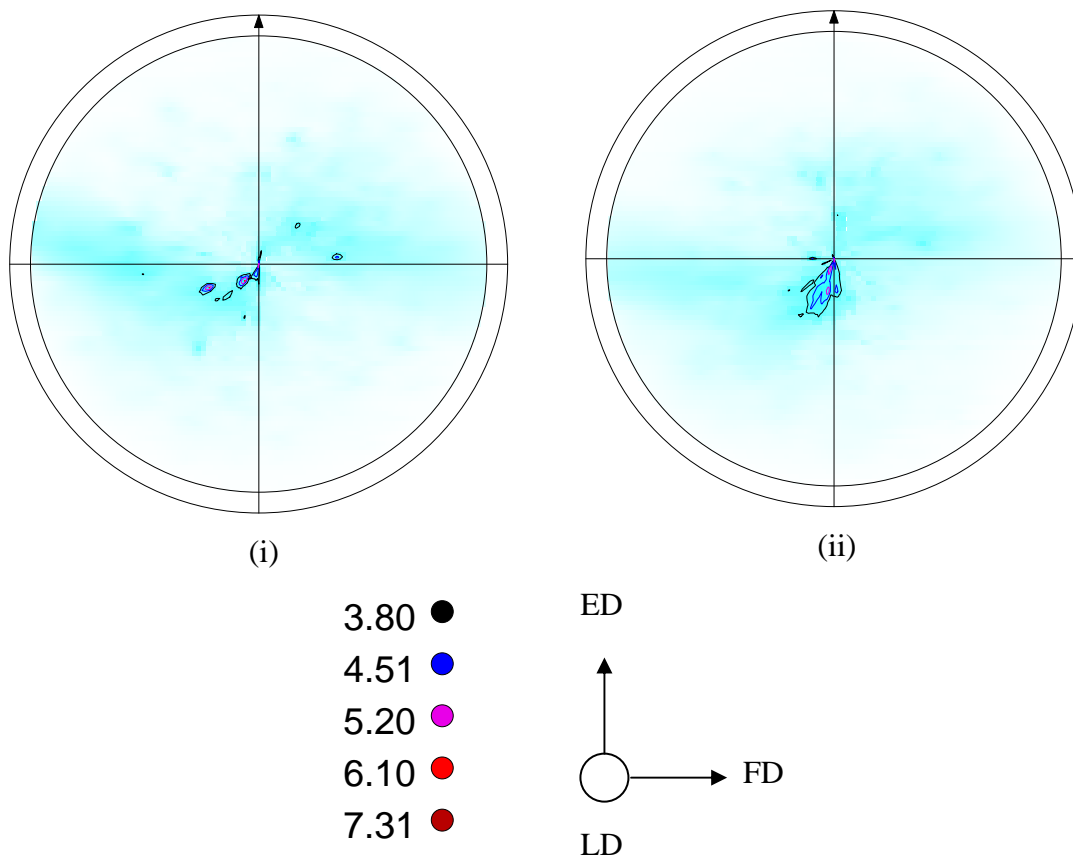


Figure 27. The $\{0\ 0\ 6\}$ pole figures of preprocessed material under extrusion temperatures: (i) 235°C (ii) 220°C via route B_C at 0.3in/min. (ED: Extrusion direction, (LD: Longitudinal plane normal direction, FD: Flow plane normal direction).

passes via route B_C at an extrusion temperature of 235°C and a punch speed 0.3 in/min with ECAE). The extrusion conditions for further plastic deformation include an

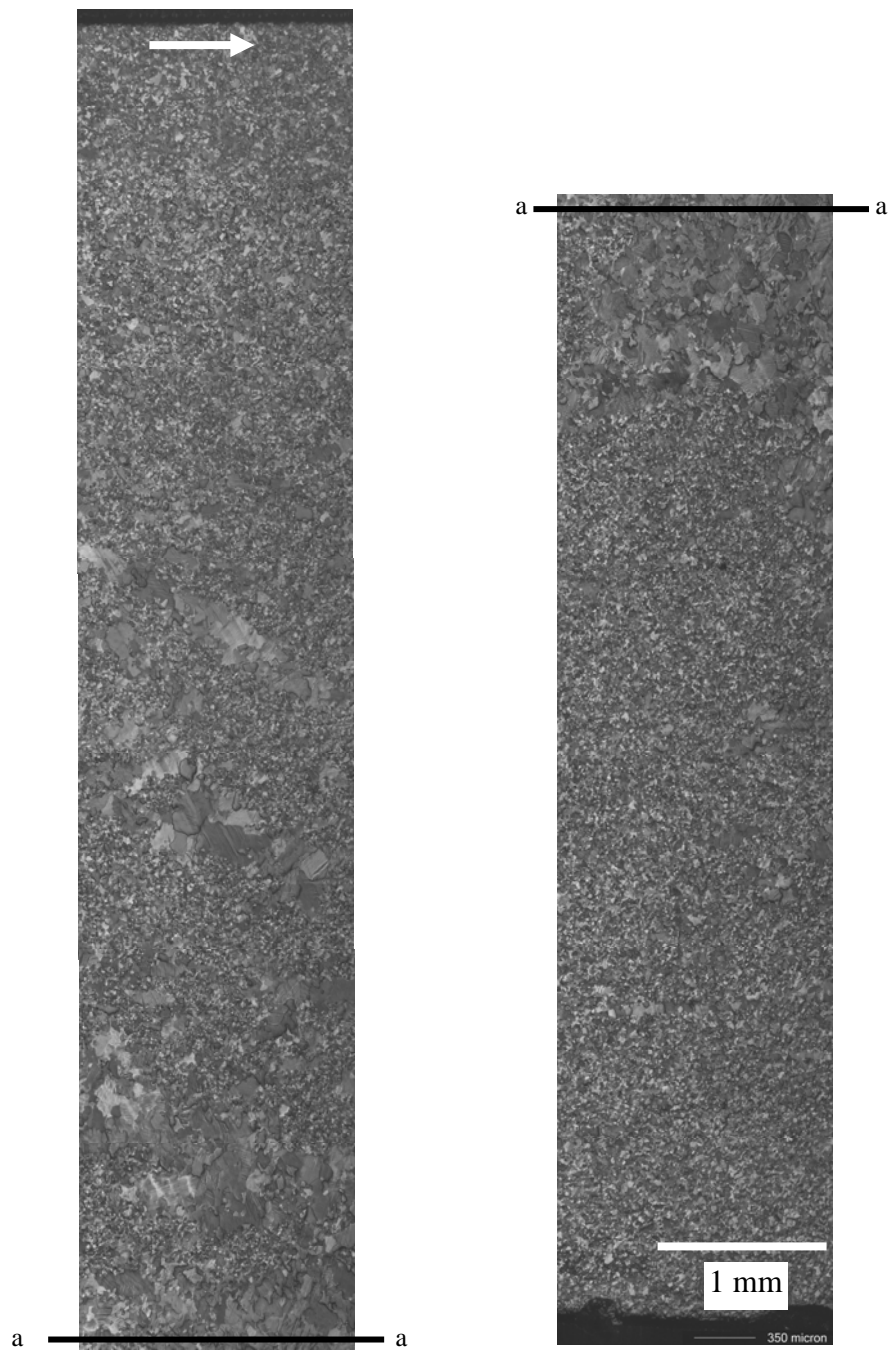


Figure 28. Microstructure development of preprocessed Bi₉₀Sb₁₀ alloy after one extrusion pass at an extrusion temperature of 235°C and a punch speed of 0.3 in/min. (Preprocessed conditions: extrusion temperature 235°C; punch speed 0.3 in/min; ECAE route B_C).

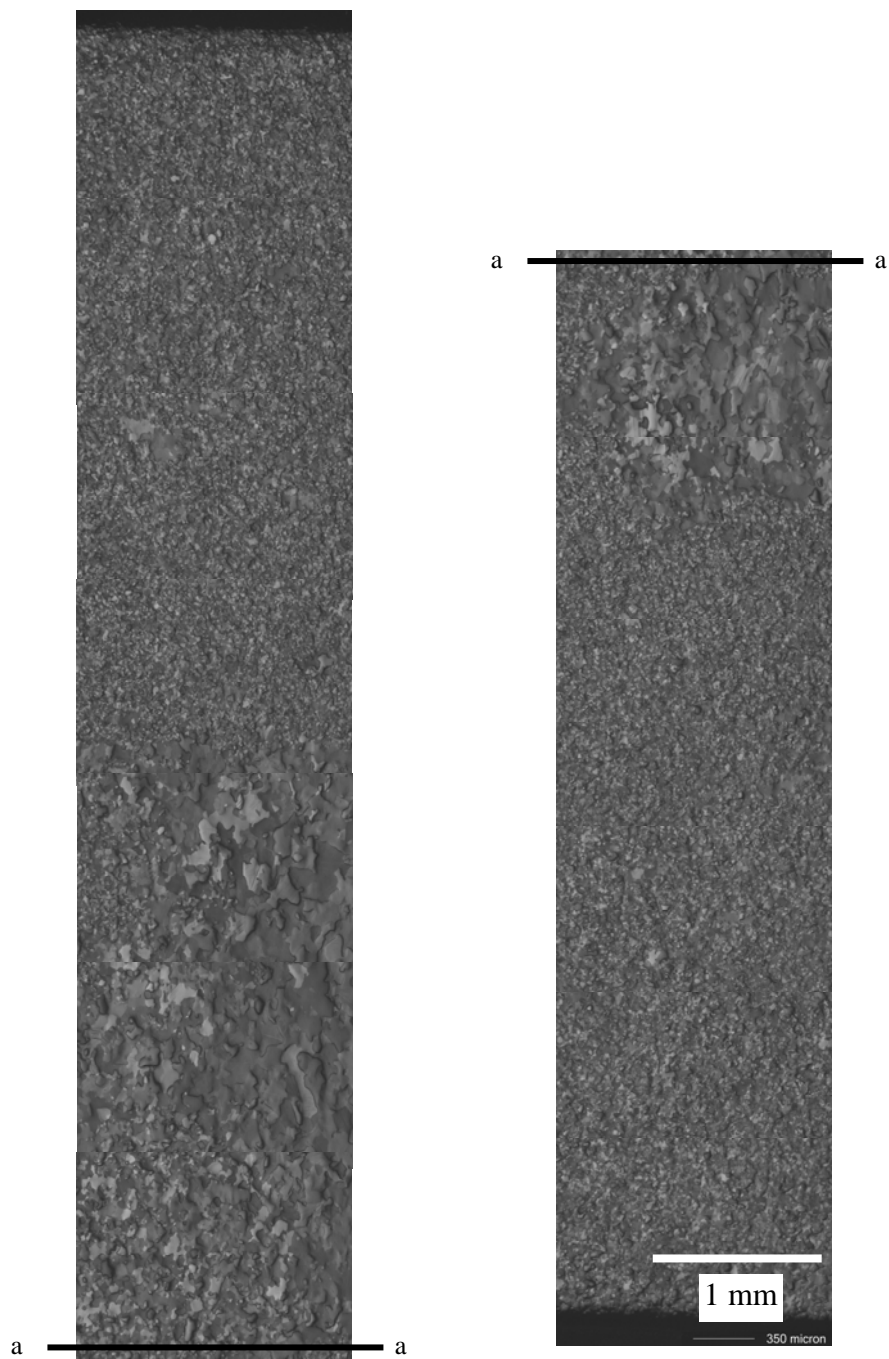


Figure 29. Microstructure development of preprocessed $\text{Bi}_{90}\text{Sb}_{10}$ alloy after two extrusion passes via route A at an extrusion temperature of 235°C and a punch speed of 0.3 in/min.

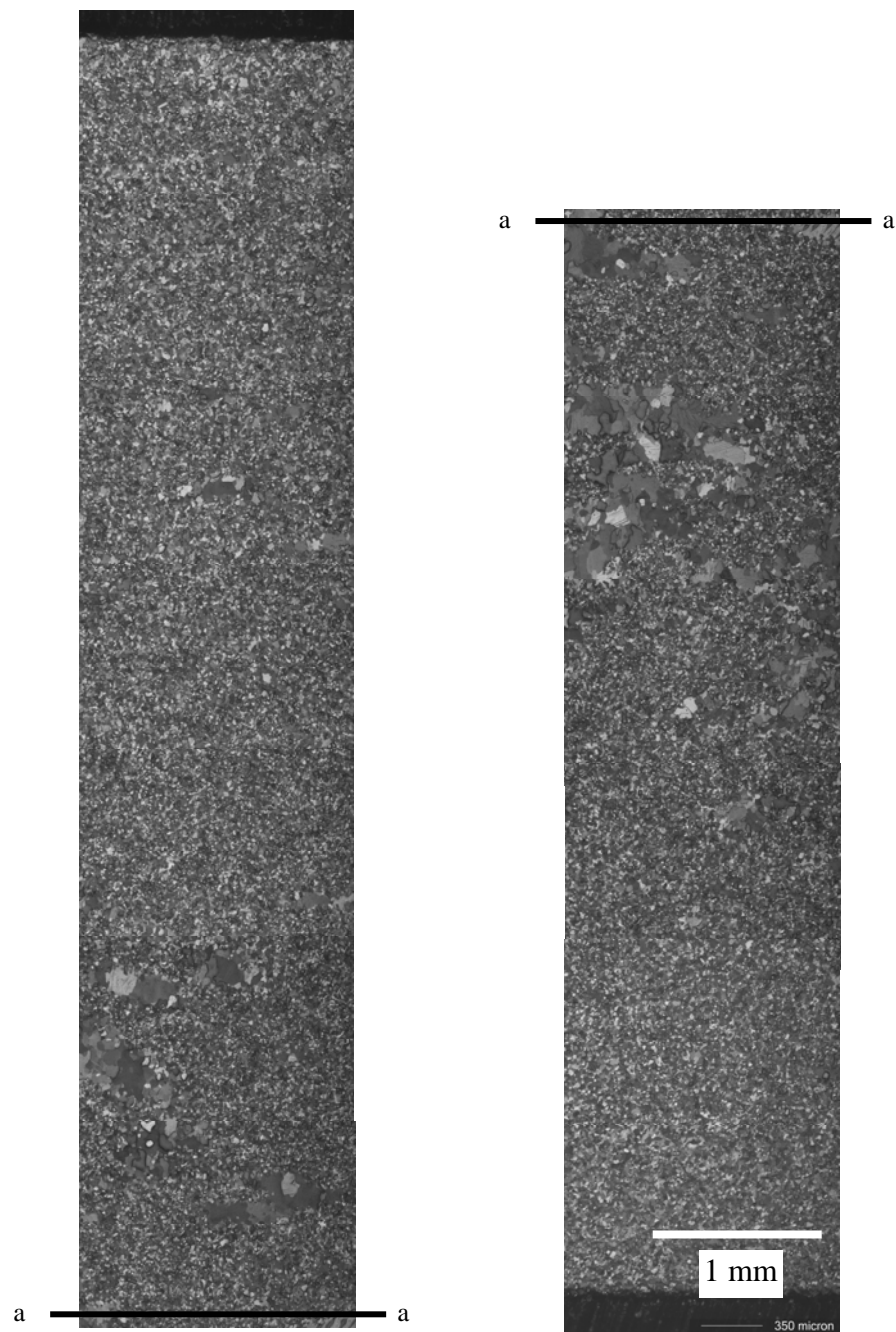


Figure 30. Microstructure development of preprocessed $\text{Bi}_{90}\text{Sb}_{10}$ alloy after four extrusion passes via route A at an extrusion temperature of 235°C and a punch speed of 0.3 in/min.

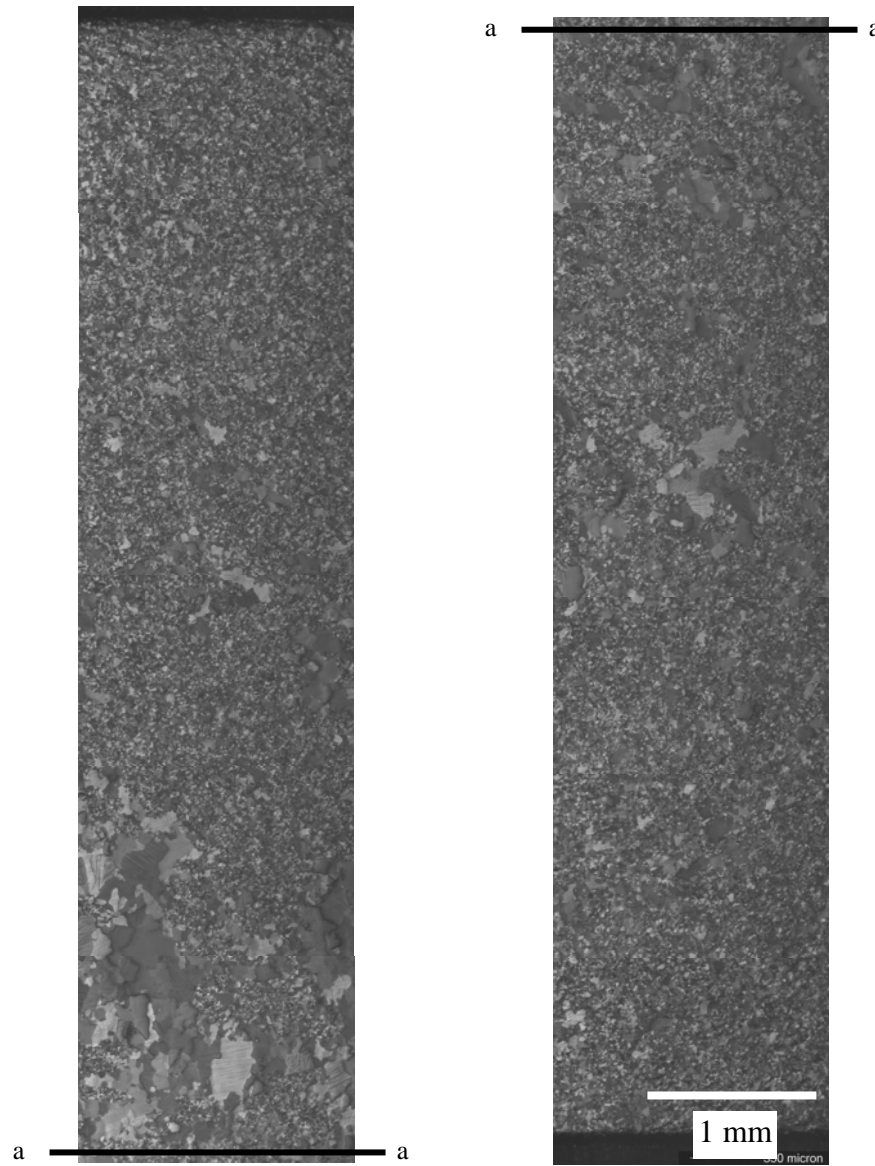


Figure 31. Microstructure development of preprocessed $\text{Bi}_{90}\text{Sb}_{10}$ alloy after two extrusion passes via route C at an extrusion temperature of 235°C and a punch speed of 0.3 in/min.

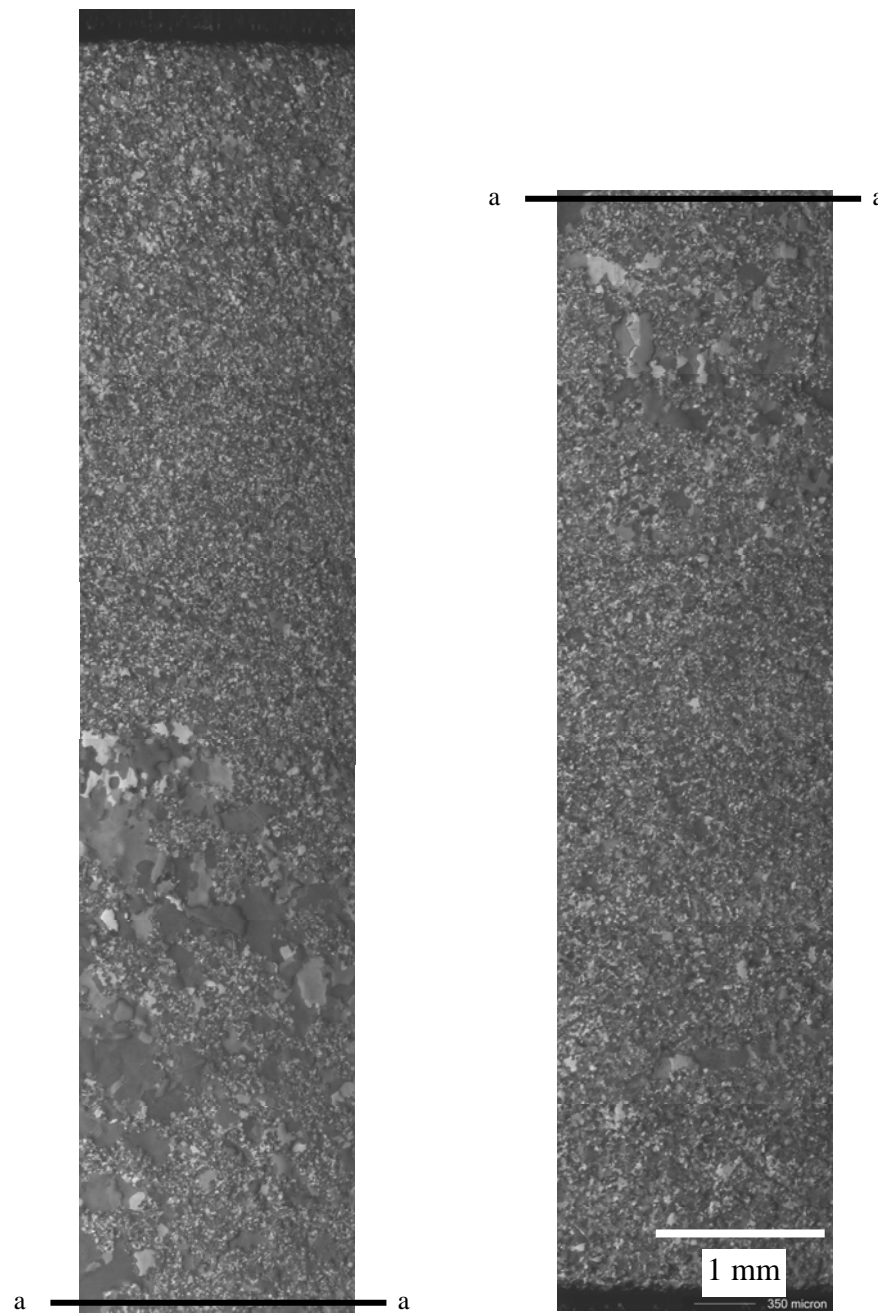


Figure 32. Microstructure development of preprocessed Bi₉₀Sb₁₀ alloy after four extrusion passes via route C at an extrusion temperature of 235°C and a punch speed of 0.3 in/min.

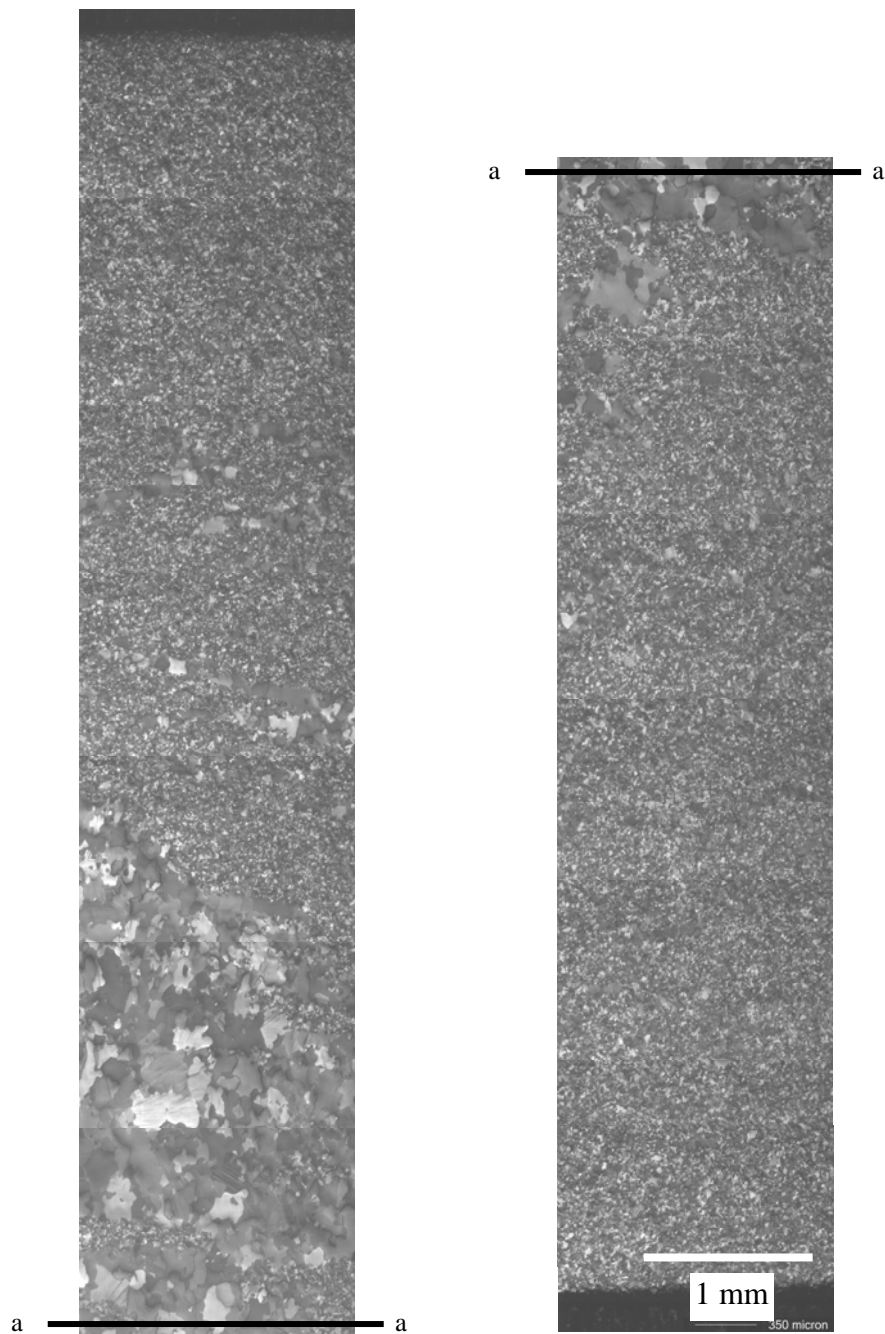


Figure 33. Microstructure development of preprocessed $\text{Bi}_{90}\text{Sb}_{10}$ alloy after using half exit area extrusion at an extrusion temperature of 235°C and a punch speed of 0.15 in/min.

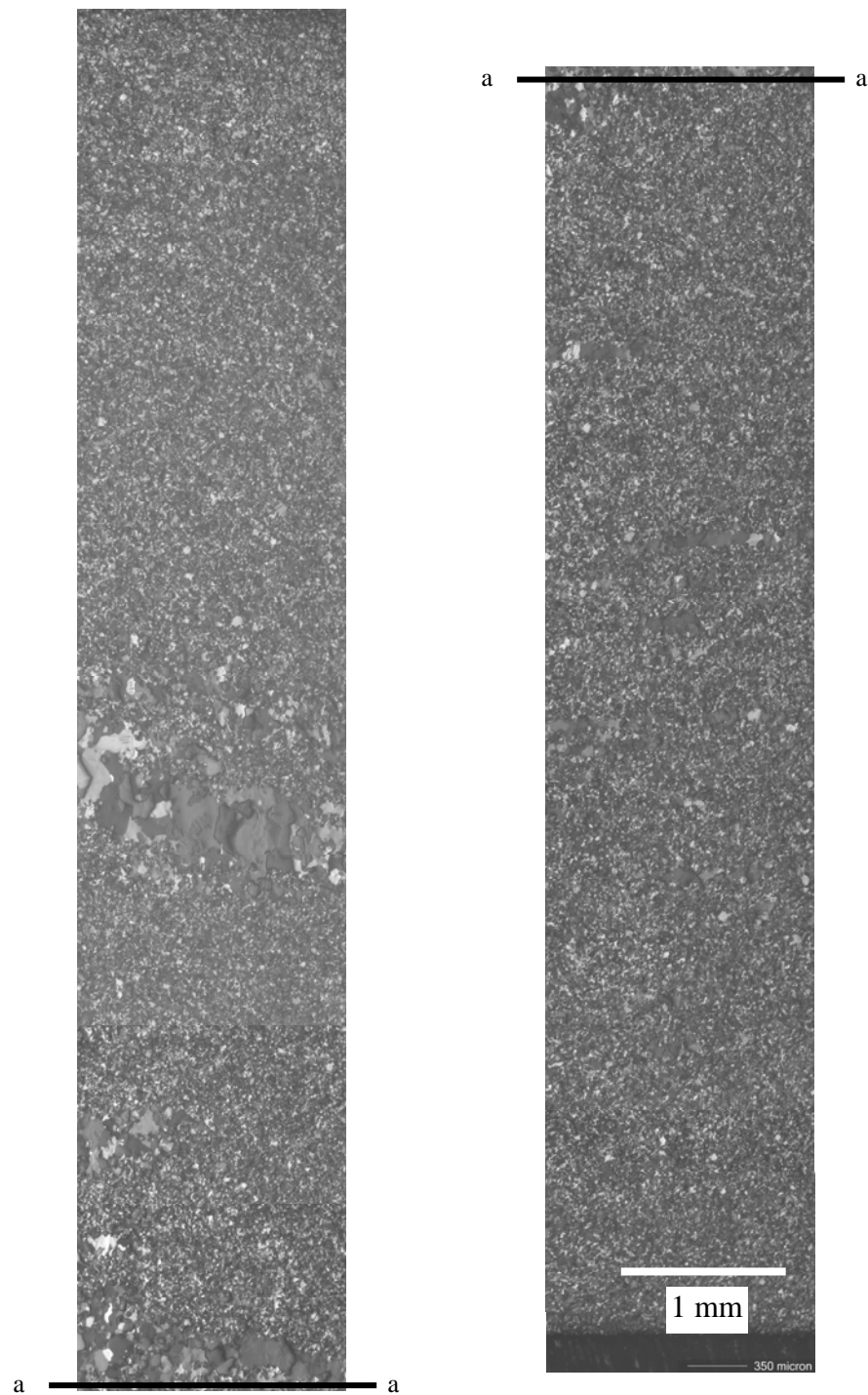


Figure 34. Microstructure development of preprocessed $\text{Bi}_{90}\text{Sb}_{10}$ alloy after using quarter exit area extrusion at an extrusion temperature of 235°C and a punch speed of 0.15 in/min.

increased number of extrusion passes (one, two and four), different route (A and C), and area reduction in the exit channel. The average fine-grain size of one, two, and four extrusion passes via route A is 9-10 μm . The average fine-grain size remains similar to preprocessed samples regardless of the number of extrusion passes. Coarse grains (50-300 μm) remain in the microstructure, and a bimodal microstructure persists as shown in Figure 28 to 30. The percentages of fine grain area are 64%, 72%, and 89%. The percentage of fine grain area gradually increases as the number of extrusion passes increases.

Similar grain morphology exists for two and four extrusion passes via route C. The bimodal microstructures are shown in Figure 31 and 32. Average grain size is 10-11 μm for two and four extrusion passes via route C and the percentages of grain refinement are 73% and 82%. Though the percentage of fine grain area gradually increases with the number of extrusion passes via route C, the bimodal microstructure remains regardless of the extrusion route.

The extrusion conditions for reduced exit channel areas ($A_{\text{ex}}=1/2A_{\text{in}}$ and $1/4A_{\text{in}}$) are one extrusion pass and an extrusion temperature of 235 $^{\circ}\text{C}$. The punch speeds are varied at 0.15 in/min and 0.075 in/min for half and quarter area exit channel extrusion in order to maintain the extrusion rate (0.3 in/min) in the exit channel. The microstructures of reduced exit channel area material, with preprocessed billets, are shown in Figure 33 and 34. Average grain size is approximately 10 μm for both extrusions. Coarse-grain area (50-250 μm) persists and percentages of fine-grain area are 75% and 86% for the half and quarter exit channel area, respectively. As the exit

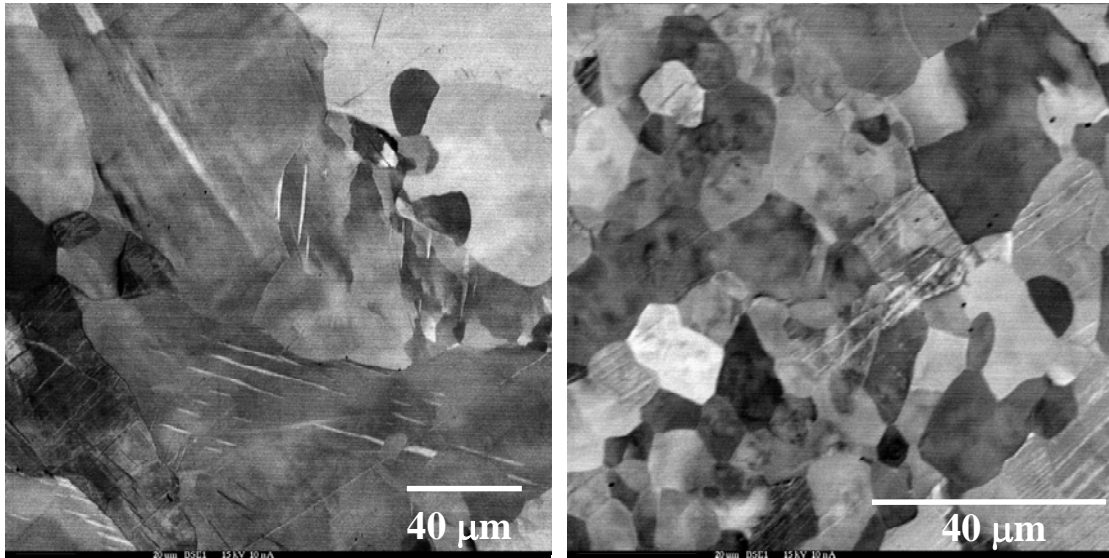
channel area decreases the grain refinement is more efficient. However, the bimodal grain size microstructure does not disappear. The reduced exit area channel extrusions are more effective for grain refinement compared to that of one pass ECAE, but reduced cross section area extrusion still has difficulties for grain refinement (i.e. the bimodal microstructure persists).

4.4.2. Microprobe analysis for chemical homogeneity

EDS and WDS were performed in order to check the chemical homogeneity in the material for one extrusion pass via ECAE and half exit area extrusion case. The quantitative EDS results for the sample processed via ECAE are shown in Figure 35. From the qualitative analysis, it is seen that the antimony peaks near 3.6 KeV are different for the coarse-grain area and fine-grain areas. The antimony peak in fine-grain area is higher than in the coarse grain area. This indicates more antimony in it.

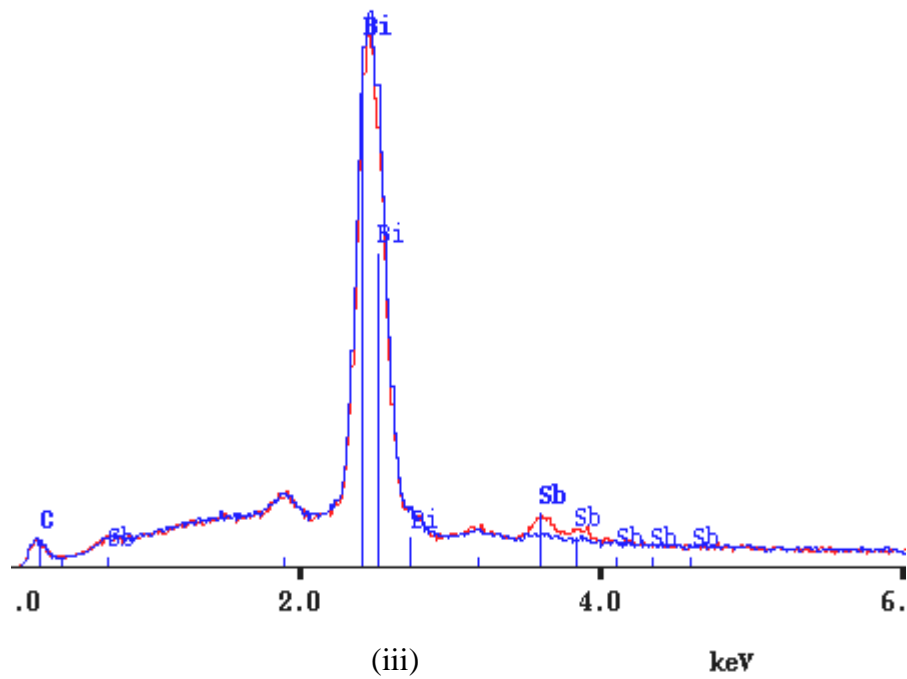
Further quantitative analysis conducted with WDS is shown in Figure 36. The antimony content in coarse-grain area and fine-grain area are 0.5-4.9 at% and 6.5-15.8 at% respectively. The level of grayness in the EDS images does not represent the level of antimony contents. The antimony content in coarse grains is much lower than that in fine grains. It is clear that the antimony content varies between areas of different grain size and the sample has inhomogeneous chemical composition even after multipass ECAE processing.

The EDS and WDS results for the sample processed via half exit area extrusion are shown in Figure 37 and 38. From the qualitative analysis, the antimony peak in the sample is slightly higher in the coarse grain area than that of fine grain area as shown



(i)

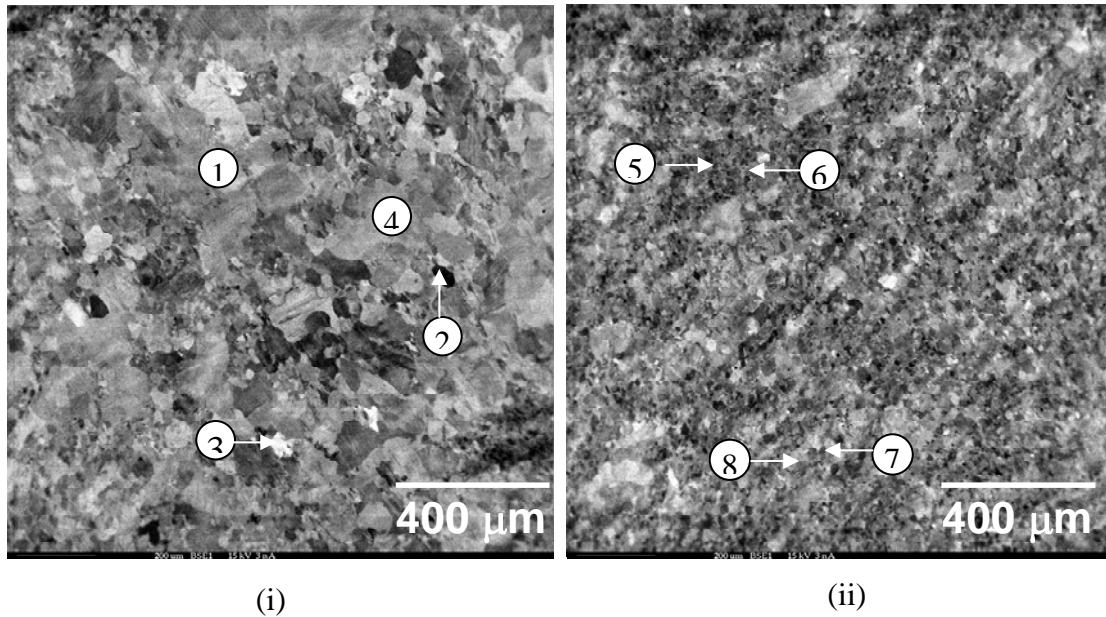
(ii)



(iii)

keV

Figure 35. Microprobe analysis with EDS for one extrusion pass of preprocessed $\text{Bi}_{90}\text{Sb}_{10}$ alloy via ECAE: (i) coarse grain area, (ii) fine grain area, and (iii) qualitative analysis.



Area	Location	Bi (at%)	Sb (at%)
Coarse grain	1	97.4	2.6
	2	95.1	4.9
	3	97.5	2.5
	4	99.6	0.5
	Average	97.4	2.6
Fine grain	5	84.2	15.8
	6	93.5	6.5
	7	90.2	9.8
	8	87.4	12.6
	Average	88.7	11.2

(iii)

Figure 36. Microprobe analysis with WDS for one extrusion pass of preprocessed $\text{Bi}_{90}\text{Sb}_{10}$ alloy via ECAE: (i) examined locations in coarse grain area, (ii) in fine grain area, and (iii) quantitative analysis results.

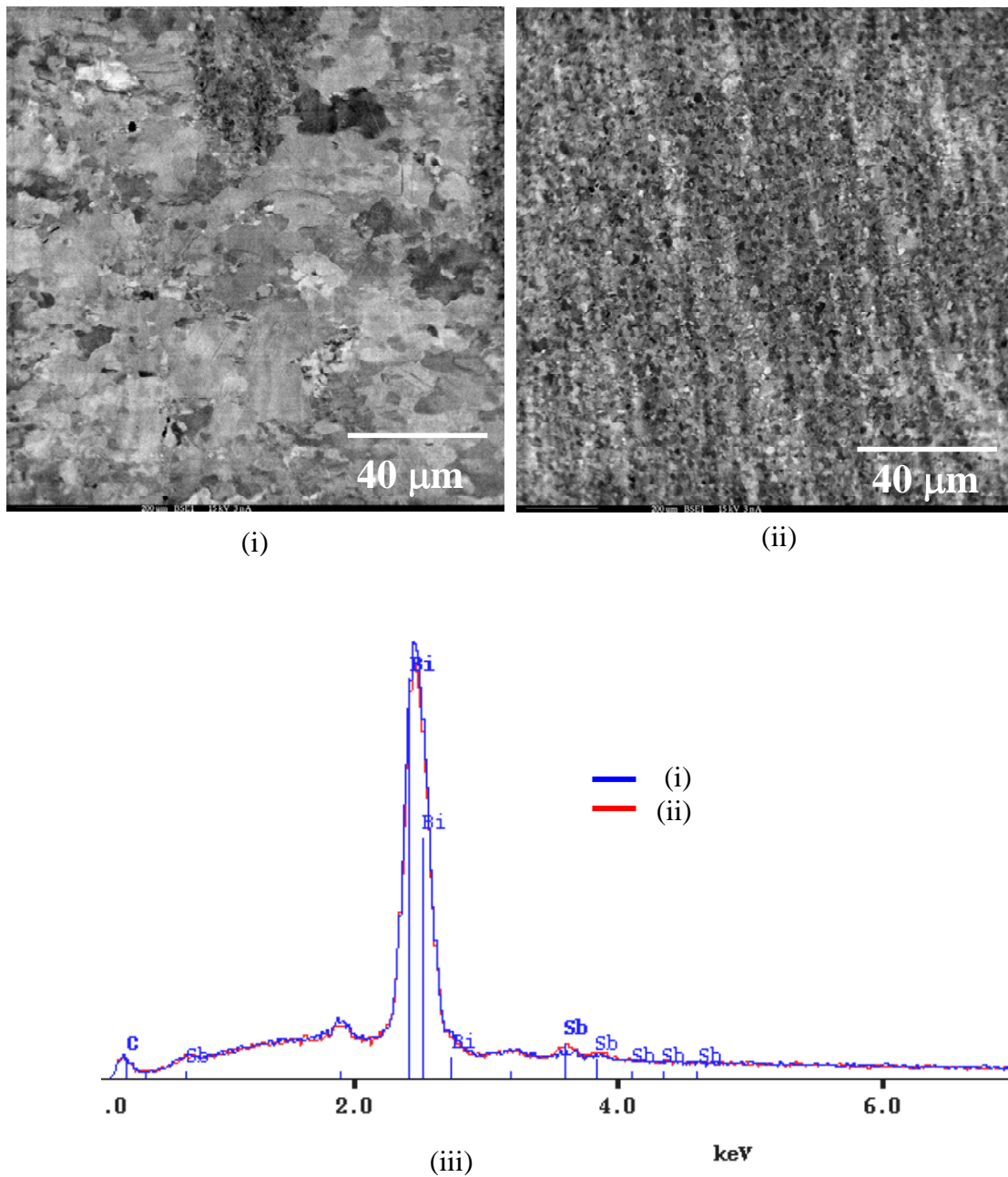
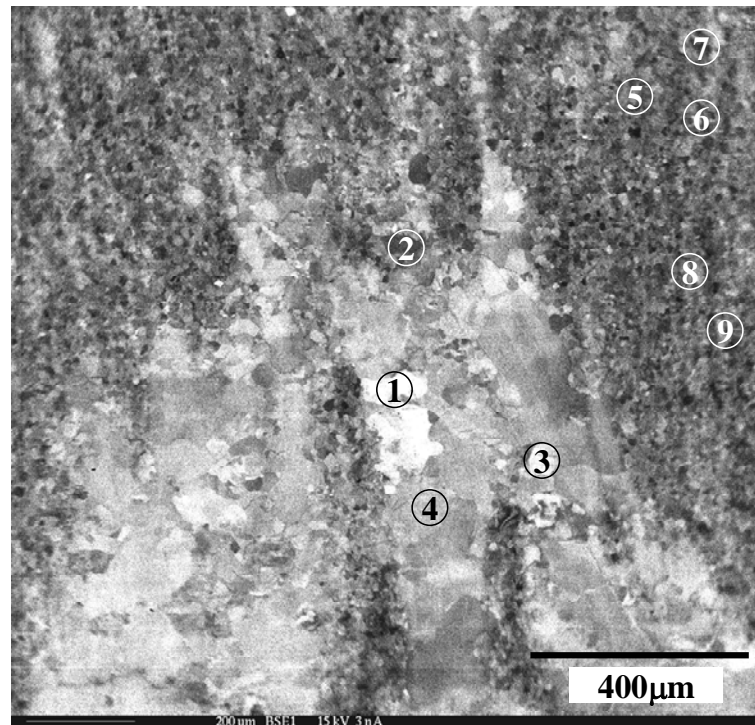


Figure 37. Microprobe analysis with EDS for one extrusion pass of preprocessed $\text{Bi}_{90}\text{Sb}_{10}$ alloy via half exit area extrusion: (i) coarse grain area, (ii) fine grain area, and (iii) qualitative analysis.



(i)

Area	Location	Bi (at%)	Sb (at%)
Coarse grain	1	98.5	1.5
	2	94.3	5.7
	3	97.5	2.6
	4	98.2	1.8
	Average	97.1	2.9
Fine grain	5	80.5	19.6
	6	88.3	11.8
	7	80.3	19.78
	8	97.5	2.58
	9	88.7	11.3
	Average	87.0	13.0

(ii)

Figure 38. Microprobe analysis with WDS for one extrusion pass of preprocessed $\text{Bi}_{90}\text{Sb}_{10}$ alloy via half exit area extrusion: (i) examined locations in EBS image and (ii) quantitative analysis results.

in Figure 37 (iii). This indicates that the antimony content in the fine-grain area is higher than that in the coarse-grain area. Further quantitative analysis conducted with WDS is shown in Figure 38. The antimony content in coarse grains and fine grains is 1.5-5.7 at% and 2.5-19.7 at% respectively. The antimony content in coarse grains is seen to be much lower than that in fine grains. The antimony content of the sample varies among grains and shows inhomogeneous chemical composition after exit channel area reduction extrusion of a preprocessed material.

4.4.3. Texture development with further deformation

Figure 39 shows the $\{0\ 0\ 6\}$ pole figure of processed materials after (i) one pass, (ii) two passes and (iii) four passes via route A. The basal poles are observed at $15\text{-}30^\circ$ on the longitudinal plane normal after one extrusion pass. After a second pass and a fourth pass via route A, the basal poles are observed at $10\text{-}30^\circ$ and $5\text{-}10^\circ$. The basal poles are seen to have a tendency to align toward the longitudinal plane normal, and the strength of texture increases slightly as the number of extrusion pass increases following route A processing.

Figure 40 shows the $\{0\ 0\ 6\}$ pole figures of processed material after (i) two passes and (ii) four passes via route C. The basal poles are observed at $15\text{-}30^\circ$ and $5\text{-}25^\circ$ to the longitudinal plane normal after two and four extrusion passes respectively. The basal poles have tendency to align toward 25° to the longitudinal plane normal, and the strength of texture increased as the number of extrusion pass increases via route C.

Figure 41 shows the $\{0\ 0\ 6\}$ pole figures of processed material following (i) half area and (ii) quarter area exit channel extrusions. The basal poles are observed at

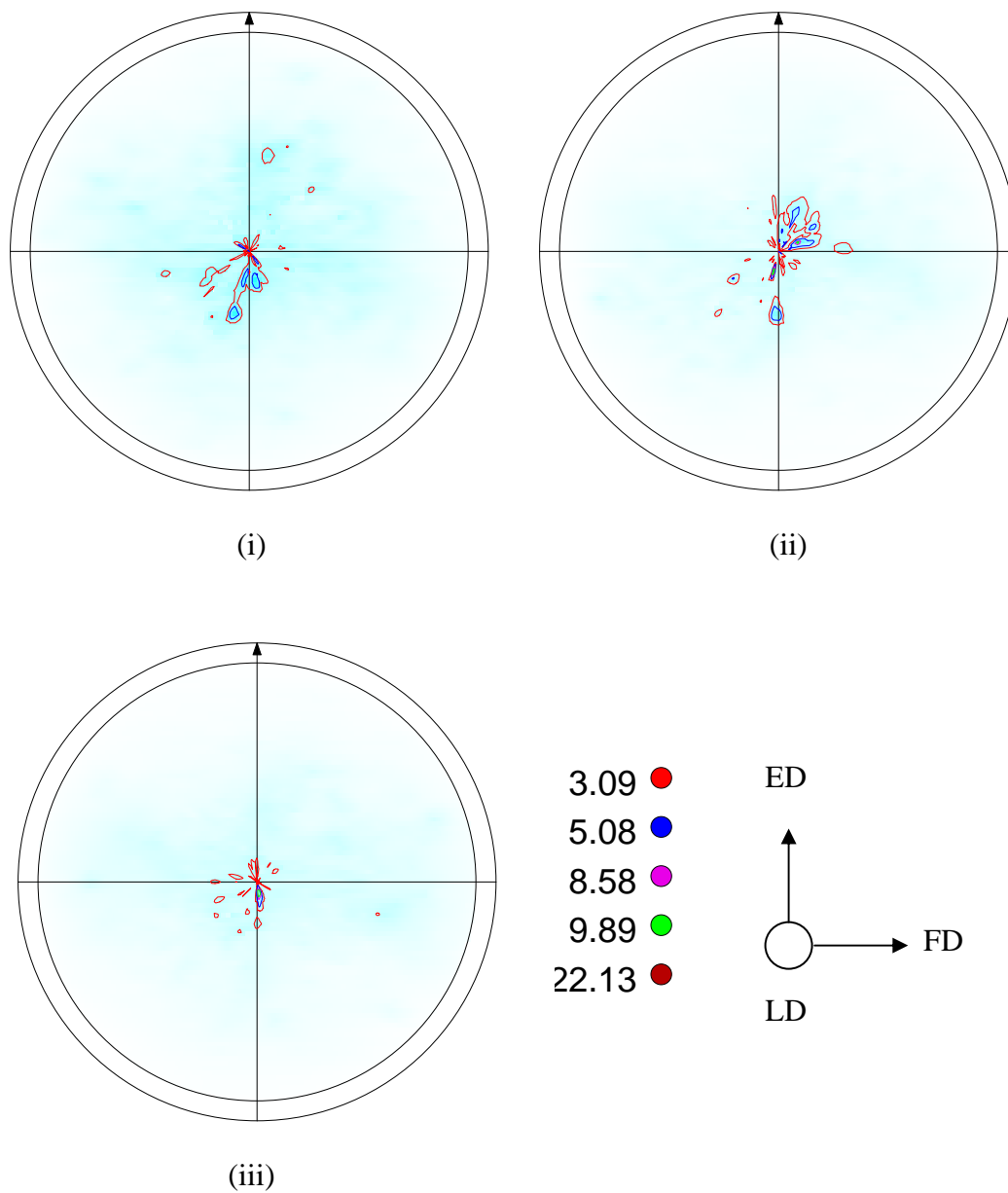


Figure 39. The $\{0\ 0\ 6\}$ pole figures of processed material after: (i) one pass, (ii) two passes and (iii) four passes via route A (ED: Extrusion direction, LD: Longitudinal plane normal direction, FD: Flow plane normal direction).

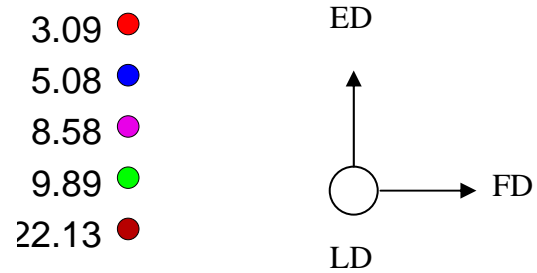
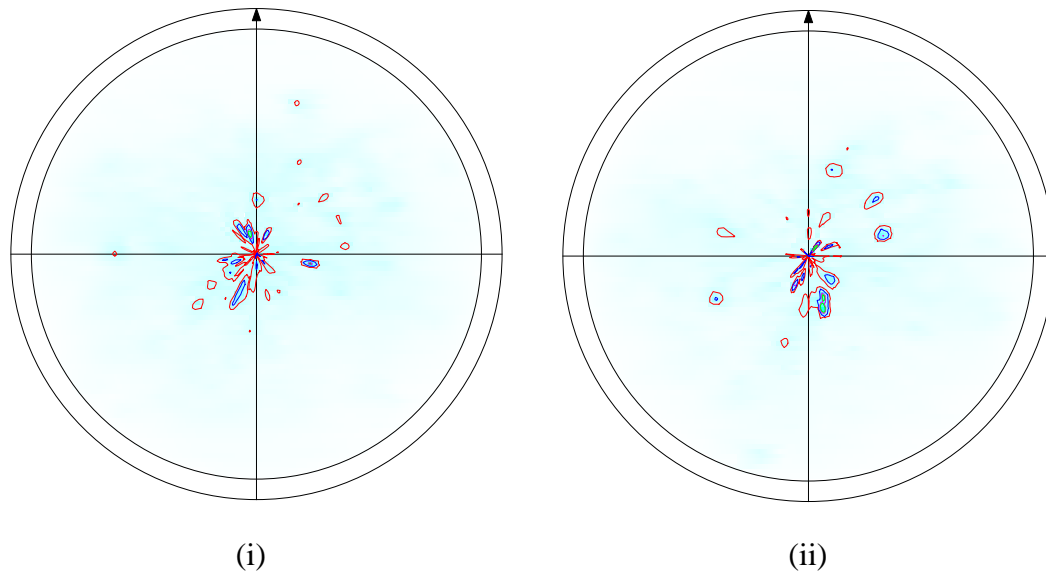


Figure 40. The $\{0\ 0\ 6\}$ pole figures of processed material after: (i) two passes and (ii) four passes via route C (ED: Extrusion direction, LD: Longitudinal plane normal direction, FD: Flow plane normal direction).

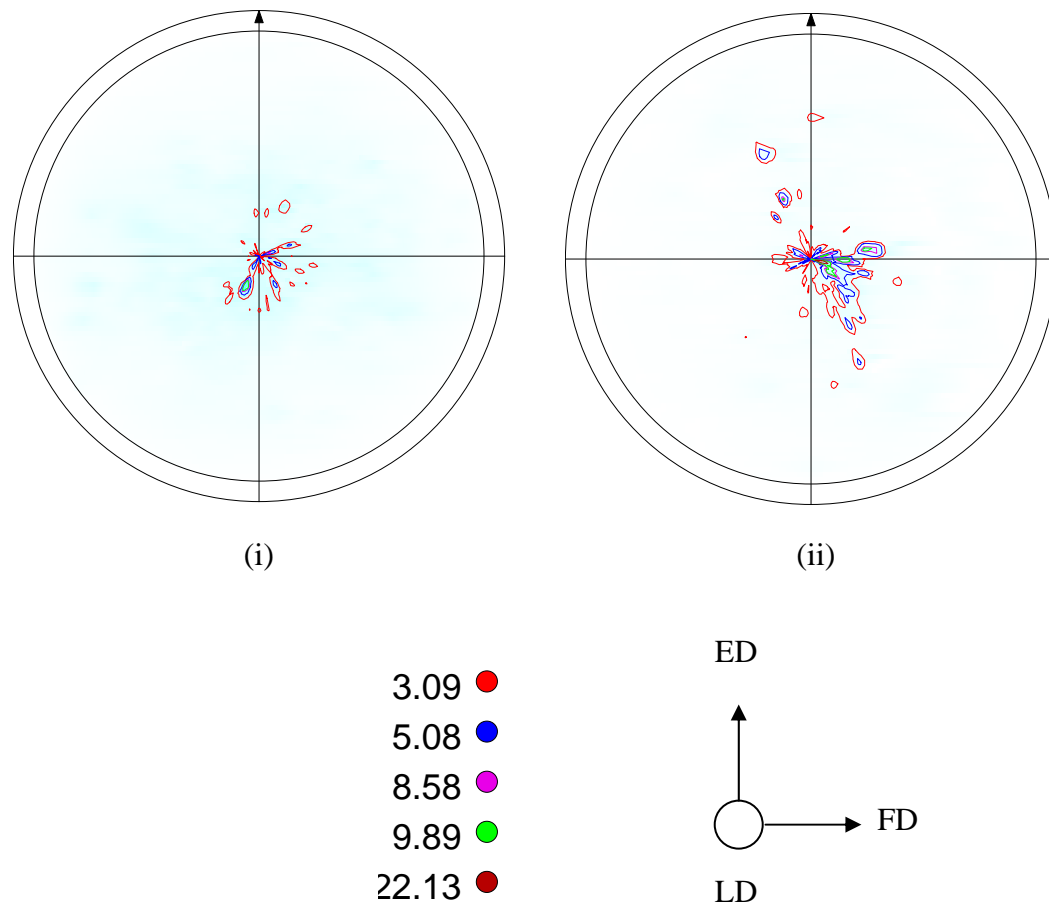


Figure 41. The $\{0\ 0\ 6\}$ pole figures of processed material following: (i) half and (ii) quarter area exit channel extrusion (ED: Extrusion direction, LD: Longitudinal plane normal direction, FD: Flow plane normal direction).

approximately $5-15^\circ$ to the longitudinal plane normal in both cases. The basal poles have a tendency to align toward to the longitudinal plane normal, and the strength of texture greatly increases as the area of the exit channel decreases.

4.5. Microstructure development with further deformation of a preprocessed and heat treated Bi-Sb alloy

4.5.1. Grain refinement with a heat treated Bi-Sb alloy

Figure 42 shows the microstructure after heat treatment of preprocessed Bi-Sb alloy. The preprocessed Bi-Sb alloy was heat treated at 250°C for 100 hours under low vacuum (10^{-3} torr). The grains are seen to have grown to approximately $50-300\mu\text{m}$

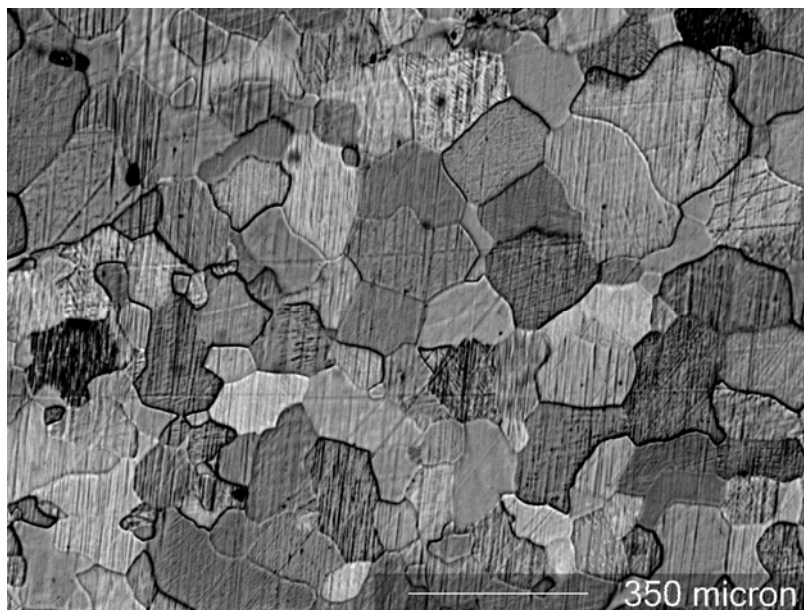


Figure 42. Microstructure of preprocessed and heat treated Bi-Sb alloy. Heat treatment conditions: annealing temperature of 250°C for 100 hours under low vacuum (10^{-3} torr).

during heat treatment, and the microstructure does not show bimodal grain size morphology.

Figure 43 shows the microstructure after four extrusion passes via route B_C of the preprocessed and heat treated Bi-Sb alloy. The extrusion conditions are the same as those for the preprocessing. The microstructure is again bimodal but the percentage of the fine-grain area is dramatically improved (to approximately 95%) over that for the cases without a long term heat treatment prior to deformation processing. The average fine grain size is approximately 10 μ m and the coarse grain size is approximately 50-150 μ m.

4.5.2. Microprobe analysis for chemical homogeneity

EDS and WDS were conducted in order to check the chemical homogeneity of the sample proceed with four extrusion passes via route B_C after preprocessing and long term heat treatment. The EDS results of the quantitative analysis are shown in Figure 44 for coarse grains (approximately 100 μ m) and Figure 45 for fine grains (approximately 10 μ m). The antimony peaks in the coarse grains, regardless of the grayness (bright and dark grains), are similar as shown in Figure 44. The antimony peaks in the fine grains, regardless of the grayness (bright and dark grains), are also similar as shown in Figure 45. Thus, the level of gray does not represent the antimony contents in the sample. However, the antimony peaks in the fine grains are slightly higher than those in coarse grains by comparison of the peaks in Figure 44 and 45.

Further quantitative analysis was performed with WDS and is shown in Table 6. The analyzed grains are indicated in the EBS images of the Figure 44 and 45. The

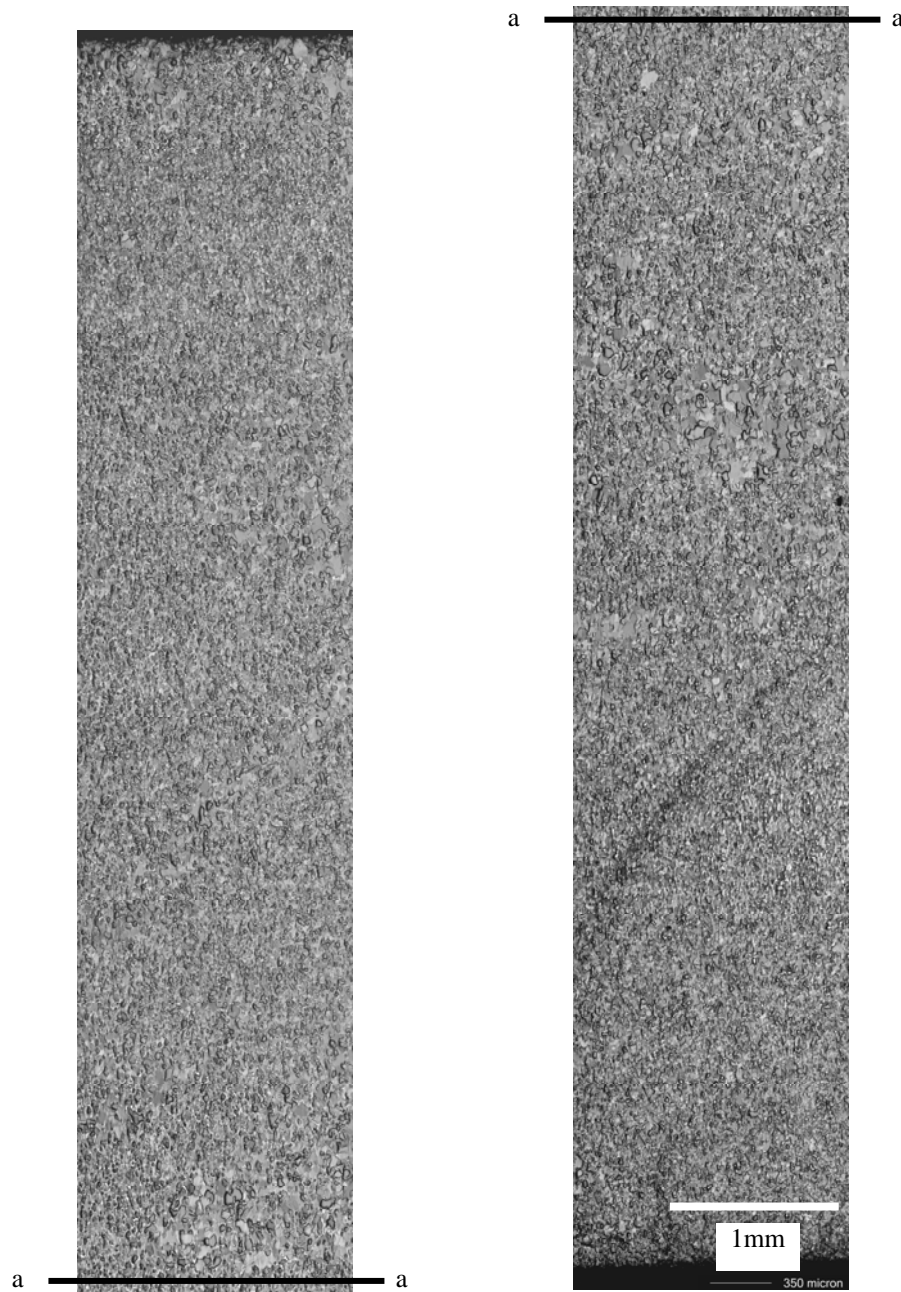


Figure 43. Microstructure after four extrusion passes via route B_C using preprocessed and heat treated Bi₉₀Sb₁₀ alloy.

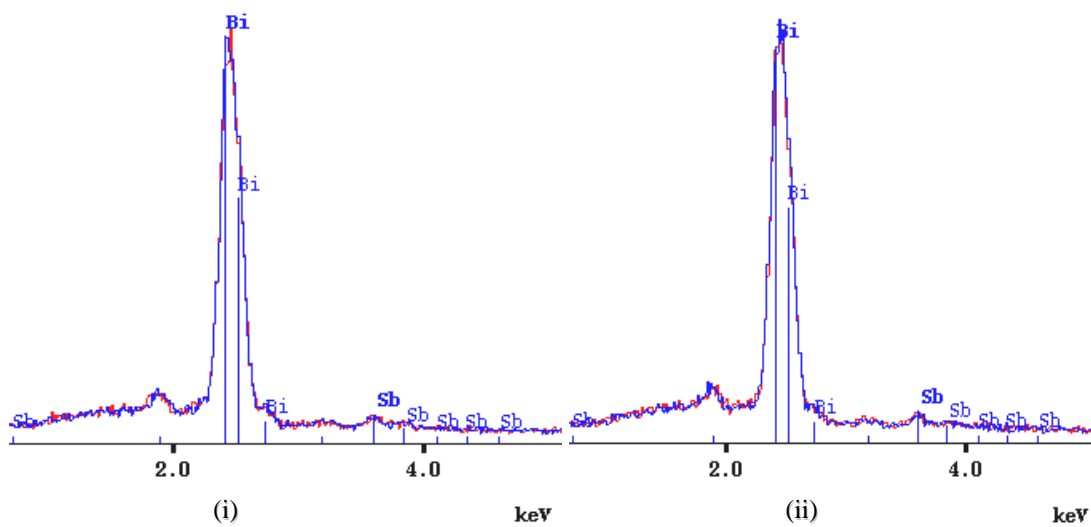
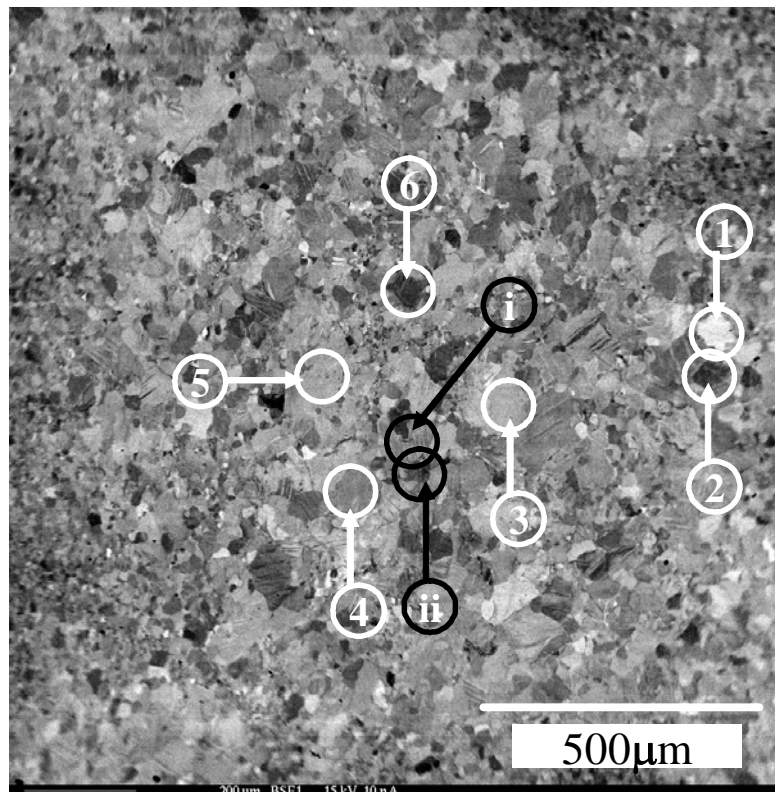


Figure 44. Microprobe analysis with EDS of coarse grains after four extrusion passes of preprocessed and heat treated $\text{Bi}_{90}\text{Sb}_{10}$ alloy: (i) bright coarse grains and (ii) dark coarse grains.

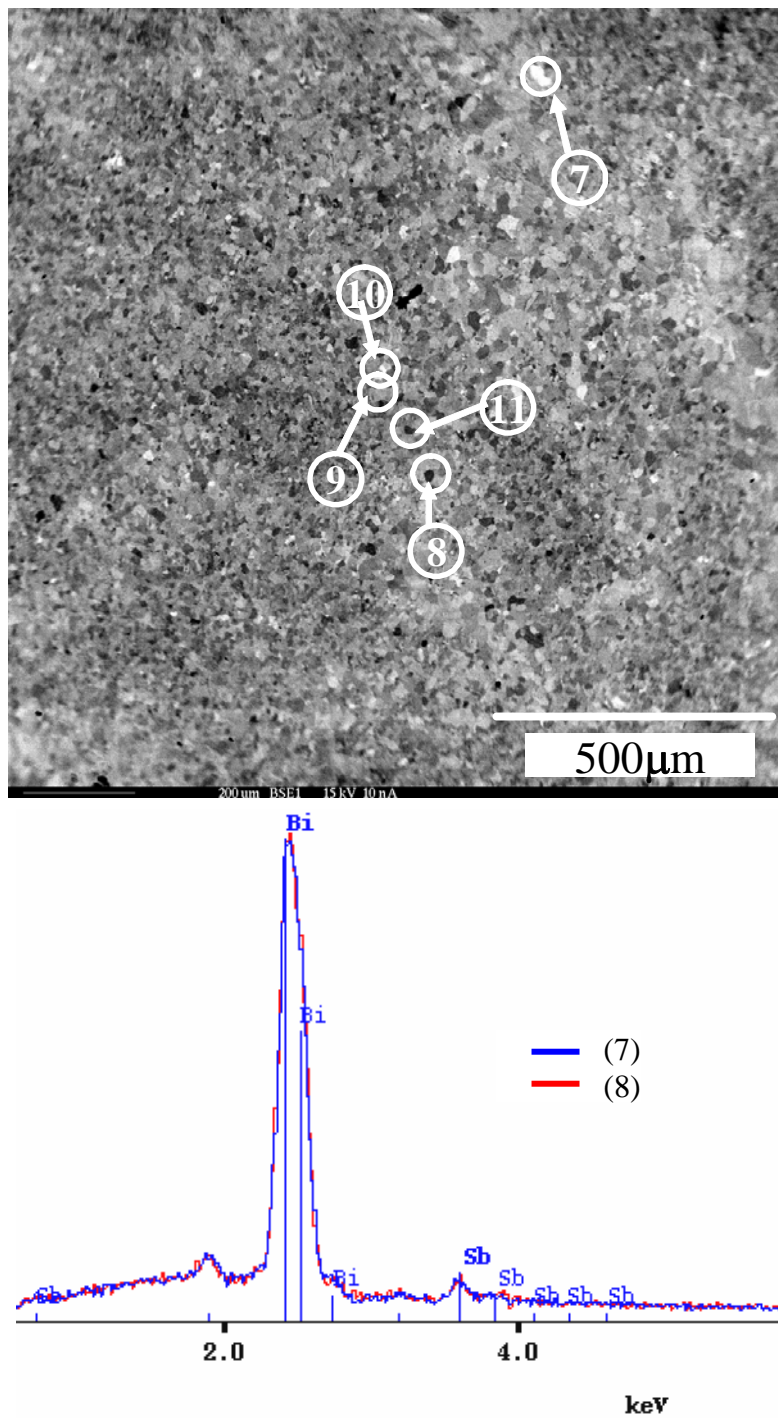


Figure 45. Microprobe analysis with EDS of fine grains after four extrusion passes of preprocessed and heat treated Bi₉₀Sb₁₀ alloy: bright fine grain (7) and dark fine grain (8).

Table 6. Chemical composition of four extrusion pass Bi-Sb after preprocessing and heat treatment analyzed by WDS. Examined locations displayed in Figure 44 and 45.

Grain size	Locations	Bi (at%)	Sb (at%)
Coarse grains	1	92.7	7.3
	2	92.9	7.1
	3	93.2	6.8
	4	92.7	7.3
	5	93.4	6.6
	6	93.9	6.1
	Average	93.1	6.9
Fine grains	7	90.7	9.3
	8	87.7	12.3
	9	88.0	12.0
	10	87.7	12.3
	11	87.3	12.8
	Average	88.3	11.7

average antimony content in coarse grains and fine grains is 6.6-7.3 at% and 9.3-12.8 at% respectively. The antimony content in the coarse grains is lower than that in the fine grains. But, the difference in composition between the fine-grain and coarse-grain area is less in this case than for all of the materials processed without a prior long term heat treatment. This decrease in chemical difference also has had a positive influence on the grain refinement.

CHAPTER V

DISCUSSION

In this study, cast Bi-Sb alloy was processed with severe plastic deformation (SPD) via ECAE and area reduction angular extrusion under various conditions namely: extrusion temperature (220-250°C), extrusion rate (0.1-0.6 in/min), the amount of total plastic strain (four to eight passes), route (A and C), reduced exit channel area (half and quarter area of inlet area), and prior heat treatment (100 hours at 250°C and 10^{-3} torr). All material was preprocessed (four passes of route B_C) in order to eliminate differences in the starting material due to differences arising from the extremely large-grained cast microstructure.

The initial cast grains are refined through dynamic recrystallization during deformation at elevated temperature. However, the dynamically recrystallized microstructure shows bimodal grain size: one area is fine-grained with approximately 5-30µm diameter grains and the other area is coarse-grained with approximately 50-300µm diameter grains. The development of the bimodal microstructure is caused by two main factors: one is chemical inhomogeneity from the initial cast material and the other is related to dynamic recrystallization mechanisms. The effects of chemical homogeneity and dynamic recrystallization on grain refinement are discussed in the following sections.

Plastic deformation at elevated temperature in brittle Bi-Sb alloy involves a considerable contribution from basal plane slip (cleavage plane), twinning and recrystallized grain rotation. Although the basal plane slip is dominant in plastic

deformation of Bi-Sb alloys, twinning and grain rotation are also important mechanisms of texture evolution. The ECAE process leads to rearrangement of grains depending on the route employed. Different combinations of shear plane, shear direction, and number of extrusion passes for multipass extrusions are possible. The texture evolution of various routes, number of extrusion passes, and area reduction in the exit channel will be discussed in the following section.

5.1. Grain refinement of cast Bi-Sb alloys

5.1.1. Chemical homogeneity effects on grain refinement

Chemical homogeneity of cast Bi-Sb alloy is an important factor in grain refinement of Bi-Sb alloys when plastic deformation breaks up the microstructure. The initial cast alloy shows a large Sb gradient (from 33 at% to almost 0.2 at%) from one region to the next (50-several hundreds of microns). The segregation in cast ingot is mainly induced by the large temperature difference between liquidus and solidus line according to the phase diagram. Another possibility of segregation is density of Bi and Sb. The gravity effects on densities of materials may induce the segregation. Even though the high Sb concentration area gradually decreases as the number of extrusion passes increases, the bimodal chemical composition and bimodal grain size microstructure remained in all processed samples. The range of Sb concentration in the processed samples (preprocessing + one pass of ECAE and preprocessed + one pass of half exit area extrusion) which do not receive homogeneous strain vary from 0.5 at% to 20 at% for the cases without prior heat treatment. The bimodal microstructure shows a high Sb concentration (average Sb: 12.2 at%, varying between 2.5 at% and 19.7 at%) in the fine-

grain area and a low Sb concentration (average Sb: 2.7 at%, varying between 0.5 at% to 5.7 at%) in the coarse-grain area (from the EDS and WDS results).

Long-term heat treatment to reduce composition gradient by diffusion is an effective method to homogenize the chemical composition for Bi-Sb alloys. A sample was heat treated at temperature 250°C for 100 hours after preprocessing and further processed with four extrusion passes via route B_C. The fine grains produced during preprocessing grew and formed 100-300µm grain sized microstructure after heat treatment of preprocessed Bi-Sb alloy.

The heat treated and ECAE processed sample shows improved grain refinement and a more homogeneous chemical ratio of Bi and Sb. Although the average fine-grain size (approximately 10 µm) of the heat treated and further deformed sample is similar to that of samples prepared without heat treatment, the percentage of fine-grain area increases dramatically to 95 %, and the coarse-grain size decreases to approximately 50-150µm. Following the long-term heat treatment the grains grow, and the grain size increases approximately 300µm. Considering this fact, the percentage increase in fine-grain area is significant. Clearly, a more uniform chemical composition of material is much more efficient for grain refinement during hot plastic deformation. Thus, heat treatment between hot deformation processes is strongly related to the level of grain refinement in Bi-Sb alloys. The average fine-grain size, coarse-grain size, and percentage of fine-grain area for the various extrusion conditions are summarized in Table 7 and 8.

However, the bimodal microstructure still remains in the heat treated sample, following SPD processing, and a corresponding bimodal chemical composition also

Table 7. Refined grain size and percent of fine grain area for preprocessed Bi₉₀Sb₁₀ alloys (four extrusion pass of ECAE via route B_C).

Billet ID	Punch speed (in/min)	Extrusion Temperature (°C)	Average fine-grain size(μm)	Coarse-grain size(μm)	Percent of fine grain area (%)
1	0.1	250	15	50~300	55
2	0.3	250	11	50~300	59
3	0.6	250	9	50~300	56
4	0.3	235	9	50~300	56
5	0.3	220	7	50~300	48

Table 8. Summarized refined grain size and percent of fine grain area with further deformation of preprocessed Bi₉₀Sb₁₀ alloy billets (preprocessed conditions: 4Bc at 235°C and 0.3 in/min).

Billet ID	Area of exit channel	Number of extrusion passes	Route	Average fine-grain size(μm)	Coarse-grain size(μm)	Percent of fine grain area (%)
6	A _{inlet}	1	A	10	50~300	64
7	A _{inlet}	2	A	9	50~300	72
8	A _{inlet}	4	A	9	50~300	89
9	A _{inlet}	2	C	11	50~300	73
10	A _{inlet}	4	C	10	50~300	82
11*	A _{inlet}	4	B _C	10	50-150	95
12	1/2 A _{inlet}	1	A	10	50-250	75
13	1/4 A _{inlet}	1	A	10	50-200	86

* Material heat treated at 250°C for 100 hours in vacuum prior to SPD processing.

remains between the fine and coarse grain regions. The antimony content in cast, fine, and coarse grains of Bi-Sb alloy billets processed with different extrusion conditions is summarized in Table 9. The average Sb concentration is 11.7 at% in fine grains and 6.9 at% in coarse grains, and the variations of Sb concentrations in fine grains (9.3 – 12.8 at %) and in coarse grains (6.1 – 7.3 at %) for the long-term heat treated sample are considerably reduced compared to samples prepared without prior long-term heat treatment.

Based on this study, the development of the bimodal microstructure in Bi-Sb alloy is strongly related to the Sb concentration gradient in the initial cast grains. A high Sb concentration area in cast grains form fine grains and a low Sb concentration area forms coarse grains during hot plastic deformation. The level of grain refinement is also strongly related to the Sb concentration gradient. One of the significant reasons for

Table 9. Summary of Sb content in cast, fine, and coarse grains of nominal Bi₉₀Sb₁₀ alloy billets processed following various deformation routes.

Billet ID	Area of exit channel	Number of extrusion passes	Route	Sb content in fine grains (at%)	Sb content in coarse grains (at%)
Cast				0.2 - 33	
6	A _{inlet}	1	A	6.5 – 15.8	0.5 – 4.9
11*	A _{inlet}	4	B _C	9.3- 12.8	6.1 – 7.3
12	1/2 A _{inlet}	1	A	2.5 – 19.7	1.5 – 5.7

* Material heat treated at 250°C for 100 hours in vacuum prior to SPD processing.

bimodal microstructure is the difference in atomic radius between Bi atom (1.55 \AA for neutral atoms) and Sb atom (1.45 \AA for neutral atoms).

The Bi-Sb alloy forms complete substitutional solid solutions according to the phase diagram (Figure 5). When an Sb atom with a smaller atomic radius is substituted for a Bi atom, lattice strain fields are induced near the Sb atoms among Bi atoms as illustrated in Figure 46. The tensile lattice strains imposed on the host atoms (Bi) by smaller substitutional atoms (Sb) is shown in Figure 46 (i). A group of smaller substitutional

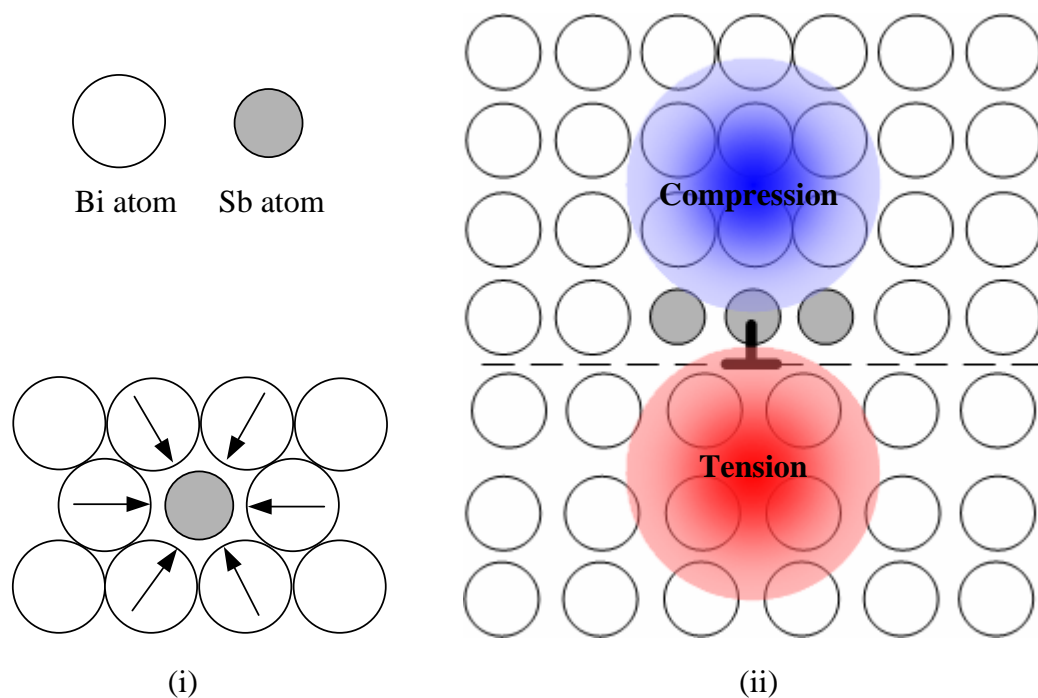


Figure 46. Illustrations of lattice strains induced by substituted atoms in Bi-Sb alloy: (i) tensile lattice strains imposed on the host atoms (Bi) due to a smaller substitutional atom (Sb), and (ii) dislocation lattice strains induced by a group of smaller substitutional atoms.

atoms (Sb) produce a dislocation accommodation structure and induce lattice strains. There are compressive and tensile lattice strains around the dislocation as shown in Figure 46 (ii). The magnitude of the strains induced corresponds to the level of Sb concentration. A high Sb concentration area has more lattice distortion and low Sb concentration area has less lattice distortion.

Lattice strain fields interact with dislocations generated during hot deformation. The high Sb concentration area in cast grains recrystallize more effectively and form fine grained microstructure during hot deformation because of large lattice strain. A low concentration area of Sb refines less effectively and forms coarse grains. Thus, fine-grain areas are produced in the high concentration Sb areas and the coarse-grain areas are produced in low concentration Sb areas through the process of dynamic recrystallization. During the hot deformation process, Sb atoms from high Sb concentration areas diffuse into the low Sb concentration areas and form a more homogeneous chemical composition.

5.1.2. Dynamic recrystallization mechanisms for grain refinement

Grain refinement of cast Bi-Sb grains occurs mainly by the combination of two different dynamic recrystallization mechanisms during hot deformation. First, large cast grains form sub-grain boundaries by the misorientation (tilting or twisting) during plastic deformation at elevated temperature. The sub-grains rotate and produce a new set of high angle grain boundary as shown in Figure 47 (i). Second, dislocations induced by strain move to pre-existing grain boundaries under strain and accumulate near the boundaries. The accumulated dislocations reorganize at elevated temperature and

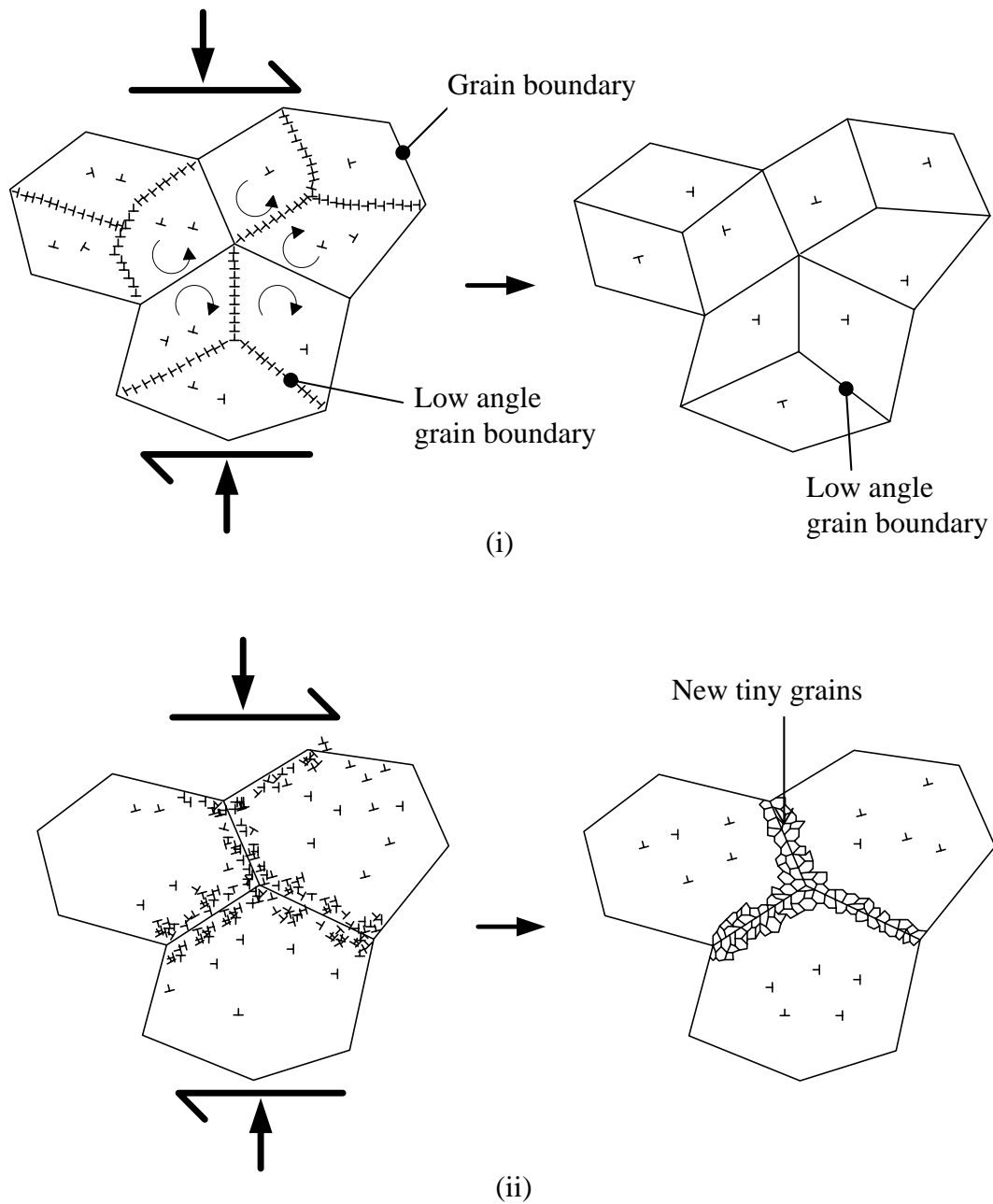


Figure 47. Illustrations of dynamic recrystallization mechanisms in Bi-Sb alloy during hot deformation: (i) sub-grains are formed by applied strain and produce new high angle grain boundaries by rotations and (ii) dislocations induced by strain are accumulated in the vicinity of old grain boundaries. Tiny grains form in the accumulated dislocation area and develop new high angle grain boundaries.

produce a new set of sub-grains followed by sub-grain growth which eliminates dislocations, as shown in Figure 47 (ii).

The microstructure of Bi-Sb alloy develops a bimodal grain size character after hot multipass ECAE and area reduction angular channel extrusion process, as shown in Table 7 and 8. The coarse grain size remains similar even after many extrusion passes, but the fine-grain area gradually increases with added plastic strain as shown in the Table. The bimodal microstructure suggests that different dynamic recrystallization mechanisms occur during hot deformation. The first mechanism occurs more likely in the preprocessed extrusion process of cast Bi-Sb alloy. Cast grains are difficult to break up because large grain fragments interlock with each other at an early stage of grain refinement. Thus, sub-grains in the cast grains are formed by the misorientation under strain and rotate to produce high angle grain boundaries. This mechanism most likely produces coarse grains (100~200 μm).

The second mechanism is active during the entire hot deformation process and produces fine grains (5~30 μm) near pre-existing grain boundaries. This mechanism is more dominant in later stages of multipass extrusion. The interlocking forces between the large grains gradually reduce as the number of extrusion passes increases because fine grains near the coarse grain boundaries assist rotation of the coarse grains under further strain. Thus, the coarse grains are gradually refined by increased deformation. These dynamic recrystallization mechanisms for Bi-Sb alloy occur simultaneously during hot deformation.

5.2. Texture development of Bi-Sb alloys

Shear planes and shear directions in multipass ECAE processing are an important factor for development of texture in Bi-Sb alloy. A strong cast texture develops into weak textures with basal poles oriented approximately 5-40° to the longitudinal plane after preprocessing (four extrusion passes of route B_C) regardless of extrusion temperature and rate. The maximum values of basal poles and angles for preprocessed and processed materials are summarized in the Table 10 and 11. As shown in Figure 10

Table 10. Summary of maximum intensity values (logarithmic scale) of basal poles and their positions (degrees) for preprocessed Bi-Sb alloys.

Billet ID	Punch speed (in/min)	Extrusion Temperature (°C)	Maximum values of basal poles	Angle (Chi)	Angle (Phi)
1	0.1	250	8.2	40	175
			6.4	15	0
			6.4	20	260
2	0.3	250	6.1	35	180
			5.9	10	210
			5.8	15	85
3	0.6	250	7.1	25	210
			6.2	30	180
			6.0	5	205
4	0.3	235	6.2	10	220
			6.1	25	240
			5.3	0	190
5	0.3	220	6.0	5	200
			5.7	15	190

Table 11. Summary of maximum values (logarithmic scale) basal poles and their positions (degrees) for preprocessed Bi-Sb alloys.

Billet ID	Area of exit channel	Number of extrusion passes	Route	Maximum values of basal poles	Angle (Chi)	Anlge (Phi)
6	A_{inlet}	1	A	8.3	15	170
				7.4	30	195
				6.5	15	190
7	A_{inlet}	2	A	13.7	10	195
				10.9	10	5
				7.2	30	180
8	A_{inlet}	4	A	12.5	5	170
				4.7	5	335
				4.5	10	280
9	A_{inlet}	2	C	12.8	10	340
				10.1	25	100
				8.5	10	25
10	A_{inlet}	4	C	14.6	25	165
				13.6	5	40
				8.9	15	205
12	$1/2 A_{\text{inlet}}$	1	A	17.3	15	205
				9.4	5	75
				6.7	15	150
13	$1/4 A_{\text{inlet}}$	1	A	49.7	5	95
				19.0	15	90
				11.7	25	80

(ii), shear directions and planes change after each extrusion pass during preprocessing and cause the development of a weak texture. The maximum basal poles have a tendency to incline to 25° , the angle of shear from the extrusion axis.

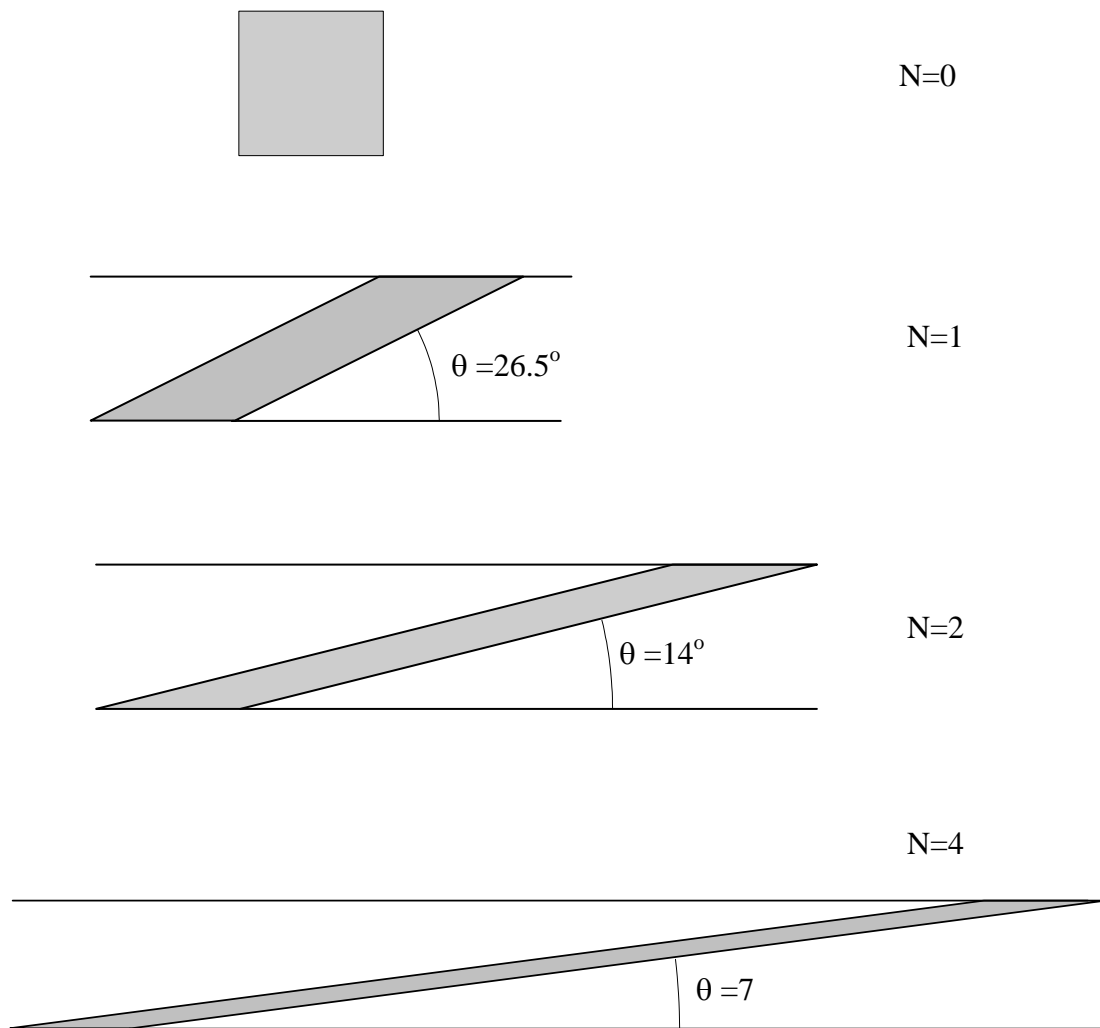


Figure 48. Illustrations for element transformation and angles between transformed element and extrusion axis depending on the number of extrusion pass (N) for route A.

The element transformations following multipass route A processing are illustrated in Figure 48. The transformed elements incline to the extrusion axis as the extrusion number of pass increases via route A. The developed textures of Bi-Sb alloys via route A show similar patterns. The maximum basal poles form at $15-30^\circ$ for one pass, $10-30^\circ$ for two passes, and $5-10^\circ$ for four passes on the longitudinal plane normal direction. The maximum basal poles incline closer to the longitudinal plane normal direction as the number of extrusion increases for route A processing.

However, the maximum basal poles, for multipass route C processing, form $10-25^\circ$ for two passes and $5-25^\circ$ for four passes on the longitudinal plane normal direction. The maximum basal poles have a tendency to incline to 25° , the angle between a transformed element by simple shear and the extrusion axis. The deformed element is restored to its original shape after reverse shear following each even numbered pass.

The texture gets stronger with increased plastic deformation following route A and C processing. Based on the results of texture development in Bi-Sb alloy, Figure 49 schematically illustrates the hypothesized texture evolution for route A and C processing. The basal plane is represented by a hexagonal element in Figure 49. The gray hexagonal element after a first extrusion pass aligns to incline to 26.5° , the angle between the element transformed by simple shear and the extrusion axis. The gray hexagonal element in the inlet channel is oriented differently for the second pass because of different billet rotations between route A (0° rotation) and C (180° rotation). However, the hexagonal element in both route A and C is inclined to the extrusion axis after the second pass. It is hypothesized that the rectangular element experiences a rigid body rotation and simple

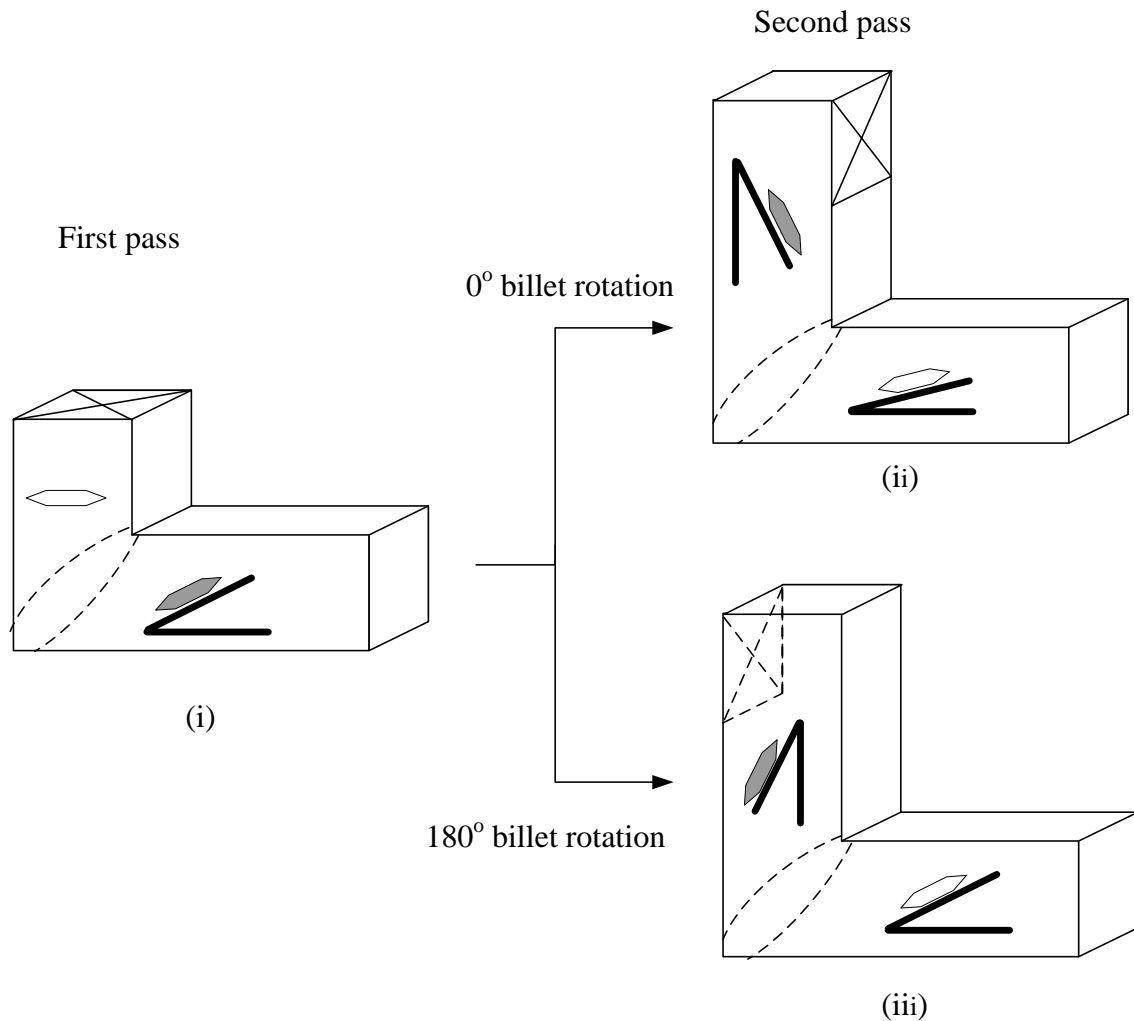


Figure 49. Schematic illustration for different orientations of a material element (representing the basal plane hexagon) after the first (i) and second pass (ii) route A and (iii) route C.

shear for route A extrusion. While the element experiences rigid body rotation and simple shear, the grains rearrange and a stronger texture develops. The hexagonal element for route C experiences just simple shear without rigid body rotation. Although

basal slip is a dominant mechanism for plastic deformation, grains misoriented to the shear plane are rearranged by the simple shear and texture is enhanced.

Figure 50 schematically illustrates texture evolution for area reduction exit channel extrusion. The transformed elements incline more to the extrusion axis as the reduced area channel areas are reduced. The angles between the transformed element and extrusion axis are 26.5° , 18.4° and 11.3° for equal, half and quarter area exit channel extrusions as shown in Figure 50. The development of textures for Bi-Sb alloy, from the experimental results, show similar patterns. The maximum basal poles, from the experimental results, form near 15° for half area extrusion and near 5° for quarter area extrusion. The textures obtained from area reduction exit channel extrusions are stronger than those from the simple ECAE process. As the reduced area in exit channel decreases, the texture gets stronger and the basal planes aligns closer to the longitudinal plane.

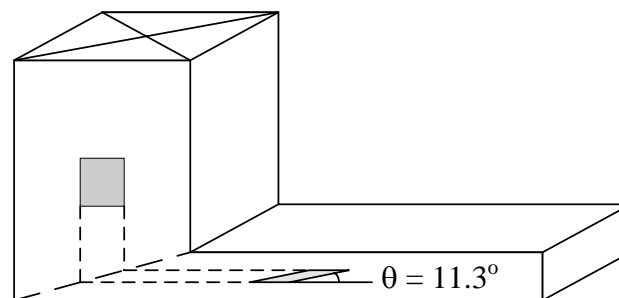
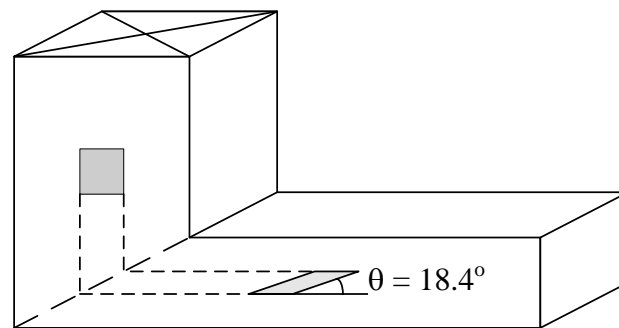
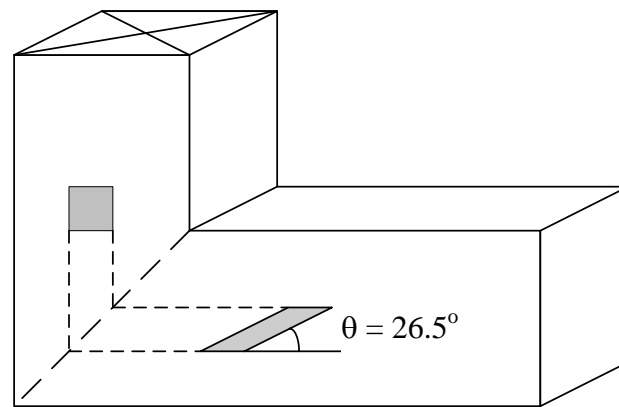


Figure 50. Illustrations for element transformation and angles between transformed element and extrusion axis depending on the exit channel area: (i) equal to inlet area (ii) half inlet area, and (iii) quarter inlet area.

CHAPTER VI

FINDINGS AND CONCLUSIONS

This study demonstrated the process of grain refinement and texture evolution via ECAE and reduction area exit channel extrusion for cast Bi-Sb alloys. The grain refinement mechanism for Bi-Sb alloy is dynamic recrystallization which occurs during plastic deformation at elevated temperature. Basal plane slip and grain rotation are the dominant mechanisms of texture evolution.

The initial cast Bi-Sb ingot material was large grained and chemically inhomogeneous. Various microstructures were developed depending on the severe plastic deformation conditions. The homogeneity of chemical composition is strongly related to the microstructural evolution during hot plastic deformation. Some of the effects of the various extrusion conditions, including area reduction ratio of the exit channel, homogeneity of chemical composition, and heat treatment were identified and found to be especially important for grain refinement and texture development of cast Bi-Sb alloy. The findings (F) and conclusions (C) that can be drawn from this work include the following:

F. 1. Cast Bi-Sb alloy has large grains (0.3-3mm) and shows significant chemical microsegregation (Sb: 0-33 at%). Regions of high Sb concentration are separated by distances of 50 to several hundreds of microns.

- F. 2. Severe plastic deformation preprocessing (ECAE via 4B_C) refines the microstructure but results in a bimodal grain size distribution: fine-grain size: 5-30 μm; coarse-grain size: 50-300μm; percentage of fine-grain area: 50-60 %.
- F. 3. ECAE processing of preprocessed materials leads to: fine-grains size: 5-30 μm; coarse grain size 50-300μm; percentage of fine-grain area: up to 90 %; antimony content in fine grains (for one extrusion pass): 6.5-15.8 at %; antimony content in coarse grains (for one extrusion pass): 0.5-4.9 at %.
- F. 4. ECAE processing combined with a reduced exit channel area leads to: fine-grain size: 5-30 μm; coarse-grain size: 50-300μm; percentage of fine-grain area: 75 % for half area exit channel and 86 % for quarter area exit channel; antimony content in fine grains (for half area exit channel): 2.5-19.7 at %; antimony content in coarse grains (for half area exit channel): 1.5-5.7 at %.
- F. 5. A long-term homogenizing heat treatment (100 hours at 250°C under vacuum: 10⁻³ torr) after 4B_C preprocessing results in large grains with diameters 100-300μm grain size.
- F. 6. ECAE processing (four extrusion passes of route B_C) of preprocessed and homogenized Bi-Sb alloy results in: fine-grain size: 5-30 μm; coarse-grain size: 50-150μm; percentage of fine-grain area: up to 95 %; antimony content in fine grains: 9.3-12.8 at %; antimony content in coarse grains: 6.1-7.3 at %.
- F. 7. Strong basal poles are formed in various directions, normally perpendicular to solidification direction, for cast Bi-Sb alloy.

F. 8. Weak textures are formed after preprocessing (four extrusion passes of route B_C) and the basal poles are oriented approximately 5~40° to the longitudinal plane regardless of the extrusion temperature and rate.

F. 9. The general texture of ECAE processed material is characterized by:

(i) For route A processing, basal poles have a tendency to align closer to the longitudinal plane normal as the number of extrusion passes increases, and the strength of texture increases as the number of extrusion passes increases.

(ii) For route C processing, basal poles have a tendency to align at around 25° to the longitudinal plane normal, and the strength of texture increases as the number of extrusion passes increases.

F. 10. The general texture of material processed by exit channel reduction area extrusion is that the basal poles have a tendency to align towards the longitudinal plane normal, and the strength of texture increases dramatically as the area of the exit channel decreases.

C. 11. The refined grain size decreases as the extrusion temperature decreases and as the extrusion rate increases.

C. 12. The refined grain size remains similar regardless of extrusion route, number of extrusion passes, and area reduction ratio of the exit channel. The shearing pattern and magnitude of strain do not affect grain size during processing by hot plastic deformation.

C. 13. The percentage of fine-grain area increases gradually as the number of extrusion passes increases, for simple ECAE processing.

C. 14. Multipass route A processing is more effective for grain refinement compared to route C processing because of the benefit of intersecting shear planes.

C. 15. Exit channel area reduction extrusion is more effective for grain refinement than the ECAE processing.

C. 16. Chemical inhomogeneity and dynamic recrystallization mechanisms in Bi-Sb alloy induce a bimodal (distribution of grain size) microstructure after hot plastic deformation:

(i) High Sb content area is effectively refined to fine grains.

(ii) Low Sb content area does not refine well and results in coarse grains.

(iii) New coarse grains are formed by accumulation / reorganization of dislocation and rotation of large grains.

(iv) New fine grains are formed by reorganizing accumulated dislocations induced by strain at grain boundaries.

C. 17. A long-term high-temperature heat treatment homogenizes chemical segregation and enables more effective microstructural break down by severe plastic deformation processing.

C. 18. The extrusion route and number of extrusion passes are important for texture evolution in Bi-Sb alloy:

(i) route A processing: texture enhancement occurs by rigid body rotation and simple shear as the number of extrusion passes increases.

(ii) route C processing: texture enhancement occurs by simple shear as the number of extrusion passes increases.

(iii) route B_C processing: weak texture is developed because of changing shear planes and directions for each pass during multipass extrusion.

C. 19. Exit channel reduction area extrusion is very effective for microstructural break down and produces strong texture.

CHAPTER VII

SUGGESTIONS FOR FURTHER STUDY

There remain unresolved questions with regard to $\text{Bi}_{90}\text{Sb}_{10}$ alloy processed via severe plastic deformation. First of all, experiments are needed to homogenize the chemical composition of cast materials. A long-term heat treatment of cast ingots and perhaps an intermediate heat treatment between SPD processing steps would be to homogenize the microstructure of $\text{Bi}_{90}\text{Sb}_{10}$ alloy. Second, the experiments conducted in this work did not evaluate the thermoelectric properties of the SPD processed materials. Experiments need to be carried out to study the effect of microstructure and grain orientation distribution on thermoelectric properties such as the Seebeck coefficient, electrical resistivity and thermal conductivity. Third, experiments need to study on recrystallization temperature of $\text{Bi}_{90}\text{Sb}_{10}$ alloy during severe plastic deformation. The recrystallization temperature will be decided by turning the heater off during the extrusion at a constant punch speed. Fourth, processing larger and longer billets via SPD would help with analysis of microstructure and thermoelectric properties and improve productivity.

REFERENCES

- [1] R. E. Reed-Hill, and R. Abbaschian, *Physical Metallurgy Principles*, 3rd ed., PWS Publishing Company, Boston, MA (1994).
- [2] R.Z. Valiev, R.K. Islamgaliev, and I.V. Alexandrov, *Prog. Mater. Sci.* 45 (2000) 103.
- [3] V.M. Segal, *Mater. Sci. Eng. A* 197 (1995) 157.
- [4] V.M. Segal, K.T. Hartwig, R.E. Goforth, *Mater. Sci. Eng. A* 224 (1997) 107.
- [5] V.M. Segal, *Mater. Sci. Eng. A*, 271 (1999) 322.
- [6] V.M. Segal, *Mater. Sci. Eng. A*, 345 (2006) 336.
- [7] R.D. Field, K.T. Hartwig, C.T. Necker, J.F. Bingert, and S.R. Agnew, *Metall. Trans A*, 33 (2002) 965.
- [8] H.-S. Kim, D.-H. Joo, M.-H. Kim, S.-K. Hwang, S.-I. Kwun, and S.-W. Chae, *Mater. Sci. Tech.* 19 (2003) 403.
- [9] V.V. Stolyarov, L.Sh. Shuster, M.Sh. Migranov, R.Z. Valiev, and Y.T. Zhu, *Mater. Sci. Eng. A*, 371 (2004) 313.
- [10] S.L. Semiatin, V.M. Segal, R.L. Goetz, R.E. Goforth, and T. Hartwig, *Scr. Mater.*, 33 (1995) 535.
- [11] S.L. Semiatin and D.P. Delo, *Mater. Des.* 21 (2000) 311.
- [12] J-T Im, K.T. Hartwig, J. Sharp, *Acta Mater.*, 52 (2004), 49-55.
- [13] S.S. Kim, S. Yamamoto, and T. Aizawa, *J. Alloys Compd*, 375 (2004) 107.
- [14] W.M. Yim and A. Amith, *Solid –State Electron.* 15 (1972) 1141.
- [15] M. G. Fee, *Appl. Phys. Lett.* 62 (1993) 1161.
- [16] N. A. Sidorenko, *Proc. of the 13th Int. Conf. on Thermoelectrics*, Kansas City, MO, (1994) 260.
- [17] R.M. Lopez, B. Lenoir, X. Devaux, A. Dauscher, W. Dummler, and H. Scherrer, *Scripta Mater.* 37 (1997) 219.

- [18] Y. Suse, Y.H. Lee, H. Morimoto, T.Koyonagi, K. Mastsubara, and A. Kawamoto, Proc. of the 12th Int. Conf. on Thermoelectrics, Yokohama, Japan (1993) 248.
- [19] R. Martin-Lopez, A. Dauscher, H. Scherrer, J. Hejtmanek, H. Kenzari, and B. Lenoir, Appl. Phys. A, 68 (1999) 597.
- [20] Yong-Hoon Lee, T. Koyanagi, T. Tabuchi, and S. Sano, Proc. of the 22th Int. Conf. on Thermoelectrics, France, (2003) 294.
- [21] H.J. Goldsmid, Electronic Refrigeration, Pion Limited, London (1986).
- [22] R.G. Chambers, Electron in Metals and Semiconductors, Chapman and Hall, London (1990).
- [23] R. Berman, Thermal Conduction in Solids, Clarendon Press, Oxford, UK. (1976).
- [24] S.O. Kasap, Principles of Electronic Materials and Devices, 2nd ed., McGraw-Hill, New York (2001).
- [25] D.Y. Chung, T. Hogan, P. Brazis, M. Rocci-Lane, C. Kannewurf, M. Bastea, C. Uher, and M. G. Kanatzidis, Science, 287 (2000) 1024.
- [26] H. Beyer, J. Nurnus, H. Bottner, and A. Lambrecht, Appl. Phys. Lett. 80 (2002) 1216.
- [27] J. P. Dismukes, L. Ekstrom, E. F. Steigmeier, I. Kudman, and D. S. Beers, J. Appl Phys, 35 (1964) 2899.
- [28] F.D. Rosi, Solid State Electron. 11 (1968) 833.
- [29] H.J. Goldsmid, J. E. Guitornich, and M. M. Kaila, Solar Energy 24 (1980) 435.
- [30] J. G. Stockholm, Proc. of the 16th Int. Conf. on Thermoelectrics, Dresden, Germany (1997) 37.
- [31] G.E. Smith and R. Wolfe, J. Appl. Phys. 33 (1962) 841.
- [32] H.J. Goldsmid, K.K. Gopinathan, D.N. Matthews, K.N.R Taylor, and C.A. Baord, J. Phys. D: Appl. Phys. 21 (1988) 344.
- [33] Z.M. Dashevskii, N. A. Sidorenko, N.A. Tsvetkova, C. Ya Skipldarov, and A.B. Mosolov, Supercon. Sci. Technol. 5 (1992) 690.
- [34] S. Golin, Phys. Rev. 166 (1968) 643.

- [35] R.W.G. Wyckoff, *Crystal Structures*, 1, Interscience, New York (1960).
- [36] D. Schiferl and C.S. Barrett, *J. Appl. Cryst.* 2 (1969) 30.
- [37] A.L. Jain, *Phys. Rev.* 114 (1959) 1518.
- [38] D.M. Brown and F.K. Heumann, *J. Appl Phys*, 35 (1964) 1947.
- [39] L.M. Falicov and P.J. Lin, *Phys. Rev.* 141 (1966) 562.
- [40] P. Cucka and C.S. Barrett, *Acta Cryst.* 15 (1962) 865.
- [41] Thaddeus B. Massalski, *Binary Alloy Phase Diagrams*, American Society for Metals, Metals Park, OH (1986) 536.
- [42] G. Schneider, R. Herrmann, and B. Christ, *J. Crystal Growth*, 52 (1981) 485.
- [43] B. Lenoir, M. Cassart, J.-P. Michenaud, H. Scherrer, and S. Scherrer, *Phys. Chem. Solids*, 57 (1996) 89.
- [44] G.N. Kozhemyakin and L.G. Kolodyazhnaya, *J. Crystal Growth*, 147 (1995) 200.
- [45] V.S. Zemskov, A.D. Belaya, U.S. Beluy, and G.N. Kozhemyakin, *J. Crystal Growth*, 212 (2000) 161.
- [46] G.N. Kozhemyakin, M.A. Nalivkin, M.A. Rom, and P.V. Mateychenko, *J. Crystal Growth*, 263 (2004) 148.
- [47] M. W. Barsoum, *Fundamentals of Ceramics*. McGraw-Hill, Bristol, UK. (1997).
- [48] G. Cochrane and W.V. Youdelis, *Metall. Trans.* 3 (1972) 2843.
- [49] R. Martin-Lopez, B. Lenoir, X. Devaux, A. Dauscher, and H. Scherrer, *Mater. Sci. Eng. A* 248 (1998) 147.
- [50] H. Liu, Y. Wu, R. Huang, C. Song, and L. Li, *J. Phys. Chem. Solids*, 67 (2006) 1492.
- [51] X. Devaux, F. Brochin, A. Dauscher, B. Lenoir, R. Martin-Lopez, and H. Scherrer, and S. Scherrer, *Nanostructured Materials*, 8 (1997) 137.
- [52] X. Devaux, F. Brochin, R. Martin-Lopez, and H. Scherrer, *J. Phys. Chem. Solids*, 63 (2002) 119.

- [53] J. W. Christian and S. Mahajan, *Prog. Mater. Sci.* 39 (1995) 1.
- [54] S. R. Kalidindi, *J. Mech. Phys. Solids*, 46 (1998) 267.
- [55] E. Tenchoff, *Metall. Trans. A*, 9 (1978) 1401.
- [56] R. Gehrmann, M. M. Frommert, and G. Gottstein, *Mater. Sci. Eng. A*, 395 (2005) 338.
- [57] A. Staroselsky and L. Anand, *Int. J. Plasticity*, 19 (2003) 1843.
- [58] V. Gupta, *Acta Metall. Mater*, 41 (1993) 3223.
- [59] U.F. Kocks, C.N. Tome, and H.-R. Wenk, *Texture and Anisotropy*, Cambridge, UK. (2000).
- [60] W.D. Callister, Jr., *Materials Science and Engineering An Introduction*, 5th ed., John Wiley & Sons, New York (2000).
- [61] H.J. McQueen and C.A.C. Imbert, *J. Alloys Compd*, 378 (2004) 35.
- [62] M.M. Myshlyaev, H.J. McQueen, A. Mwembela, and E. Konopleva, *Mater. Sci. Eng. A*, 337 (2002) 121.
- [63] A. Mwembela, E.B. Konopleva, and H.J. McQueen, *Scr. Mater.*, 37 (1997) 1789.
- [64] J.A. del Valle, M.T. Perez-Parado, and O.A. Ruano, *Mater. Sci. Eng. A*, 355 (2003) 68.
- [65] H. Fukutomi, S. Takagi, K. Aoki, M. Nobuki, H. Mecking, and T. Kamijo, *Scr. Mater.*, 25 (1991) 1681.
- [66] S.E. Ion, F.J. Humphreys, and S.H. White, *Acta Metall.*, 30 (1982) 1909.
- [67] S.H. White, M.R. Drury, S.E. Ion, and F.J. Humphreys, *Phys. Earth Planet. Inter.*, 40 (1985) 201.
- [68] M.R. Drury, F.J. Humphreys, and S.H. White, *Phys. Earth Planet. Inter.*, 40 (1985) 208.
- [69] M.R. Drury and J.L. Urai, *Tectonophysics*, 172 (1990) 235.
- [70] Y. Iwashita, Z. Horita, M. Nemoto, and T.G. Landon, *Acta Mater.*, 46 (1998) 3317.

- [71] Q. Wei, T. Jiao, S. N. Mathaudhu, E. Ma, K. T. Hartwig and K. T. Ramesh, *Mater. Sci. Eng. A*, 358 (2003) 266.
- [72] C. Xu, M. Furukawa, Z. Horita, and T.G. Langdon, *Mater. Sci. Eng. A*, 398 (2005) 66.
- [73] M. Furukawa, Z. Horita, and T.G. Langdon, *Mater. Sci. Eng. A*, 332 (2005) 97.
- [74] G.P. Purcek, B.S. Altan, I. Miskioglu, and P.H. Ooi, *J. Mater. Proc. Tech.* 148 (2004) 279.
- [75] M. Furukawa, Y. Ma, Z. Horita, M. Nemoto, R. Z. Valiev, and T.G. Langdon, *Mater. Sci. Eng. A*. 241 (1998) 122.
- [76] V.V. Stolyarov, Y.T. Zhu, I.V. Alexandrov, T.C. Lowe, and R.Z. Valiev, *Mater. Sci. Eng. A*. 299 (2001) 59.
- [77] V.V. Stolyarov, Y.T. Zhu, I.V. Alexandrov, T.C. Lowe, and R.Z. Valiev, *Mater. Sci. Eng. A*, 343 (2003) 43.
- [78] D.H. Shin, I. Kim, J. Kim, and Y.T. Zhu, *Mater. Sci. Eng. A*, 334 (2002) 239.
- [79] D.H. Shin, I. Kim, J. Kim, Y.S. Kim, and S.L. Semiatin, *Acta Mater.*, 51 (2003) 983.
- [80] Y.G. Ko, D.H. Shin, K.T. Park, S. C.S. Lee, *Scr. Mater.*, 54 (2006) 1785.
- [81] G.G. Yapici, I. Karaman, and H.J. Maier, *Mater. Sci. Eng. A*, 434 (2006) 294.
- [82] L.R. Cornwell, K.T. Hartwig, R.E. Goforth, and S.L. Semiatin, *Mater. Char.* 37 (1996) 295.
- [83] G.G. Yapici, I. Karaman, and Z.-P. Luo, *Acta Mater.*, 54 (2006) 3755.
- [84] W.S. Choi, H.S. Ryoo, S.K. Hwang, M.H. Kim, S.I. Kwun, and S.W. Chae, *Metall. Trans A*, 33 (2002) 973.
- [85] S.H. Yu, Y.B. Chun, S.K. Hwang, and D.H. Shin, *Philosophical Mag.* 85 (2005) 345.
- [86] B.S. Lee and M.H. Kim, *Mater. Sci. Eng. A*, 423 (2006) 180.
- [87] B.S. Lee and M.H. Kim, *Mater. Sci. Eng. A*, 416 (2006) 150.
- [88] A. Yamashita, Z. Horita, and T.G. Langdon, *Mater. Sci. Eng. A*, 300 (2001) 142.

- [89] T. Mukai, M. Yamanoi, H. Watanabe, and K. Higashi, *Scr. Mater.*, 45 (2001) 89.
- [90] J. Koike, T. Kobayashi, T. Mukai, H. Watanabe, M. Suzuki, K. Maruyama, and K. Higashi, *Acta Mater.* 51 (2003) 2055.
- [91] H. Watanabe, A. Takara, H. Somekawa, T. Mukai, and K. Higashi, *Scr. Mater.* 52 (2005) 449.
- [92] H. Somekawa, and T. Mukai, *Scr. Mater.* 54 (2006) 633.
- [93] W.J. Kim, C.S. An, Y.S. Kim, and S.I. Hong, *Scr. Mater.*, 47 (2002) 39.
- [94] S.R. Agnew, J.A. Horton, T.M. Lillo, and D.W. Brown, *Scr. Mater.*, 50 (2004) 377.
- [95] S.R. Agnew, P. Mehrotra, T.M. Lillo, G.M. Stoica, and P.K. Liaw, *Mater. Sci. Eng. A*, 408 (2005) 72.
- [96] S.R. Agnew, P. Mehrotra, T.M. Lillo, and P.K. Liaw, *Acta Mater.*, 53 (2005) 3135.
- [97] A.V. Nagasekhar, U. Chakkingal, P. Venugopal, *J. Mater. Process. Technol.* 173 (2006) 53.
- [98] J. Seo, K. Park, D. Lee, and C. Lee, *Scr. Mater.* 38, (1998) 477.
- [99] J.M. Schultz, J.P. McHugh and W.A. Tiller, *J. Appl. Phys.* 33 (1962) 2443.
- [100] V.I. Nekhoroshev, *Proc. of the 17th Int. Conf. Thermoelectrics*, Nagoya, Japan, (1998) 159.
- [101] I. J. Ohsugi, T. Kojima, M. Sakata, M. Yamanashi and I. A. Nishida, *J. Appl. Phys.* 76 (1994) 2235.
- [102] I. J. Ohsugi, T. Kojima, and I. Nishida, *J. Appl. Phys.* 68 (1990) 5692.
- [103] K. Fukuda, H. Imaizumi, T. Ishii, F. Toyoda, M. Yamarashi, and Y. Kibayashi, *Proc. of the 14th Int. Conf. on Thermoelectrics*, St. Petersburg, Russia (1995) 135.
- [104] K. Fukuda, H. Imaizumi, T. Ishii, F. Toyoda, and M. Yamarashi, *Proc. of the 15th Int. Conf. on Thermoelectrics*, Pasadena, California (1996) 37.
- [105] T. Kajihara, K. Fukuda, Y. Sato and M. Kikuchi, *Proc. of the 17th Int. Conf. on Thermoelectrics*, Nagoya, Japan (1998) 129.

- [106] S. Miura, Y. Sato, K. Fukuda, K. Nishimura, and K. Ikeda, *Mater. Sci. Eng. A*, 277 (2000) 244.
- [107] J. Seo, D. Cho, K. Park, and C. Lee, *Mater. Res. Bull.* 35 (2000) 2157.
- [108] S.S. Kim, S. Yamamoto, and T. Aizawa, *J. Alloys Compd*, 419 (2006) 306.

VITA

Jae-taek Im was born on September 14, 1969 in Kyeungbuk, Republic of Korea. He was the second born son of Mr. Joong-whan Im and Mrs. Jung-ja Shin. He attended elementary and high school in Daegu, Republic of Korea. He earned his Bachelor of Science degree in materials science and engineering in February, 1997, from Yeung-nam University. He worked in the Optical Fiber manufacturing division at Samsung Electronics in Korea from 1997 to 1998.

In order to pursue a Master of Science and Doctor of Philosophy degree, he enrolled in Texas A&M University, College Station, TX in the fall of 1998. He earned his M.S. and Ph.D. degree in mechanical engineering in May 2001 and May 2007 from Texas A&M University, specializing in the area of materials science. After developing an interest in the area of materials, he joined the ECAE research group supervised by Dr. Ted Hartwig. He has been a teaching assistant for two semesters and a research assistant for eleven semesters working on the processing of Bi_2Te_3 compounds, bulk amorphous metals, niobium, tantalum, and $\text{Bi}_{90}\text{Sb}_{10}$ alloy using ECAE. His current interest is in the processing and developing of new materials, with plans to join industry,

His permanent address is:

Jae-taek Im

1902-1103 Dong, Castle Gold Park

Susung-gu, Daegu

Republic of Korea